POLITECNICO
MILANO 1863

SCUOLA DI INGEGNERIA INDUSTRIALE
E DELL'INFORMAZIONE

Multislit collimator characterization and dosimetry measurements for microbeam radiation therapy applications at the ESRF - ID17 Biomedical beamline

Tesi di Laurea Magistrale in
Physics Engineering - Ingegneria Fisica

Author: **Lucia Malucelli**

Student ID: 953366
Advisor: Prof. Marco Moretti
Co-advisors: Dr. Paolo Pellicioli
Academic Year: 2022-2023

Abstract

Microbeam radiation therapy (MRT) is an innovative radiotherapy technique that in the last decades has emerged as promising alternative to conventional radiotherapy approaches. It is based on the production of spatially fractionated, highly collimated and high intensity microbeams. Nowadays, optimal radiation sources for the production of microbeams are synchrotron sources as the ID17 biomedical beamline of the European Synchrotron Radiation Facility (ESRF). For the generation of 50 μm wide microbeams spaced by a 400 μm pitch, the most common geometry used in MRT, a multislit collimator (MSC) is necessary. The mechanical properties of the MSC are key factors for the production of an array of parallel and identical microbeams. To control MRT irradiation and ensure treatment reproducibility, elaborated dosimetry protocols have been developed. Differences between measured and simulated dose values in MRT are often above the 3% limit used in conventional radiotherapy for irradiation plan validation and several MRT studies are focusing on possible improvements.

Nowadays, two MSCs are available at the ID17 beamline: the CF-H25S+ MSC, present at the beamline since 2009, and a new one, the Densimet MSC, made of a more recent tungsten-based alloy, that is supposed to be more effective than the CF MSC in reducing the transmitted radiation through the MSC blades and thus the delivered dose between adjacent microbeams to the target (valley dose). The aim of this study is to characterize the Densimet MSC and compare it with the CF MSC to assess the improvements during MRT irradiation at the beamline.

After the study of the geometry of both MSCs, done measuring the FWHM and the center-to-center distance of the produced array of microbeams, the spectra transmitted by the MSC blades are theoretically calculated using NIST's data and simulated using Monte Carlo (MC) algorithms. A dosimetry study is conducted to measure the transmitted radiation through the MSC blade by means of a PTW microdiamond detector and radiochromic film dosimetry is performed to measure the valley dose between microbeams delivered to a water-equivalent phantom. MC simulations are compared to measured depth dose profile.

The theoretical and simulated results of the transmitted spectra are in good agreement, as well as the transmitted radiation through a single MSC blade measured with the PTW microdiamond detector. The reduced intensity of the transmitted spectrum is of 65-70% when using the Densimet MSC instead of the CF MSC.

30% reduction of valley dose is observed for film irradiated in air when using the Densimet MSC. Inside the phantom, 10% valley dose reduction for a $20 \times 20\ mm^2$ field and 15% valley dose reduction for a $5 \times 5\ mm^2$ field is measured when using the Densimet MSC. For valley dose measurements small variations are observed with respect to MC simulated values, probably due to the MSC model that is not considering blades misalignment and therefore it is neglecting the additional scattering component due to photons interacting with the inner walls of the MSC.

The results show a significant improvement when using the Densimet MSC. The new MSC is more effective in absorbing the radiation impinging on the collimator blades and consequently in reducing the valley dose delivered to the target. The reduction of the valley dose is a fundamental factor to be considered in MRT and the Densimet MSC is able to better control this parameter during irradiation.

Keywords: microbeam radiotherapy, microbeams, dosimetry, filmdosimetry, synchrotron radiation, multislit collimator

Abstract in lingua italiana

La radioterapia con microfasci (MRT) è un'innovativa tecnica di radioterapia che negli ultimi decenni è emersa come promettente alternativa alla radioterapia convenzionale. Si basa sulla produzione di fasci spazialmente frazionati, altamente collimati e ad alta intensità. Attualmente, sorgenti di radiazioni ottimali per la produzione di microfasci sono sorgenti di sincrotrone come la beamline biomedica ID17 dell'European Synchrotron Radiation Facility (ESRF). Per produrre microfasci larghi 50 μm e distanziati da un passo di 400 μm, geometria più utilizzata in MRT, l'utilizzo di un collimatore multifenditura (MSC) è necessario. Le proprietà meccaniche del collimatore sono fattori fondamentali per produrre una serie di microfasci paralleli ed identici. Per controllare l'irradiazione MRT e garantire la riproducibilità del trattamento, sono stati sviluppati eleborati protocolli di dosimetria. Le differenze tra i valori di dose misurati e simulati per MRT sono in genere ben al di sopra del limite del 3% utilizzato nella radioterapia convenzionale per la convalida del piano di irradiazione e diversi studi condotti sulla MRT si stanno concentrando su possibili miglioramenti.

Attualmente sono disponibili due MSC sulla beamline ID17: il CF-H25S+ MSC, presente sulla beamline dal 2009, e uno nuovo, il Densimet MSC, realizzato con una più recente lega a base di tungsteno, che dovrebbe essere più efficace del CF MSC nel ridurre la radiazione trasmessa attraverso le lame del MSC e quindi la dose tra microfasci adiacenti che arriva al campione (dose di valle). Lo scopo di questo studio è caratterizzare il Densimet MSC e confrontarlo con il CF MSC per valutare i miglioramenti durante l'irradiazione MRT presso la beamline.

Dopo lo studio della geometria di entrambi i MSC, realizzato tramite la misura della FWHM e della distanza da centro a centro della serie di microfasci prodotta dal collimatore, sono stati calcolati teoricamente gli spettri trasmessi dalle lame del MSC utilizzando i dati del NIST e poi simulati utilizzando algoritmi Monte Carlo (MC). È stato condotto uno studio dosimetrico per misurare la radiazione trasmessa attraverso le lame del MSC per mezzo di un rivelatore a microdiamante PTW ed è stata eseguita la film dosimetria per misurare la dose di valle tra i microfasci che arriva ad un cubo simulante acqua. Le simulazioni MC sono state confrontate con il profilo della dose all'aumentare della

profondità.

I risultati teorici degli spettri trasmessi sono in buon accordo con quelli simulati, così come la radiazione trasmessa attraverso una singola lama del MSC misurata con il rivelatore a microdiamante PTW. L'intensità ridotta dello spettro trasmesso è di 65-70% quando si utilizza il Densimet MSC al posto del CF MSC.

Si può osservare una riduzione del 30% della dose di valle per film irradiati in aria quando si utilizza il Densimet MSC. All'interno del cubo è stata misurata una riduzione della dose di valle del 10% per un campo di dimensioni 20×20 mm^2 e del 15% per un campo di dimensioni 5×5 mm^2 usando il Densime MSC. Nelle misure della dose di valle sono state osservate piccole variazioni rispetto ai valori simulati con MC, probabilmente a causa del modello utilizzato per simulare il MSC che non considera il disallineamento delle lame e dunque trascura l'ulteriore componente di scattering causata dai fotoni che interagiscono con le pareti interne del MSC.

I risultati mostrano un significativo miglioramento quando viene utilizzato il Densimet MSC. Il nuovo MSC è più efficace nell'assorbire la radiazione che incide sulle lame del collimatore e di conseguenza nel ridurre la dose di valle che arriva sul campione. La riduzione della dose di valle è un fattore fondamentale da considerare in MRT e il Densimet MSC è in grado di controllare meglio questo parametro durante l'irradiazione.

Parole chiave: radioterapia con microfasci, microfasci, dosimetria, filmdosimetria, radiazione di sincrotrone, collimatore multifessura

Contents

1 | Introduction

1.1. Radiation therapy for cancer treatment

Cancer is a generic word for a large group of diseases that can affects any part of the body and it is among the leading causes of death worldwide. It is a disease of the genes, the basic physical units of inheritance, of our body that control the way our cells work. Changes of these genes can cause malfunction, such as the growth or division of the cells when they shouldn't or the opposite. It arises from the transformation of normal cells into tumour cells, leading very often to death. One in five people worldwide develops cancer during his lifetime. In 2018, there were 18.1 million new cases and 9.5 million cancer-related deaths worldwide. By 2040, the number of new cancer cases per year is expected to rise to 29.5 million and the number of cancer-related deaths to 16.4 million [1].

Curing cancer has always been one of the most difficult challenges for medicine. There are many types of cancer treatments, depending on the type of cancer and how advanced it is. Most of the time patients receive a combination of treatments, such as surgery with radiation therapy and chemotherapy, or also immunotherapy, hyperthermia and many others [2, 4].

Radiation therapy (RT), also called Radiotherapy, is a cancer treatment that uses ionizing radiation, such us protons, ions or electrons, to possibly kill cancer cells and shrink tumours, by damaging the DNA of cancer cells. The energy deposited in matter by ionizing radiation is called absorbed dose and is measured in Gy which is defined as J/kg. Radiation also affects normal cells, causing side effects in healthy tissues areas crossed by the radiation to reach the tumour. However, RT treatments are effective because differential effects in the radiation response of healthy and cancerous tissue occur: the condition of the malignant tissue degrades more rapidly than the surrounding healthy tissue. This makes possible to define a therapeutic window where the highest possible dose of tumour control meets the lowest possible number of side effects. The concept of therapeutic window is shown as graphic in figure 1.1. To better improve this treatment, researches are

focusing in maximizing the therapeutic effect by expanding the therapeutic window.

The aim of RT is to maximise the tumour control probability (TCP) and minimize the normal tissue complications probability (NTCP). Quantities like TCP and NTCP give information on the expected quality of a treatment. Generally, both aims are not achievable simultaneously and thus the optimal compromise has to be found. One possible way to improve the treatment outcome is by means of a temporal fractionation of the dose: healthy tissue could better tolerate a radiotherapy cycle if delivered as a series of several smaller doses over consecutive days, maintaining a great control of the tumour. Indeed in this way, while healthy tissue has the opportunity of repairing the non-lethal DNA damages, the process of reoxygenation and cell-cycle redistribution increases tumour radio-sensitivity [14].

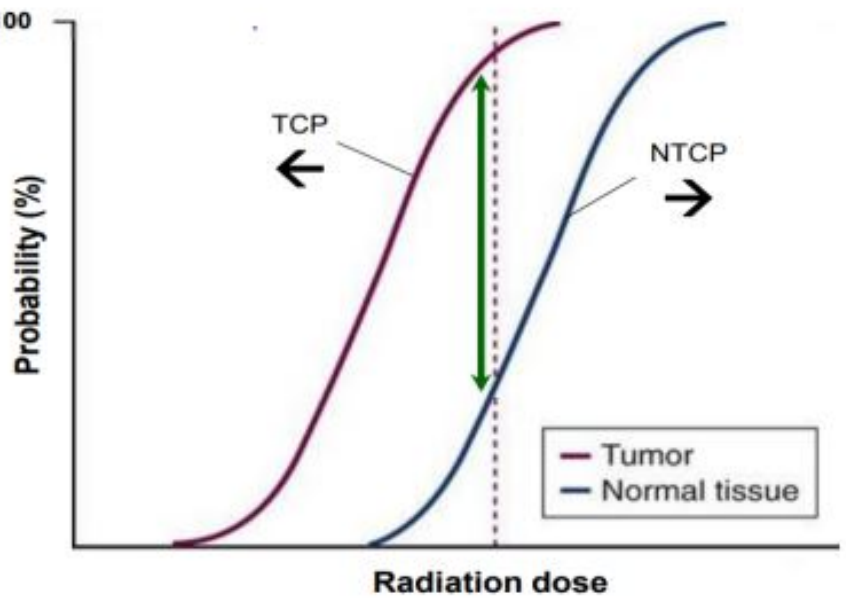

Figure 1.1: Schematic representation of the tumour control probability (TCP) in purple and of the normal tissue complications probability (NTCP) in blue as a function of the radiation dose. Both curves increase with the dose. Goal of innovative RT approaches is to maximize the therapeutic window in green by maximizing the TCP and the minimizing the NTCP for a delivered dose [14].

The therapeutic effect of radiotherapy is also maximized by increasing the geometric conformity of dose to the tumour target, trying to sculpt the high-dose region as close as possible to the target volume, limiting the dose delivered in the surrounding healthy tissues. Some of the major technical advancements in modern radiation oncology, such as

intensity modulation, motion management, particle therapy, have improved the conformity of dose to the target volume, reducing side effects in healthy tissues [9].

Spatial fractionation of the radiation field is a simple approach to reduce radiation-induced side effects. The first attempt of applying spatial fractionation to radiotherapy was done by Alban Kohler in 1909 [21], just few years after the discovery of X-rays. He showed that skin toxicity could be reduced using 'grid therapy', where a 3 mm^2 grid of woven iron wire was placed close to the skin of patients during kilovoltage irradiation. After that, in the past century, spatial fractionation was only partially studied and thus nowadays it is still a developing approach. There are several spatially fractionated RT approaches currently in pre-clinical development, including minibeam radiotherapy, that uses arrays of sub-millimetre parallel beams of X-rays or protons, and microchannel irradiation, that uses arrays of X-rays microbeams [9].

In this study we will focus on the Microbeam Radiation Therapy (MRT), that uses synchrotron X-ray radiation for the production of arrays of planar microbeams.

1.2. Microbeam Radiation Therapy - MRT

The first studies on microbeams were conducted in the 1960s by the team of W. Zeman, H.J. Curtis, and C.P. Baker [35], when they investigated the effects of cosmic radiation on humans. They found that the tolerance of mouse brain tissue to a deuteron beam of 22 MeV energy could be increased from 140 Gy/s to 4000 Gy/s when the diameter of the beam was reduced from 1 mm to 25 μm. Figure 1.2 shows the different effects caused in a mouse visual cortex by a 1 mm diameter beam on the left and a 25 μm diameter beam on the right.

This so-called *Dose Volume Effect* shows how healthy tissues better tolerate high radiation if confined in micrometric volume.

However, it was only in 1990s when D. Slatkin used microbeams for the first time for RT treatments, starting the first MRT program at the Brookhaven National Laboratory [32]. After few years J.Laissue demonstrated the high tolerance of healthy tissue to spatial fractionated beam irradiations [22, 23].

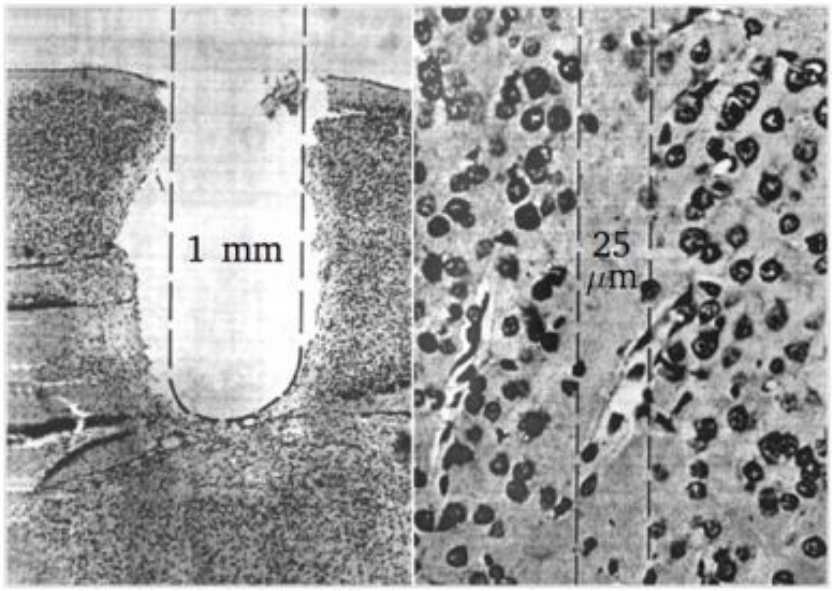

Figure 1.2: Histological images of a mouse visual cortex irradiated with a 22 MeV deuterium beam. On the left image, the mouse brain tissue irradiated with a 1 mm diameter beam and an entrance dose of 280 Gy, is completely destroyed, while on the right image the tissue irradiated with a 25 μm beam and an entrance dose of 4000 Gy is preserved [35].

Histological studies performed on a piglet brain 15 months after irradiation with a dose of 300 Gy showed how along the microbeams path the cells were destroyed, while in the surrounding region no haemorrhage was found and the tissue architecture was preserved, demonstrating the sparing of normal tissue to spatial dose-fractionation, as shown in figure 1.3.

The development of MRT programs was possible thanks to the realization of high-energy Synchrotron Radiation (SR) sources capable of producing X-ray radiation that fulfills the requirements needed for MRT studies.

Nowadays MRT is in pre-clinical development in a small number of synchrotrons that present a beamline able to generate microbeams: the European Synchrotron of Radiation Facility (ESRF) in Grenoble (France), the Australian Synchrotron (ANSTO) in Melbourne (Australia), the Canadian Light Source in Saskatoon (Canada) and the SPring-8 in Hyogo Prefecture (Japan).

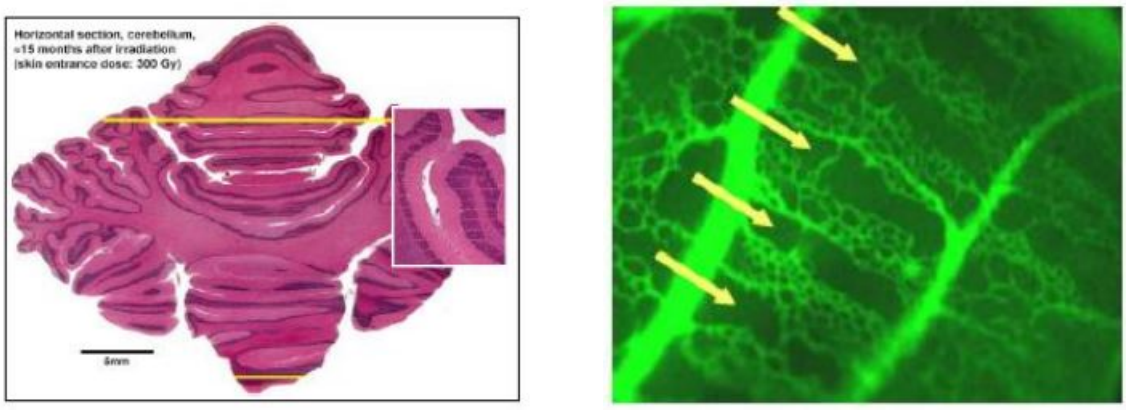

(a) (b)

Figure 1.3: (a) Horizontal section of a piglet cerebellum about 15 months after irradiation with a skin entrance dose of 300 Gy [23]. It is possible to see the paths of the microbeams as thin, weak and white horizontal parallel stripes. The piglet was behaving well after the irradiation. (b) Microscope picture of the microbeam damage reparation, observed in vivo in a chicken embryo chorioallantoic memabrane [10].

In MRT, spatial dose-fractionation is defined at micrometric scale. Fields are characterized by an array of planar microbeams 25-100 μm wide and with a center-to-center (c-t-c) distance of 100-400 μm [15]. Nowadays, the most common geometry of microbeams is of 50 μm wide beams, spaced by 400 μm pitch. The result is a spatial modulation of the delivered dose characterized by a peak dose (along the microbeam path) that can be up to some hundreds of Gy, and valley dose (between adjacent peaks) where dose is deposited following radiation scattering events in the irradiated volume. Figure 1.4 shows an example of MRT dose profile.

The peak to valley dose ratio (PVDR) is in the range of 20-50 for pre-clinical studies. To have an efficient spatial fractionation, indeed, it is fundamental to have a significant dose difference between peaks and valleys. The quantity that has to be defined and controlled with high precision is the valley dose, because in these regions the destruction of healthy tissue must be prevented by keeping the dose less than the tissue tolerance limit. Configurations with high PVDR values are therefore preferred in order to maximize the delivery of high peak doses able to kill tumour cells and minimize valley dose between microbeams to avoid healthy tissue ablation. Orthovoltage X-rays, with energies between 80 keV and 200 keV, are therefore used for microbeam irradiations because in biological tissues primary photons have the minimum lateral scattering and the secondary electrons thermalized close to their original position, minimizing dose delivery in the valley region.

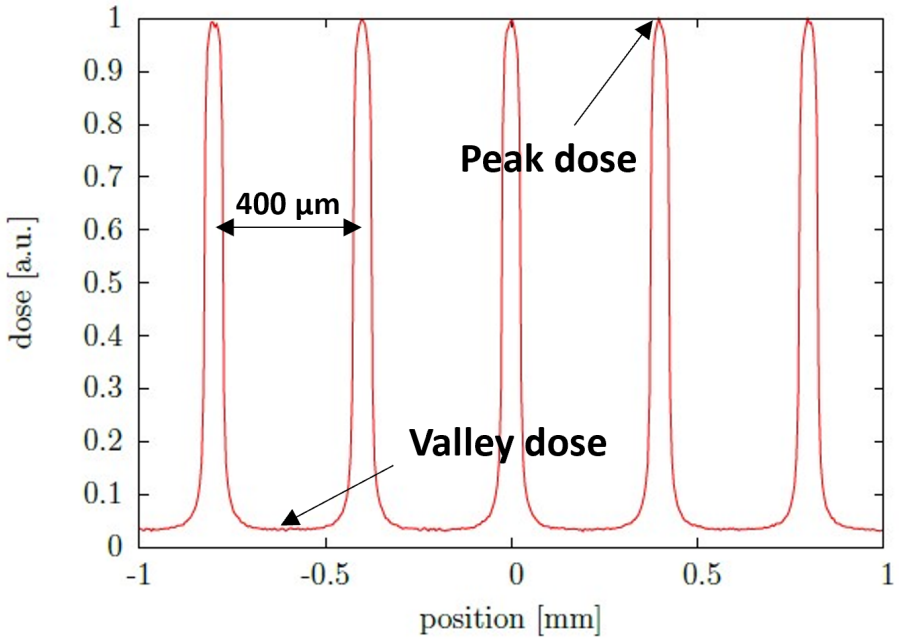

Figure 1.4: Example of a calculated microbeam dose profile used for MRT treatments, with indicated the peak doses, mainly defined by primary photons, and valley doses, resulting by scattering events of radiation inside the target volume. Here the peaks are characterized by a center-to-center distance of 400 μm. The dose difference between peak and valley can be up to 50 times [14].

Third generation SR sources are still the best option for the production of microbeams, because able to produce intense X-rays beams with small divergence. Indeed, to avoid any kind of blurring of microbeams induced by cardiovascular or pulmonary motions, a very fast dose delivery in a fraction of a second is required. The extremely highly brilliant X-rays beam produced by a synchrotron source results in ultra-high dose rates up to hundreds or thousands Gy/s, allowing dose delivery in very short time. Another emerging technique based on the use of quick irradiation of fraction of a second, called Flash RT, is performed without the use of spatial fractionation of the beam. Therefore, researchers are investigating if it is possible to apply Flash effect also in MRT treatments performed at the synchrotron [28].

Another mandatory characteristic of the beam while performing MRT treatments is a very low divergence to keep the microbeam shape inside all the crossed target. At the ESRF-ID17 beamline the synchrotron beam divergence in the horizontal and vertical direction is around 1 mrad and 0.02 mrad, respectively, significantly smaller with respect to the almost 35 mrad of the conventional X-rays sources.

1.2.1. Physic of radiation interaction with matter

X-rays were discovered in 1895 [7] and they are a penetrating form of high-energy electromagnetic radiation, with short wavelengths ranging from 10^{-12} to 10^{-8} m, corresponding to high frequencies in the range of 10^{18} up to 10^{22} Hz. When interacting with matter, X-rays are attenuated by four principal phenomena: Compton scattering, Rayleigh scattering, Photoelectric absorption and electron-electron pair production. Each of these phenomena have a different probability to occur depending on the X-ray energy. Figure 1.5 represents the attenuation coefficient for water as a function of the X-ray energy, clearly showing the different contributions of the total attenuation coefficient. In the energy range relevant for MRT (between 50 keV and 200 keV) the two most probable scattering events are:

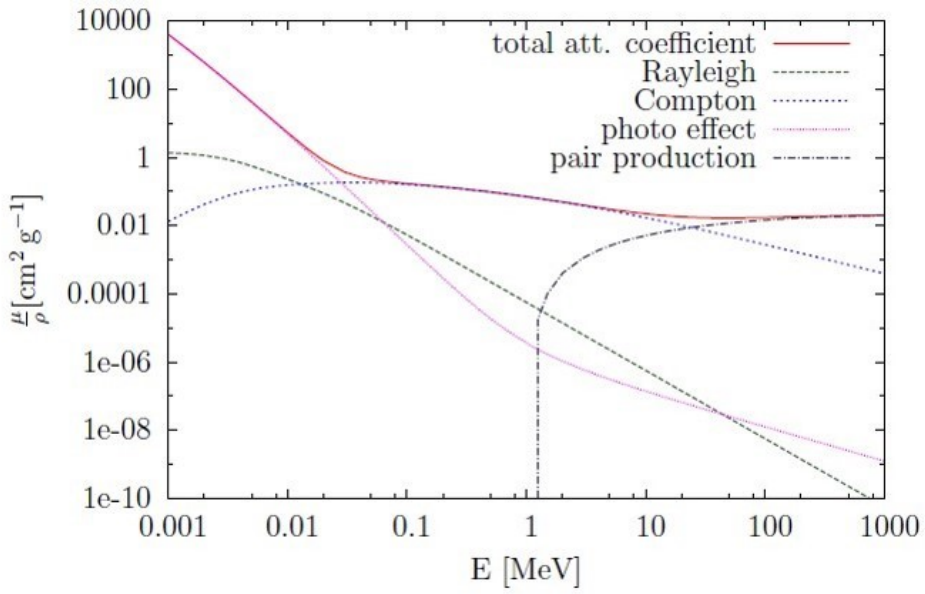

Figure 1.5: The X-ray mass attenuation coefficient of water as a function of the photon energy. The total coefficient is a sum of different scattering mechanisms, which occur with different probability depending on the photon energy. In the energy range of interest for MRT (between 50 keV and 200 keV) the Compton scattering and the Photoelectric effect are predominant [14].

- Compton scattering: it consists in the interaction between the incoming photon and a weakly bound electron (quasi-free electron). The photon transfer part of its energy to the electron causing the scattering of the latter outside the atom or molecule. The angle formed by the trajectory of the emitted electron and the diffuse photon is called Compton angle. Figure 1.6 a shows a schematic a representation of this

process.

- Photoelectric effect: it is the process in which an electron is emitted by the material upon absorption of a photon. The photon transfers completely its energy to the electron that in turns is emitted with a kinetic energy equal to: $E = hv - E_B$, where hv is the energy of the incoming photon and E_B is the binding energy of the electron. The result is an ionized atom that, in order to find the status with the minimum possible energy and thus more stable, it will rearrange by the phenomenon called atomic relaxation with an associated energy called relaxation energy. This energy in turns can lead to the emission of a fluorescence photon after an electron from a higher level has filled the lacuna left by the photoelectron. Figure 1.6 b shows a schematic a representation of this process.

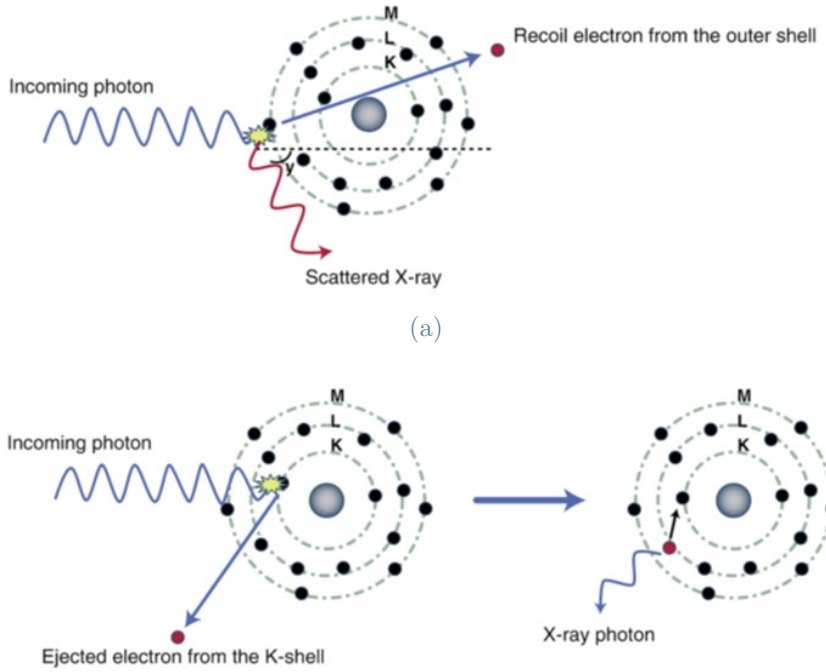

Figure 1.6: Schematic representation of the two main processes generating secondary electrons in MRT: (a) Compton scattering and (b) Photoelectric effect.

While the Rayleigh scattering could happen in the range of energies used for MRT, but the energy transfer from the photon to the bound electron would be approximately zero so can be neglected, the pair production cannot occur, because energies greater than 1 MeV are needed. The high energy electrons emitted by the Compton scattering and by the Photoelectric effect are called secondary electrons that, in turns, interact with the electrons of the material they traverse by a series of Coulomb interactions. These

secondary electrons are the responsible of the dose deposited inside the target during irradiation. In living tissues this could result in a beneficial, but also dangerous biological effect, like DNA modification or cell death [27].

1.2.2. Potential clinical applications of MRT in medicine

Nowadays MRT is in a pre-clinical phase and up to now no human patients have been treated. The greatest challenge is, indeed, to develop safe protocols that allow to apply the unique radiobiological properties of MRT to clinical human trials. Several potential clinical applications of MRT have been identified [15].

- MRT as a boost for conventional radiotherapy: the valley dose would match the conventional radiotherapy dose while the peaks would act as a boost to increase the tumour control. Bouchet et al (2016) [12] demonstrated a better efficiency of microbeam radiation therapy on glioma with respect to broad beam when MRT valley dose matches the broad-beam dose.
- MRT as a primer for drug delivery: in this case the differential effect of MRT in tumour and healthy tissue would be used. MRT, indeed, does not modify vascular permeability of normal tissue, while it increases permeability in tumour tissue [11]. Moreover, synergistic effect of MRT together with a range of drugs and immunotherapy could be exploited.
- MRT as a micro-surgical tool in neurological disorders: MRT has potential for alleviating the symptoms of neurological conditions, for example suppressing the networks responsible for abnormal movement. This is the case of spinal cord injury or epilepsy [16].

1.3. The European synchrotron (ESRF)

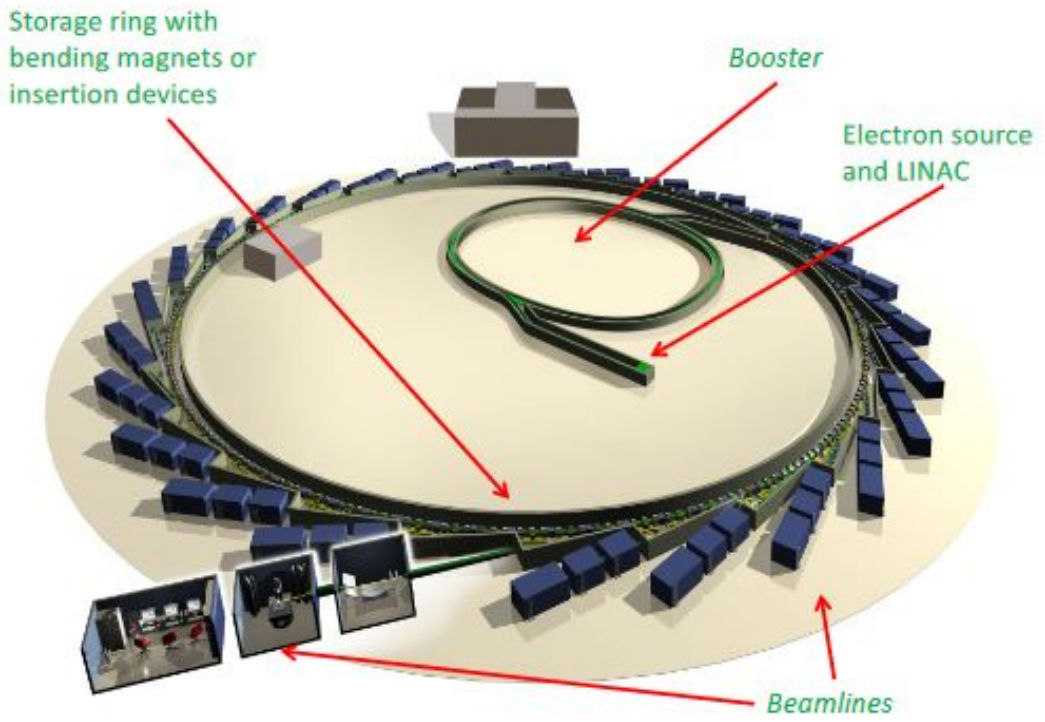

Figure 1.7: Schematic of the European Synchrotron of Radiation facility (ESRF) [6].

Founded in 1988 by twelve European countries, the ESRF is today the most powerful synchrotron radiation source of fourth generation in Europe for the production of high-flux photon beams by accelerating electrons to relativistic energies. In figure 1.7 a schematic representation of the ring and the beamlines of the ESRF is shown.

Before emitting radiation, electrons undergo several processes of acceleration to reach their final energy. The electron beam is generated by an electron gun and then firstly accelerated up to energies of 200 MeV by a linear accelerator (LINAC). Then electron bunches are injected in a first accelerator of 300 meters of circumference, called *booster*, where they reach the maximum energy of 6 GeV. The electrons are then injected in a storage ring of 844 meters of circumference for X-ray radiation production. The ESRF storage ring can store a maximum current of 200 mA and is kept under ultrahigh vacuum (UHV) conditions to limit the interaction between electrons and the residual gas atoms.

The storage ring is made of sequences of straight sections and curved sections. The curved sections are called *bending magnet* (BM), permanent magnet designed with the

aim of deviating the overall trajectory of the electrons making them turning in a closed loop. Straight sections, instead, hosts *insertion devices* (ID), which consist of a sequence of dipole magnets of opposite polarities where the magnetic field (that can be varied by changing the gap between the poles) forces the electrons to oscillate around a straight trajectory, obtaining a highly collimated cone of emitted radiation. There are two different types of IDs: *wigglers* and *undulators*. In an undulator the magnetic field is smaller compared to wigglers and so does the oscillations of the electrons, resulting in a further collimation of the beam [27, 28]. Figure 1.8 shows a schematic representation of the main sections of the storage ring.

The emitted radiation is finally collected by so-called beamlines that are installed along the storage ring, following the tangential direction of the beam. Here different experimental set up are used for researching in many areas: engineering, physics, chemistry, earth science, biology and medicine.

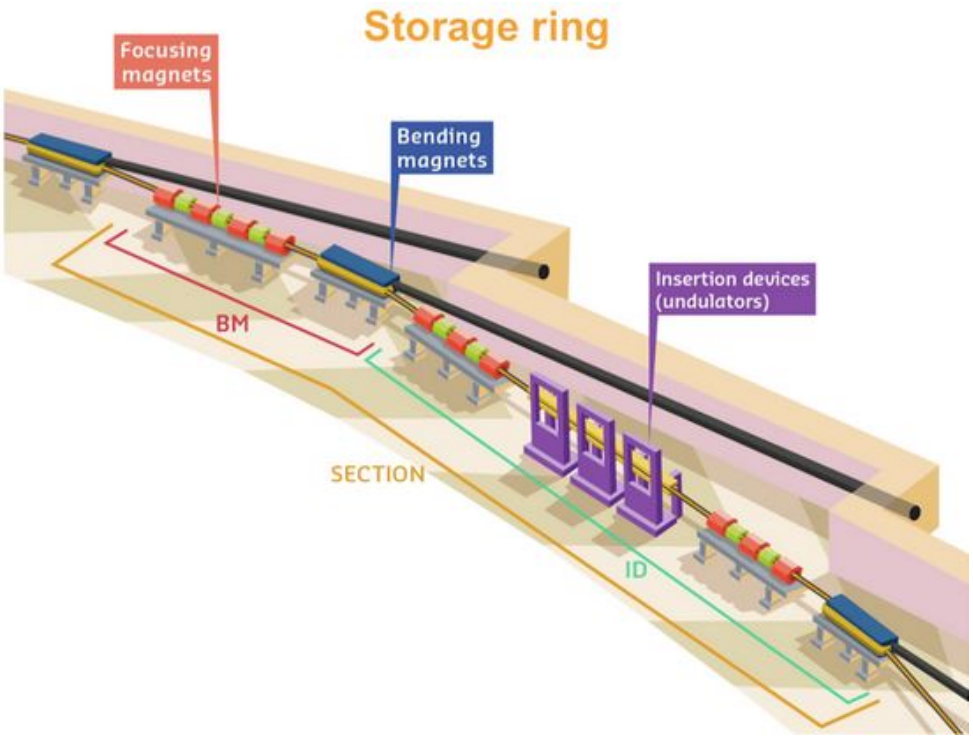

Figure 1.8: Schematic representation of the main sections of the storage ring: the bending magnet (BM) used for closing the overall trajectory of the electrons, the insertion device (ID) for the generation of synchrotron radiation, and focusing magnets [5].

Furthermore, as a result of the radiation emission, the charges lose part of their kinetic energy. Thus, to restore the energy loss and to maintain a constant average energy along the ring, the electrons are further accelerated by straight devices called Radio-Frequency

(RF) cavities. The electron passing through a RF cavity is kicked by the electric field to compensate the energy lost due to the radiation emission. However, this operation must be synchronized just with the electrons that have a lower energy. This synchronization implies that electrons cannot circulate along the ring as a continuous flow, but must form discrete bunches. This in turn implies that the synchrotron radiation is not continuous, but pulsed. Moreover, the number of circulating electrons decreases exponentially, because of the scattering with the residual gas atoms or due to a not perfect compensation of all the energy losses by the RF cavity. For that reason, when the current in the ring falls below a minimum acceptable level, new electrons are injected by the *refilling* procedure.

1.4. The synchrotron radiation

When moving electrons cross a magnetic field, their trajectory is modifying following the Lorentz law:

$$\vec{F} = q_p \cdot \vec{v} \times \vec{B}, \tag{1.1}$$

where q_p is the charge of the particle, $\vec{v}$ is its velocity and $\vec{B}$ is the magnetic field.

An accelerated charge emits electromagnetic radiation, called synchrotron radiation. Due to the relativistic nature of the electrons in the storage ring, the radiation field generated by their acceleration is not distributed in an isotropic way around the particle, but it forms a cone emitted tangentially to the electron direction, as shown in figure 1.9.

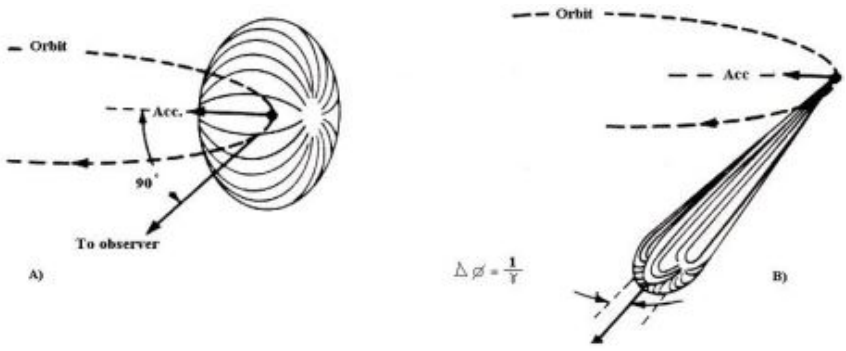

Figure 1.9: Distribution of the radiation field generated by an accelerated charged particle with relativistic nature (A) and non-relativistic nature (B) [18].

Synchrotron radiation has several unique properties [26]:

- **High intensity** (brightness): the SR radiation has an intensity $I \propto \frac{\gamma^4}{R^2}$, where R

is the radius of the storage ring and $\gamma = \frac{1}{\sqrt{1-(\frac{v}{c})^2}}$ (v is the velocity of the electron and c is the speed of light), that in relativistic conditions can be extremely high.

- **High collimation**: also the radiation emission angle is influenced by the relativistic motion of the electrons resulting in a total divergence almost equal to $\theta = \frac{1}{\gamma}$. θ can be really small, which means that the synchrotron radiation has an extremely narrow angular spread.
- **Pulsed temporal structure**: as seen before, the electrons don't circulate along the ring as a continuous flow, but they form discrete bunches, obtaining a pulsed beam.
- **Wide spectral distribution** (tunability): depending on how electrons are accelerated, by means of bending magnets or insertion devices, different spectral distribution can be observed.

To better explain the last point let's consider the case of a *bending magnet*. Due to the very narrow angular width of the photon beam emitted, it is very similar to a searchlight. This means that the detector (i.e. the experimental station along the beamline) is illuminated for a very short time. It is possible to calculate the time duration of the photon pulse seen by a point detector located at a distance D_L from the source, as shown in figure 1.10.

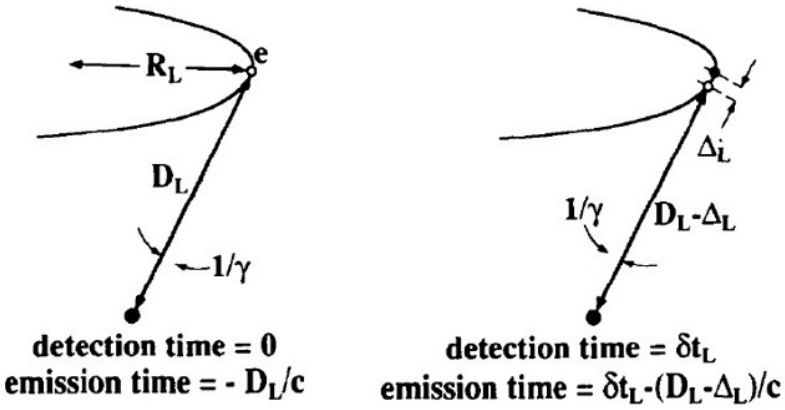

Figure 1.10: Estimate of the duration time of a pulse of synchrotron radiation, i.e. the time interval δt_L during which the detector is illuminated [26].

Considering a first photon emitted at $t_L = 0$ and detected at $t_L = \frac{D_L}{c}$ and also being Δ_L the distance covered by an electron during the time interval with a velocity v, the last photon will be emitted at $t_L = \frac{\Delta_L}{v}$ and detected at $t_L = \frac{\Delta_L}{v} + \frac{D_L - \Delta_L}{c}$. Thus, the time interval during which the detector is illuminated is the difference between the last and the first detection event:

$$\delta t_L = \frac{\Delta_L}{v} + \frac{D_L - \Delta_L}{c} - \frac{D_L}{c} = \frac{\Delta_L}{v} - \frac{\Delta_L}{c}, \tag{1.2}$$

Furthermore, defining $\beta = \frac{v}{c} \simeq 1$ and considering the emission angle $\Delta\theta = \frac{\Delta_L}{R}$, where R is the curvature radius, and knowing that $\Delta\theta \sim \frac{1}{\gamma}$ and thus $\Delta_L = \frac{R}{\gamma}$, it turns out that:

$$\delta t_L = \Delta_L(\frac{1}{v} - \frac{1}{c}) \simeq \frac{R}{\gamma}(\frac{1}{\beta c} - \frac{1}{c}) = \frac{R}{\gamma}\frac{1-\beta^2}{\beta c(1+\beta)} = \frac{R}{c\gamma^3}\frac{1}{\beta(1+\beta)} \simeq \frac{R}{2c\gamma^3}, \tag{1.3}$$

Being γ big, this means that the photon pulse can be extremely short. Using the energy time uncertainty principle ($\delta E \delta t \geq \hbar$):

$$\Delta E \approx \Delta\omega \simeq \frac{2c}{R}\gamma^3, \tag{1.4}$$

This corresponds to a broad emission spectrum.

Wigglers have similar emission spectra, but with much higher intensities.

In *Undulators*, by contrast, electrons do many small oscillations. That corresponds to a coherent superposition of many searchlights, thus the detector is now continuously illuminated. The emission spectrum is no longer continuous, but it is characterized by many peaks.

Figure 1.11 shows an example of spectra for the three different type of SR sources:

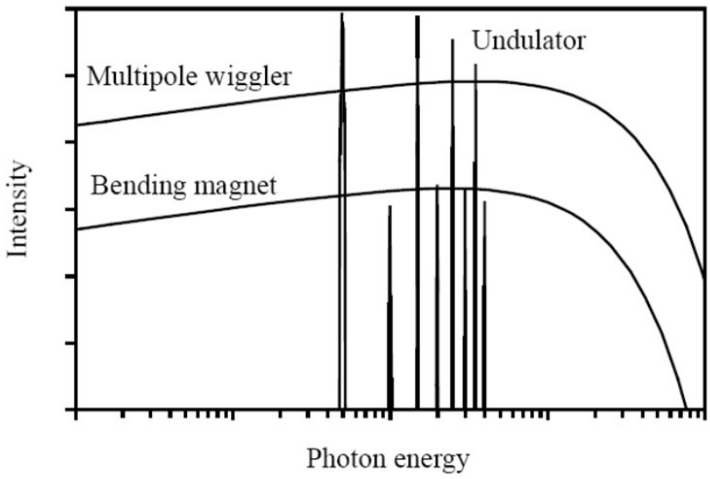

Figure 1.11: Spectral distribution of the radiation generated by a wiggler, a bending magnet and an undulator as a function of the photon energy [8].

Therefore, the wiggler turns to be the more suited insertion device to produce X-ray radiation for MRT due to the extremely intense photon beam generated.

1.4.1. Wiggler field

The field produced by a wiggler along the beam axis is periodic and can be described by the following scalar potential [20]:

$$\phi(s,z) = f(z)cos(2\pi\frac{s}{\lambda_u}) = f(z)cos(k_u s), \tag{1.5}$$

It is possible to consider a scalar and not a vector potential because there are no electric currents along the beam. As shown in figure 1.12 a, s is the horizontal direction along the beam axis, while z is the vertical direction. Moreover λ_u is the periodic length of the field.

Applying the Laplace equation to (1.5)

$$\Delta^2\phi(s,z) = 0, \tag{1.6}$$

one obtains:

$$\frac{d^2f(z)}{dz^2} - f(z)k_u^2 = 0. \tag{1.7}$$

Thus the solutions is:

$$f(z) = Asinh(k_u z). \tag{1.8}$$

Substituting (1.8) into (1.5) one obtains:

$$\phi(s,z) = Asinh(k_u z)cos(k_u s), \tag{1.9}$$

Considering just the vertical component, that is the only one relevant for the particle motion, the magnetic field produced by a wiggler is (see figure 1.12 a):

$$B_z(s,z) = \frac{\partial\phi(s,z)}{\partial z} = k_u Acosh(k_u z)cos(k_u s). \tag{1.10}$$

The value of the constant A can be estimated considering the strength of the poletip field B_0 at $z = \frac{g}{2}$ (see figure 1.12 b), where g is the gap height of the wiggler:

$$B_0 = B_z(0, \frac{g}{2}) = k_u A cosh(k_u \frac{g}{2}) = k_u A cosh(\pi \frac{g}{\lambda_u}), \tag{1.11}$$

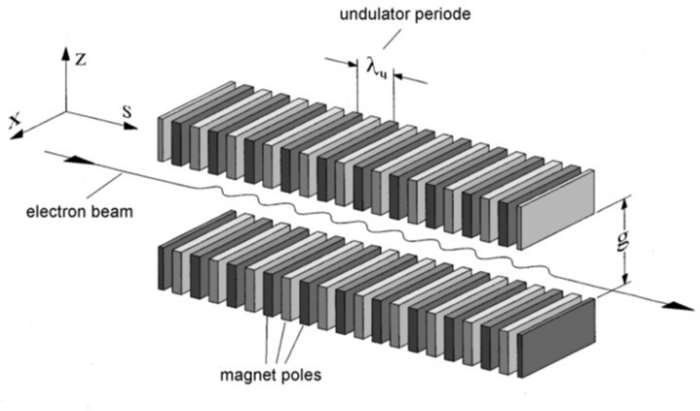

(a) Oscillations induced to the electron beam by the wiggler field.

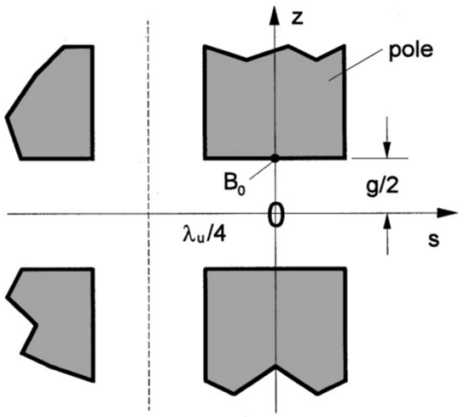

(b) Poletip field B_0 calculated at $z = \frac{g}{2}$, where g is the gap height of the wiggler, and $s = 0$.

Figure 1.12: Wiggler insertion device [20].

from which one obtains:

$$A = \frac{B_0}{k_u cosh(\pi \frac{g}{\lambda_u})}. \tag{1.12}$$

Therefore, the field around the electron beam become:

$$\tilde{B} = \frac{B_0}{cosh(\pi \frac{g}{\lambda_u})}. \tag{1.13}$$

The total field is inversely proportional to the gap: it decreases very rapidly with increasing gap height, as shown in figure 1.13.

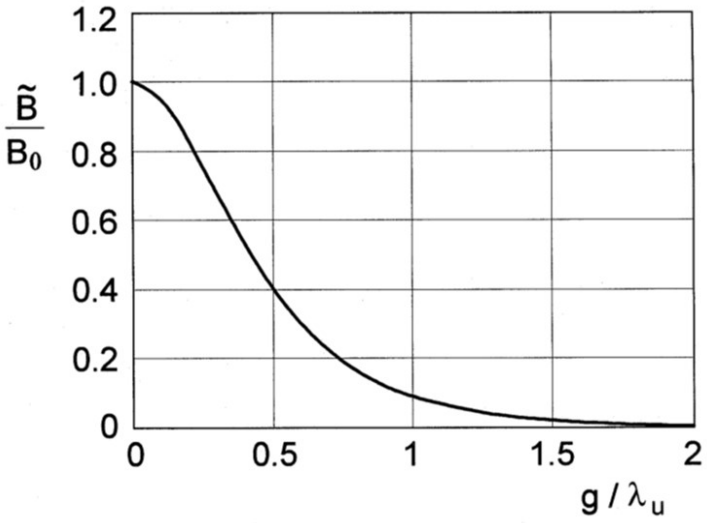

Figure 1.13: Wiggler field normalized with respect to the poletip field as a function of the gap height normalized with respect to periodic length of the field: $\tilde{B}$ decreases with increasing of g [20].

1.5. The ID17 biomedical beamline of ESRF

The ID17 is the biomedical beamline of the ESRF [12,13,14]. It was designed with the aim of supporting innovative works in radiation therapy and medical imaging. As for most of the beamlines, after the radiation source, it is possible to identify three main zones in which the beam is sent in:

- the *optical hutch*: close to the ring, here are located several components used to define the beam quality and shape to be sent to the target.
- the *experimental hutch*: all the detectors used for measuring and recording information about the radiation-matter interaction are located in this part.
- the *control cabin*: where researchers can monitor the experiment and analyze the obtained data.

The ID17 is one of the so-called long beamlines of the ESRF. Indeed, there are two different experimental hutches: the first one is located at 40 m from the source and it is

mainly dedicated to MRT experiments. Here a polychromatic beam is available with a dose rates up to 16 kGy/s. The second hutch is located at 150 m from the source in a satellite building and is dedicated to medical imaging experiments.

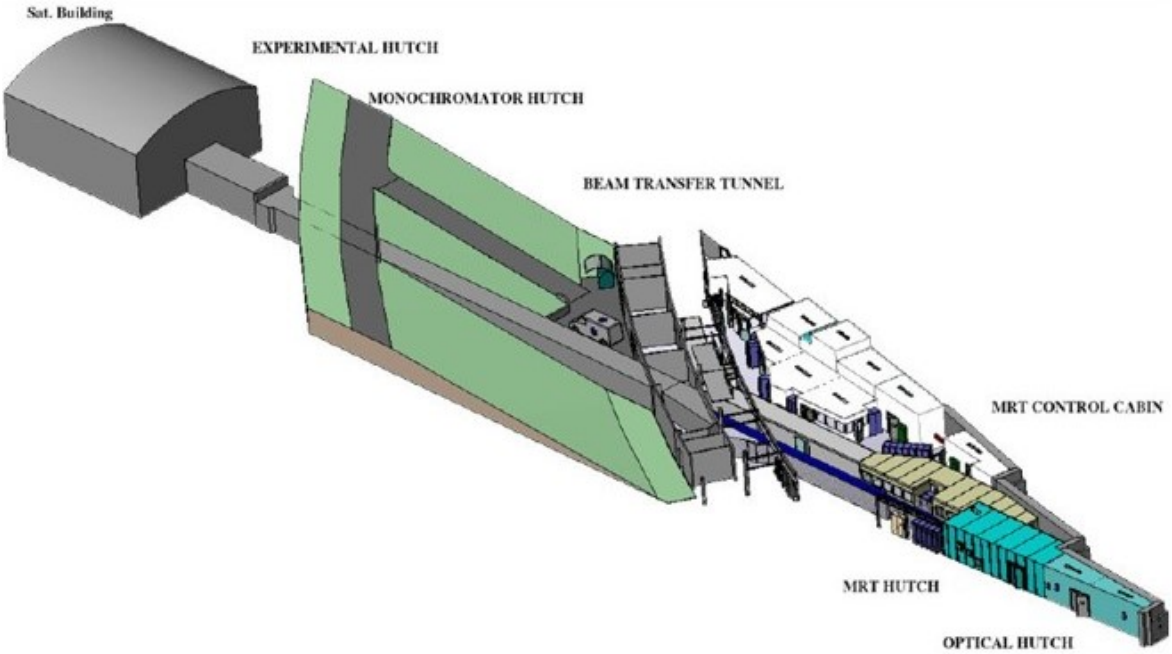

Figure 1.14: Scheme of the ID17 biomedical beamline. The experimental hutch 1 hosts the setup for MRT and is located around 40 m from the storage ring. A long tunnel is used to transfer the beam to the satellite building where a second experimental hutch is used for imaging experiments [18].

By mean of dedicated crystals, the polychromatic beam is transformed to monochromatic before entering in the second hutch, with energies that can be tuned between 20 and 130 keV and dose rates of up to hundreds of Gy/s. Figure 1.14 shows a schematic picture of the ID17 biomedical beamline.

In the following sections a detailed description of the optical and experimental hutch dedicated to MRT is presented.

1.5.1. ID17 optical hutch for MRT

The radiation generated by the wiggler source is transported through the *optical hutch* along a stainless steel pipe under vacuum conditions. The pipe is isolated by means of different valves and Beryllium (Be) windows [18, 27, 28]. At 21.6 m from the sources a diaphragm defines the beam dimension of 2.4 cm and 0.5 cm respectively in the horizontal

and vertical direction, in order to minimize the heat load on the instrumentation from useless radiation. Two couple of motorized slits, made by oxygen free copper blocks, define the overall size of the rectangular field entering the experimental hutch. A combination of different water-cooled filters, made of carbon, aluminum and copper of different thickness, are used to attenuate the beam and to cut photon energies below 50 keV, non-effective for microbeam treatments. Different combinations of attenuators allow the definition of different spectra profiles and intensities.

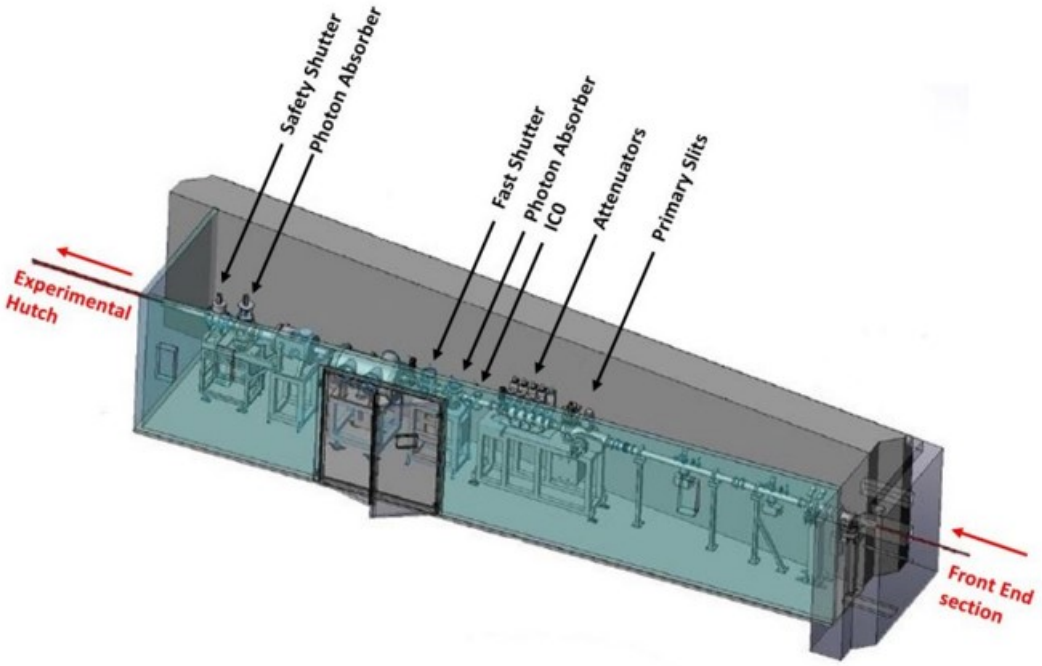

Figure 1.15: ID17 optical hutch with highlighted the main components used during MRT experiments to define the beam quality and shape [18].

Two ionization chambers (ICs) are installed in the optical hutch to monitor the beam intensity after the attenuators train. In order to accurately control the exposure time of the radiation on the sample, a fast shutter realized with two 15 mm thick blades of tungsten carbide (WC), is placed after the IC. This shutter is able to provide a minimum opening time of 5 $\pm$0.5 ms [27]. At the end of the optical hutch a safety shutter separates the optical hutch from the experimental hutch. Figure 1.15 shows a schematic view of the ID17 optical hutch with the main components.

1.5.2. ID17 experimental hutch for MRT

At the beginning of the experimental hutch, the X-ray radiation exits the pipe under vacuum condition and starts to propagate in air. A first ionization chamber (IC1) monitors the beam intensity at the entrance of the experimental hutch. Following, some PMMA blocks can be used to further attenuate the beam intensity. A rotary shutter is present also in this hutch and can be used independently or in combination with the fast shutter installed in the optical hutch. Figure 1.16 shows a schematic view of the ID17 experimental hutch with the main components.

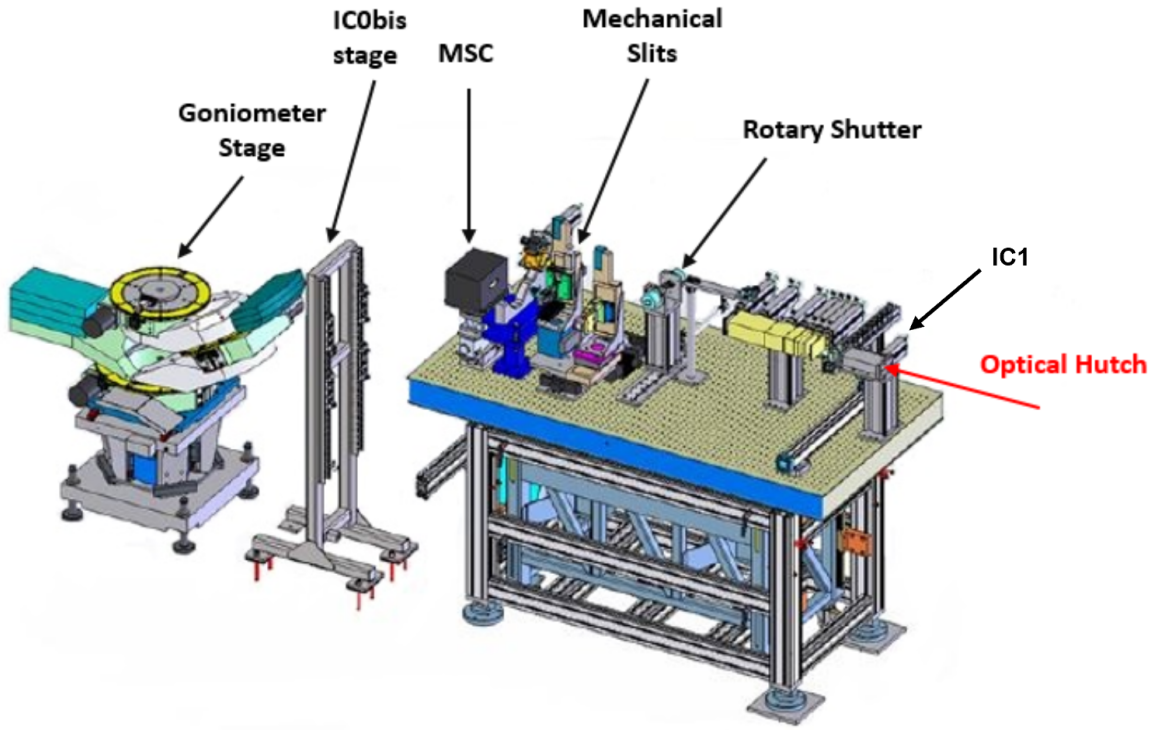

Figure 1.16: Technical drawing of the instrumentation present in the MRT experimental hutch, from the IC1 to the high precision goniometer [18].

The final beam height is defined by one of four vertical apertures with fixed dimension (51 μm, 102 μm, 520 μm and 795 μm) centered with the center of the beam. A couple of motorized horizontal slits can be moved inside the beam to precisely define a beam width below 1 mm. The maximum dimension of the beam reaching the target is the 2 mm x 35 mm, too small to directly irradiate a target with a vertical extension higher than 2 mm. In order to overcome this limitation a scanning technique is used: the sample is placed

on a kappa-type goniometer and it is vertically translated at constant speed through the photon beam. The vertical movement range of the goniometer is of approximately 14 cm.

For microbeams creation, a multislit collimator (MSC) is placed inside the beam, before the target, to spatially modulate the intensity of the homogeneous synchrotron beam. The MSC is a machined block of metal with equidistant aperture that defines the width and periodicity of the microbeams. At first, it was realized with a fixed geometry alternating Au and Al foils, but soon Tecomet was built, a MSC characterized by apertures of variable width [33]. Nowadays, even if variable apertures are more versatile, MSCs of fixed geometry are used, because easier to align and to control during experiment. Typically made of a tungsten-based alloy, MSCs are created with a single block or assembling individual blades for obtaining the desired width and spacing of microbeam array [15].

Figure 1.17 shows the technical drawing of one of the MSCs available at ID17.

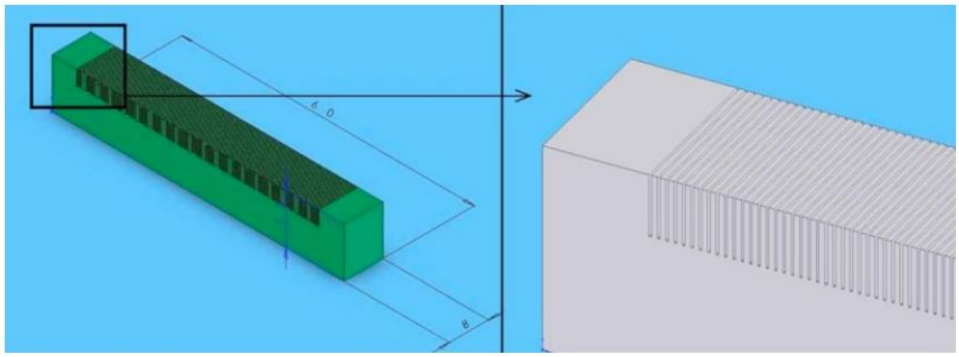

Figure 1.17: Schematic drawing of a single block MSC available at the ID17 beamline [15].

Using a MSC, two main configurations are possible for the creation of microbeams at the beamline:

- *Vertical microbeams*: the MSC fractionates the broad beam into small rectangular beamlets along the horizontal direction. Keeping fixed the MSC position while scanning vertically the target the painting of vertical microbeam is possible. Figure 1.18 (a) shows a schematic draw of this scanning technique.
- *Horizontal microbeams*: the MSC defines an aperture periodicity along the vertical direction. If the MSC is translated together with the target, the MSC's apertures are exposed consecutively and horizontal microbeams are defined on the target. Figure 1.18 (b) shows a schematic draw of this scanning technique.

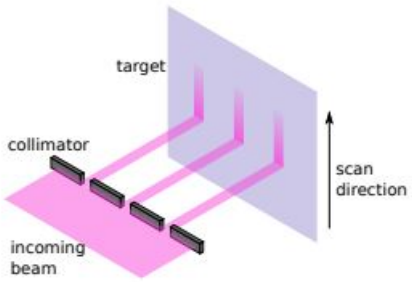

(a) Vertical microbeams.

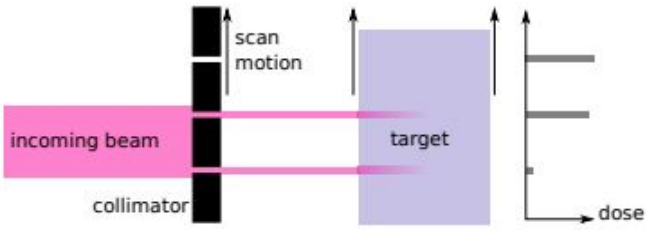

(b) Horizontal microbeams.

Figure 1.18: Schematic of two different configurations for the production of microbeams using a MSC and a scanning technique [14].

At the end of the experimental hutch, around 4 m from the goniometer stage, a second ionization chamber (IC2) is used for beamline alignment procedure and beam monitoring. The last device installed along the beam is a Fast-Readout Low-Noise (FReLoN) CCD camera that is used for imaging purposes as radiography of the target with a resolution of around 23 μm.

1.5.3. Novel and future radiation sources

One obstacle to the translation of MRT to clinical human trials is the lack of compact microbeam sources able to make this technique available in more research centers and hospitals. Nowadays only a third or fourth-generation synchrotron can produce microbeams fulfilling all the criteria required for an efficient MRT treatment. However, synchrotrons are large facilities that need a large space to be build and they are very expensive to run. Synchrotrons remain great options for research and developing in MRT, but alternative compact microbeam sources must be developed for clinical applications at large scale. Some examples of new technology for compact radiation sources potentially able to allow MRT are listed below [9]:

- *Inverse Compton scattering sources*: this source works similarly to synchrotrons

with the difference that electrons, instead of being deflected by static magnetic field of undulators or wigglers, interact with the electric field of a strong laser. Currently, there are two possible designs of this kind of source: a linear accelerator or a storage ring based system.

- *Compact X-ray tube based microbeam sources*: In X-rays tube electrons are accelerated up to several hundred keV of kinetic energies and sent toward a target made of materials with high atomic numbers (usually tungsten). When interact with the target atoms, electrons generate bremsstrahlung and characteristics X-ray photons that are emitted isotropically. One of the main problem is that most of the incoming electrons' kinetic energy is converted in to heat. Thus, the focal spot of electron must be limited to keep the surface target temperature below the melting point. Therefore, the optimal compromise between focal spot size and flux of the beam must be found. Moreover, the divergence is too high, resulting not in microbeams, but minibeams. Appropriate collimators need to be fabricated.

- *Proton microbeams*: at first protons were excluded for MRT, because they show strong lateral scattering. Nevertheless, particular proton beams have recently been investigated for MRT, because they are easy to produce and shape. Similar to conventional proton therapy, the tumour is treated with homogeneous dose, but then, in order to obtain normal tissue sparing, spatial dose fractionation is applied only in the entrance region.

1.6. Dosimetry for MRT

In RT experimental dosimetry is essential for the possible prediction and validation of the dose delivered during a treatment. MRT dosimetry is still nowadays highly challenging, because dosimetry must be done at micrometric scale to properly characterized the dose profile of microbeams. Very high dose rates are used that can easily bring to detector saturation and the use of X-ray in the keV range requires particular attention in the choice of materials used for detectors construction.

The important physic quantity to be measured in RT is the mean absorbed dose (D), that is the quantity of energy deposited by ionizing particles per unit mass:

$$D = \frac{dE}{dm} \tag{1.14}$$

Photons are indirect radiation sources, because, being uncharged particles, the dose is

actually deposited by secondary electrons generated by the interaction of the photon beam with the matter. In the SI the dose is measured in Gy that corresponds to $\frac{J}{Kg}$.

1.6.1. Experimental dosimetry for MRT

Before microbeam irradiation, absolute dosimetry is performed in a homogeneous field following as close as possible the International Atomic Energy Agency (IAEA) for reference dosimetry, using medium energy kilovoltage X-rays and ionization chamber as detector. At ID17 beamline the protocol established by Fournier et al. [18] is followed, based on the use of a PTW PinPoint ionization chamber with small sensitive volume of 0.015 cm^3.

For dosimetry at microscopic scale ionization chambers do not provide enough spatial resolution. Indeed, for the quantification of dose delivered in MRT several detectors have been realized and studied to try to resolve the dose distribution of microbeams at micrometric scale. Two of the current most used high spatial resolution detectors are the MicroDiamond detector by PTW (PTW, Freiburg, Germany) and radiochromic films. The MicroDiamond is a solid state detector with a 1-dimensional spatial resolution of a few micrometres able of resolving microbeam features. Radiochromic films are passive detectors, used daily in conventional RT, that undergo optical density variation when interacting with ionizing radiation, making possible the quantification of the delivered dose. These two detector types will be used for dosimetry measurements in this work and more details about their structure and used will be presented in section 2.4.

Despite substantial improvements in experimental dosimetry at micrometric scale for MRT have been done in the past year, differences between experimental and simulated doses are often bigger than the 3% required for validating clinical applications. Part of this work is therefore focused on the understanding of possible causes of discrepancies between simulated and measured doses related to the radiation interaction with the MSC.

1.6.2. Dose calculation in MRT

In RT dose calculation is a fundamental tool for the estimation of the dose delivered during an irradiation. Various algorithms have been developed to calculate dose in simple and complex geometry. What makes dose calculation extremely challenging in MRT is an inhomogeneous fluence distribution of primary and secondary radiation particles, resulting in inhomogeneous dose distribution. Moreover, a small spatial scale in the order of micrometer is needed to resolve the microbeams dose distributions, bringing the necessity to manage big dataset. The most used approach in radiotheraphy with external photon beams is Monte Carlo (MC) radiation transport technique.

Monte Carlo simulations are based on the repetition of a stochastic process to obtain an estimate of the expectation value of a quantity by averaging the result of all histories observed. The error of a simulation is given by:

$$s(N) = \sqrt{\frac{<x^2> - <x>^2}{N}} \tag{1.15}$$

where N is the number of repetitions and x a random variable. Increasing the number of histories, the expectation values $<x^2>$ and $<x>^2$ converge to a constant and the estimated variance converges to zero. Thus, the precision of MC simulation increases by increasing the number of histories.

In RT, MC technique is used to simulate the path of particles of ionising radiation through matter, considering interaction probabilities calculated by theoretical models and defining a random and unique trajectory using a pseudo-random number of generators. The big advantage of the MC simulation is the high accuracy of the result. If the interaction probabilities of a certain particle type as a function of the material composition, mass density, and the particle energy are well known and described by a model or empirical data, this interaction can be modelled in the simulation. If the number of repetitions is large enough, the result converges towards the expectation value of the physical model. The simulation considers not only primary particles, but also all the cascades of secondary particles generated along the path. Only when all particles have lost their kinetic energy, i.e. they are absorbed by the medium, or the particles have left the regions of interest, the simulation stops to process those secondary particles. An important quantity for the definition of production cut threshold is the minimum energy a secondary particle must have upon its generation in order to be actually created and considered in the cascade of particles to simulate. This is called *scale of interest* and is useful to reduce the calculation time and the memory consumption.

The Monte Carlo toolkit used in this study for dose calculation in MRT is Geant4, acronym of *Geometry and Tracking*. It is written in C++ and provides an ensemble of classes which constitute the basic functions of a MC simulation and which the user can extend according to the specific requirements of the application.

In this work, MC simulations will be realized to calculate the transmitted spectrum after the interaction of the X-ray radiation with the MSC blades. This will be the starting point for simulations of the delivered dose inside a simple scenario of a cube of water. This may provide useful indications about discrepancies between simulated and measured dose distribution in MRT.

1.7. Aim of the project

Microbeam radiation therapy (MRT) is a developing radiotherapy that in the past decade has evolved from pre-clinical trials to a situation in which clinical trials could be planned. The spatially dose fractionation, i.e. the transition from a broad beam to microbeams, is done by means of a multislit collimator (MSC). The mechanical properties of this device are the most important factor required to produce an array of parallel and identical microbeams.

During the past 15 years, several different designs have been made for the creation of a reliable MSC, in order to obtain the most precise array of parallel microbeams with the highest peak dose and the lowest valley dose possible. The MSC present at the ID17 biomedical beamline of the ESRF since 2009 generates microbeams characterized by a nominal full width at half maximum (FWHM) of 50 μm and a c-t-c distance of 400 μm. To control the MRT irradiation, dosimetry protocols based on the use of dedicated MC simulations and specific detectors have been developed [28]. In contrast with RT, where uncertainties and differences between simulated and experimental dose values are typically below 3%, in MRT the variation between calculated and measured dose can be up to 10-30%, too high to make possible the begin of medical applications. Often most of the dose discrepancies are measured in valley regions where the measured doses are higher than the simulated ones.

Between the several factors influencing the dose distribution, one possible cause of the augmented valley dose is the radiation transmitted through the blade of the MSC or scattering on the inner wall of the MSC which may be not correctly modelled so far, increasing the valley dose measured between microbeams. Ideally, photons impinging on the MSC should be absorbed inside the metal blade, but this is not the case. In reality not all the photons are stopped by the slabs of the MSC and a small fraction is passing through the blades becoming primary radiation reaching valley regions. Moreover, the MSC blades may not be all perfectly aligned, defining variations in the aperture's geometries. For this reason, some photons could interact with the inner surfaces of the MSC, leading to a total reflection or scattering of the radiation, causing a change in the dose distribution that can bring to an increase of the valley dose during irradiation [30].

For this reason, a new MSC realized by mean of Densimet 185 material, a more recent tungsten-based alloy, has been recently purchased by the ID17 beamline with the prospective of improving the precision in the generation of microbeams for MRT applications, and more specifically of reducing the contribution of transmitted radiation through the MSC blades.

The present study has the objective of characterizing the Densimet MSC and comparing it with the MSC already used at the beamline. Radiation transmitted through the blades of the MSCs will be measured to understand if the Densimet MSC is actually more effective in absorbing the radiation of the incoming synchrotron beam, thus reducing the valley dose. Experimental dosimetry study and MC simulations are realized in simple and complex scenario in order to provide with both MSCs useful elements able to explain the differences between measured and calculated dose distribution.

1.8. Outline of the thesis

The outline of this manuscript is as follow:

- Chapter 2 presents the methods and materials used in the study. At the beginning, the design of the two MSCs used for this work are described, together with the characterization procedure, that includes the cleaning of the apertures, and the procedure used for their FWHM and c-t-c distance measurement. Following, the method used for calculating and measuring the spectra transmitted by the MSCs is described, together with the MC simulations of the transmitted spectra. The last part of the chapter is dedicated to the procedures used for dosimetry validation. Firstly, it is presented the method for measuring the dose delivered to the target with a microdiamond detector. Then the radiochromic film dosimetry protocol, performed in air and in a water equivalent phantom is described. The chapter ends with the presentation of the MC simulation of the dose delivered to the target.
- Chapter 3 presents all the results obtained from the calculation and experimental measurements described in the previous chapter. The comparison between measured data and simulation results is presented.
- Chapter 4 discussed the results obtained in the previous sections, together with some possible improvement in the method and further studies.
- Chapter 5 presents the main conclusions of the work.

2 | Material and Methods

2.1. Design of the multislit collimator

The multislit collimator (MSC) is the fundamental component of the beamline that transforms the homogeneous field generated by the synchrotron source into a spatially fractionated array of radiation. It is a mechanical component realized with high density tungsten alloys that shows a pattern of apertures with a well-established and defined periodicity. At ID17 biomedical beamline the most used MSC for MRT experiments is designed to generates microbeams characterized by a nominal full width at half maximum (FWHM) of 50 μm and a nominal center-to-center (c-t-c) distance of 400 μm. This MSC is made of CF-H25S+ (where CF stays for Corrosion-Free), a metal alloy of tungsten carbide (WC), cobalt (Co), vanadium carbide (VC) and chromium carbide (Cr3C2), with a density of 14.55 g/cm^3. Following in the manuscript, this MSC available at the beamline since 2009 will be mentioned as "CF-MSC".

A second MSC has been recently bought at the beamline with the same mechanical design of the CF-MSC, but it is realized with a more recently developed tungsten alloy named Densimet 185. The Densimet MSC is made of a metal alloy of tungsten (W), nickel (Ni) and iron (Fe) and it has a nominal density of 18.54 g/cm^3.

The precise chemical composition of the two MSCs is reported respectively in table 2.1 and 2.2.

CF-MSC

	WC	**Co**	**VC+Cr3C2**
Weight%	90.3	8.5	1.2

Table 2.1: Chemical composition of the CF-MSC.

Densimet 185 MSC

	W	Ni	Fe
Weight%	96.97	2.02	1.01

Table 2.2: Chemical composition of the Densimet 185 MSC.

The Densimet 185, with its higher concentration of tungsten with respect to the CF-H25S+ alloy, has properties closer to those of the pure tungsten and is expected to be more efficient in absorbing the radiation impinging on the blades of the MSC. Both MSCs are made of a 8 mm thick single copper block, hosting 125 individual blades fitted to obtain the desired aperture width and spacing of the microbeams array. This mechanical design was used because wire-cutting techniques are not precise enough for obtaining apertures less than 100 µm from a single metal block. Figure 2.1 shows a technical drawing of a single-stack MSC used at the ID17 Biomedical beamline.

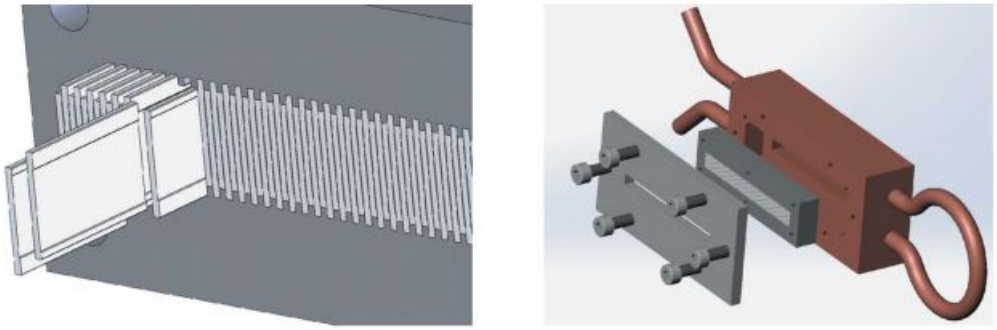

(a) (b)

Figure 2.1: Technical drawings of the single-stack MSC used at ID17 Biomedical beamline of ESRF [30]. (a) Representation of the technique used for assembling individual blades inside the metal block. (b) Geometry of the instrument used to mount the MSC on the metal stage.

For experiments, the MSC (CF or Densimet) is mounted on a metal base fixed on a rotational stage used for the alignment of the apertures inside the beam. A water-cooling system and a nitrogen gas flow inside the Aluminum box where the MSC is embedded to avoid overheating of the metal during irradiation.

2.2. Characterization of the multislit collimator geometry

2.2.1. Optical microscope study

The first step in the characterization of the two MSCs is the check of the cleanliness of the apertures. No information about the CF-MSC was available from past checks at the moment of the study. This step is fundamental to verify that small residues from the machining procedure are not stuck between blades. As it will be shown in the results, a cleaning action was needed for both MSCs and it was done by UNT (Usinage Nouvelles Technologies), the company that realized the two MSC. Practically, a foil 0.05 mm thick was passed between each blade, then vacuumed cleaned and blew with compressed air.

Digital images of the apertures before and after the treatment are acquired by means of an Inverted Optical Microscope with a micrometric resolution. The term *inverted* is related to the fact that the light source illuminates the optical system, placed at the base of the microscope, from the top. Between the light source and the optics, a stage holds the sample that is analyzed through light transmission. Below the stage, the optical system collects the light transmitted through the MSC placed on the stage. At ESRF ID17 biomedical beamline a Zeiss Axio Vert.A1 inverted optical microscope is used. Light is emitted by a temperature independent LED source in the range of 400 and 700 nm and a voltage between 1.5V and 12V is applied. The scanning stage, where the MSC is placed, it's able to move with 0.1 μm resolution. At the end the light is collected by a CCD camera that acquires and digitizes the images. The camera is black & white type with 12-bit resolution.

2.2.2. Data analysis protocol

To check the regularity of the aperture width and periodicity, the synchrotron beam is used. The procedure starts with the alignment of the beamline to define a beamlet only a few micrometers wide.

The beam generated by the wiggler device enters the optical hutch where two couples of vertical and horizontal motorized slits (primary slits) shape a rectangular beam 500 μm high and 300 μm wide to decrease the radiation entering the experimental hutch and therefore the background radiation. In the experimental hutch the width of the beam is further reduced to almost 15/20 μm using a motorized horizontal slit. A vertical aperture with fixed dimension of 0.52 mm defines the final beam height. The beam reaches the

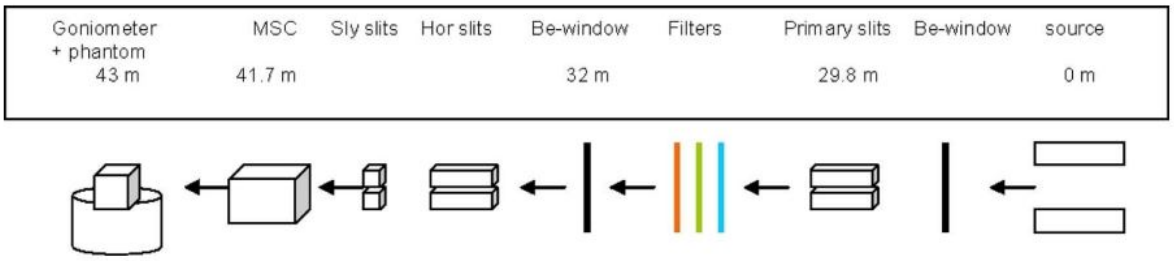

Figure 2.2: Sketch of MRT experimental setup starting with the source, on the right, and up to the target position on the left, with the corresponding distance of each element from the x-ray source [15].

MSC at 41.7 m from the source, as shown in figure 2.2, where a sketch of the MRT setup is presented.

The MSC is mounted above a stack of three different motors that allow the precise alignment of the collimator inside the beam. Two translational motors allow the displacement of the MSC in the plane perpendicular to the beam propagation direction and a rotation motor used to align the MSC apertures parallel to the beam. By an iterative process of adjusting these three motors, an alignment of the apertures with the beam can be achieved with a precision of $\pm 0.005°$.

To obtain the profile of each single microbeam, i.e. the radiation profile defined by each MSC aperture, horizontal scans of the MSC are done moving the component by means of the horizontal translation motor, in order to scan all apertures through the beam. The motor is moved for a range of 52 mm, by steps of 5 μm (motor resolution), thus obtaining a set of 10401 points per scan. The IC2 ionization chamber, located after the end of the experimental hutch, measures the radiation transmitted by the MSC apertures as a function of the MSC position.

Figure 2.3 shows the intensity profiles of the five central microbeams detected by the IC2. Each acquisition point of the profile is normalized with respect to the storage ring current present at the moment of the signal acquisition.

To calculate the FWHM of each microbeam and the c-t-c distance between microbeams a Matlab code is developed. First, each single microbeam is identified from the pattern and studied individually. By means of a Gaussian fit, the y coordinate of the center of the peak is found and then the peak intensity is calculated as average over the five central points. From this, the half height of the peak is obtained. A linear fit is then created between two points with the y value closest to $y = halfheight$ on both side of the peak.

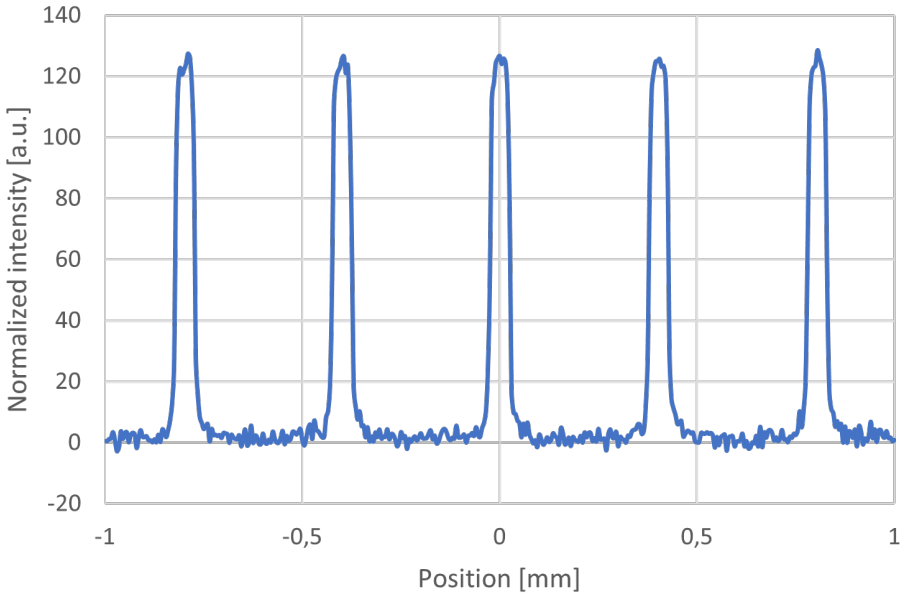

Figure 2.3: Intensity profile of five microbeams from the center of the MSC.

From this, the x value of the point on the left side of the peak and of the point on the right side of the peak at $y = halfheight$ is extrapolated form the linear fit. The FWHM is calculated as the difference between the x values of these two points, while the center of the peak as the average of their x values.

Afterwards, the same procedure is repeated iteratively for all microbeams. The c-t-c distance is finally calculated as the difference between the center of each adjacent peak.

2.3. Radiation transmitted through the multislit collimator blades

The Densimet MSC is designed with the main purpose of decreasing the transmitted radiation through the blades of the collimator and possibly of reducing the scattering events on the inner walls with respect to the CF multislit collimator already present at the beamline. The improvement in the use of the Densimet 185 as attenuating material is theoretically calculated starting by the National Institute of Standards and Technology (NIST) values and then experimentally measured by means of a semiconductor detector.

2.3.1. Theoretical calculation of transmitted radiation

The wiggler generated X-ray spectrum that impinges on the MSC is calculated using the OrAnge SYnchrotron Suite (OASYS) platform, as described in the work of Di Manici [25]. As presented in section 1.5, the raw spectrum generated by the wiggler device crosses a series of attenuators and monitoring detectors that attenuate the spectrum and change its energy profile. In this work, two spectrum configurations are considered: the *conventional spectrum*, used in most of the experiments, has the maximum intensity of up to 16000 Gy/s and a mean energy of 103 keV; the *clinical spectrum* has a higher mean energy of 120 keV, defined by mean of thicker attenuators, and it is defined for future possible clinical scenario in order to be more penetrating the matter and to reduce dose delivery in dense biological tissues such as bones.

Table 2.3 shows the detail of the beamline components crossed by the X-ray beam before reaching the target. Figure 2.4 shows on top the clinical and conventional X-ray energy spectra profile impinging on the MSC, while on the bottom, the figure shows the corresponding profiles normalization with respect to their maximum intensity value, highlighting the energy shift between the two configurations. The peak intensity in the conventional case is at around 80 keV, while in the clinical case is slightly higher around 90 keV.

Configuration	Conventional MRT	Clinical MRT
Be window [mm]	2.3	2.3
Attenuator 1: C [mm]	1.15	1.42
Attenuator 2: Al [mm]	0.28	0.28
Attenuator 3: Al [mm]	1.24	1.24
Attenuator 4: Cu [mm]	0.35	1.42
Attenuator 5: Cu [mm]	0.69	0.69
IC0	NO	YES
Al exit window [mm]	0.5	0.5
IC0bis	NO	PMMA

Table 2.3: List of the components and their thickness that the photon beam crosses before hitting the MSC. The two configurations of conventional and clinical spectra are considered.

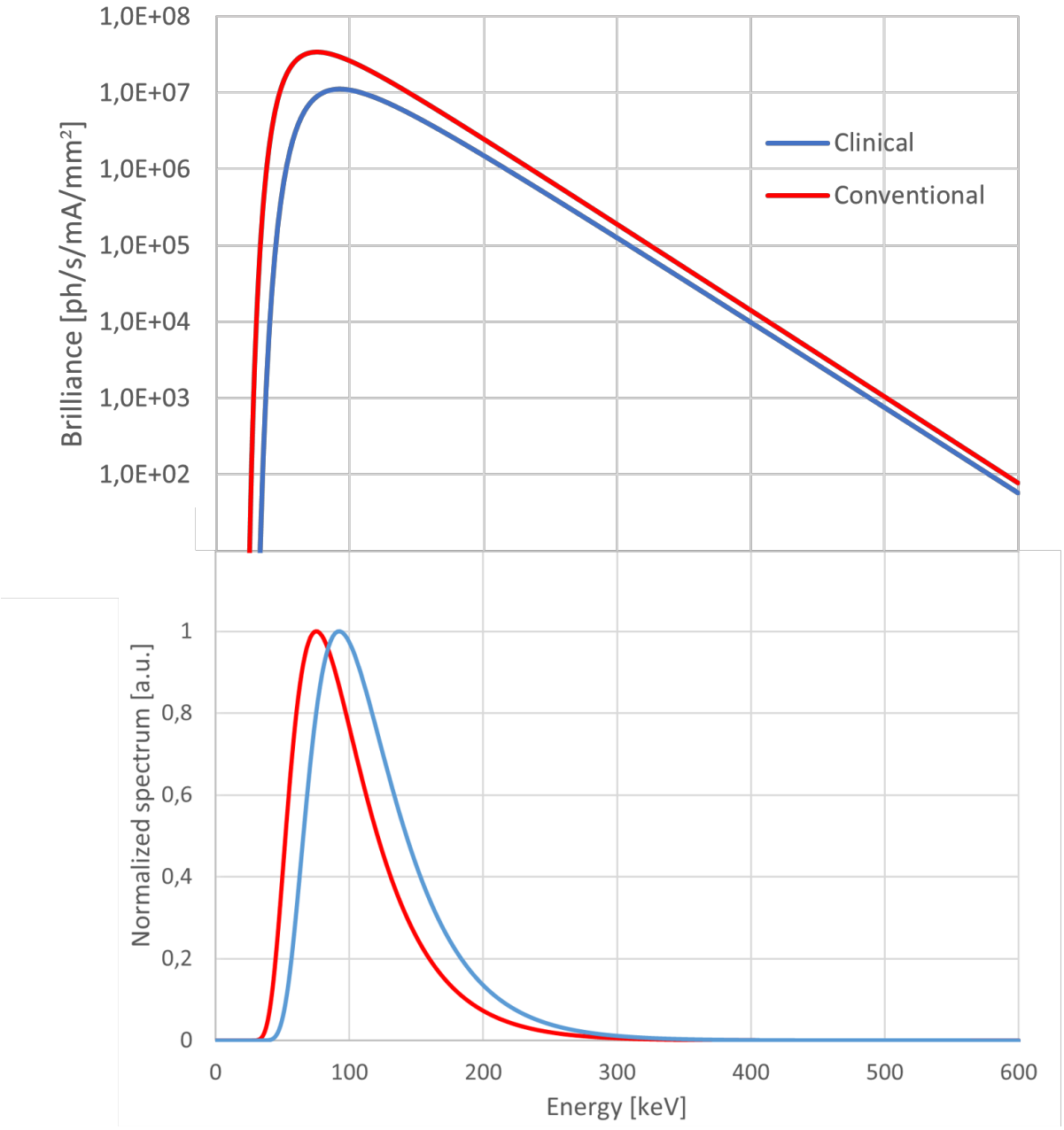

Figure 2.4: On the top, X-ray energy spectrum profiles impinging on the MSC considering the clinical (blue curve) and the conventional (red curve) configuration as a function of the photon energy. On the bottom the corresponding X-ray energy spectra profiles obtained after normalization with respect to the maximum intensity value.

While the X-ray beam arriving on the MSC in correspondence of the collimator aperture passes undisturbed and reaches the target, the radiation impinging on the MSC blades is mostly absorbed inside the collimator. The small part of transmitted radiation through the MSC blades can be calculated starting from the mass attenuation coefficients taken from the NIST database (Hubbell and Seltzer, 1996) and applying the Lambert-Beer law.

The latter describes the attenuation of a monochromatic beam of photons that arrives with an intensity I_0, penetrates a layer of material with a mass thickness x and a density ρ and emerges with a reduced intensity I, given by the following equation:

$$I = I_0 e^{-\frac{\mu}{\rho}x} \tag{2.1}$$

where the mass thickness x is the product between the thickness l and the density ρ of the material and $\frac{\mu}{\rho}$ is the mass attenuation coefficient. By entering on the NIST database energies from 0 keV to 600 keV with steps of 0.1 keV, the corresponding values of the photon mass attenuation coefficients in $\frac{cm^2}{g}$ considering just the coherent scattering (i.e. the photons that undergo a coherent scattering event are considered absorbed and not transmitted) is obtained. Knowing the density and the thickness of both MSCs it is possible to calculate the *transmittance*, i.e. the ratio between the light that is actually transmitted by the material and the incident radiation, as:

$$T = \frac{I}{I_0} \tag{2.2}$$

and straightforward the percentage transmittance:

$$\%T = \frac{I}{I_0}100 \tag{2.3}$$

Multiplying the transmittance with the X-ray spectrum for both clinical and conventional configuration, the transmitted spectrum through the blades of the CF and the Densimet MSC that arrives at the target is calculated. The spectrum transmitted by the blades of the Densimet MSC is expected to be more attenuated with respect to that obtained using the old MSC, providing an overall lower value of valley dose when equivalent irradiation parameters are used.

Figure 2.5 on top shows $\frac{\mu}{\rho}$ as a function of the photon energy for both CF and Densimet material as obtained from the NIST database, while at the bottom the percentage difference of the total attenuation coefficient of the Densimet 185 with respect to that of the CF-H25S+ material is shown. The mass attenuation coefficient of the Densimet 185 is overall higher with respect to the CF-H25S+ material: it is around 14% higher in the 70-140 keV energy range, and between 10% and 4% for photon energies above 250 keV. Having the MSCs equivalent thickness, the overall radiation transmission will be as well influenced by the material density that in the case of the Densimet 185 is 22% higher than the CF-H25S+ alloy.

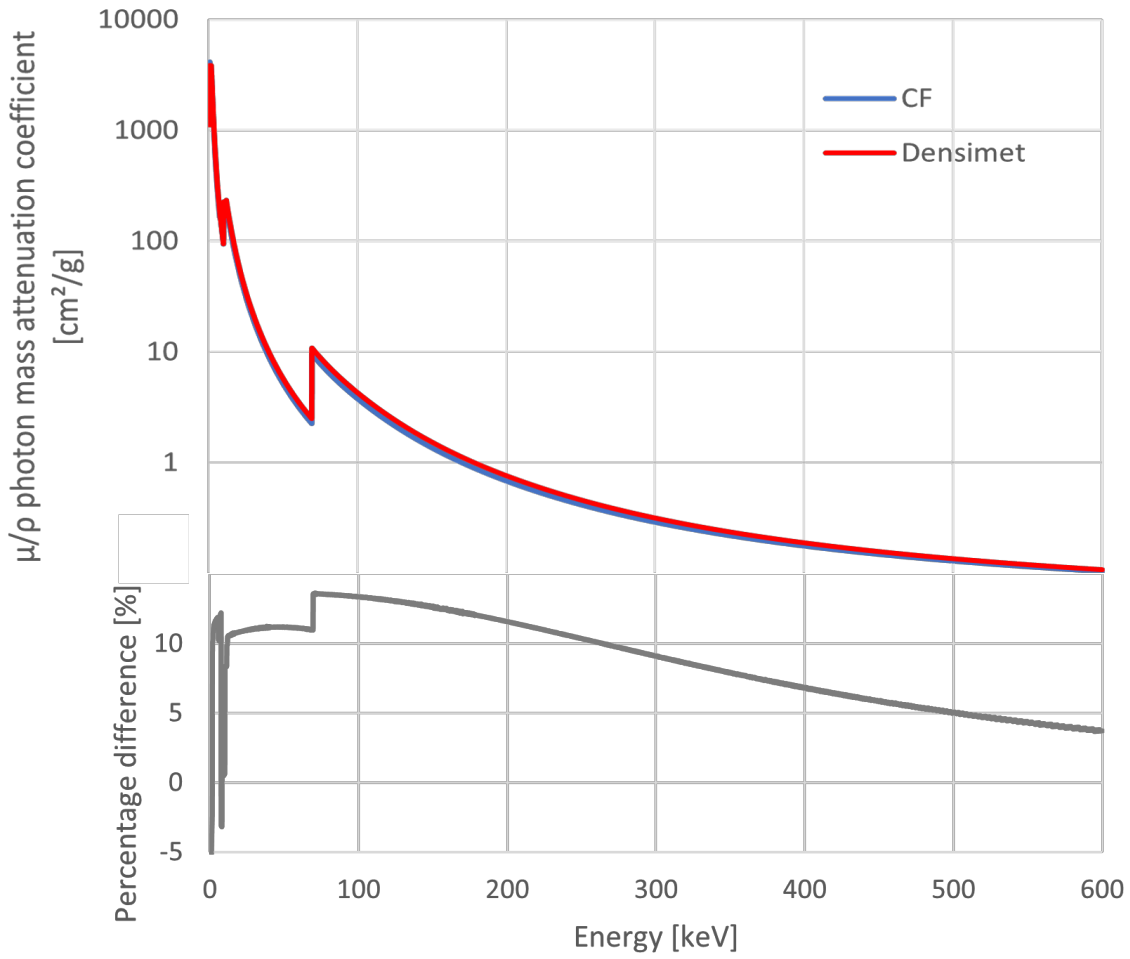

Figure 2.5: On top, plot of the photon mass attenuation coefficient $\frac{\mu}{\rho}$ represented as a function of the beam energy obtained from the NIST database for the CF-H25S+ and the Densimet 185 material in blue and red, respectively. On the bottom, the percentage difference between the two attenuation coefficients is shown.

2.3.2. Monte Carlo simulations of transmitted radiation

Monte Carlo simulations are prepared to confirm that the simulated spectrum passing through the blades of the MSC is matching the characteristics of the transmitted spectrum calculated starting from the mass attenuation coefficient of the NIST database. The Geant4 toolkit version 10 is used for the simulation.

The geometry of the simulation is modelling a single blade of the MSC, 350 μm wide, 3 mm high and 8 mm long. An X-ray radiation with energy distribution of the conventional and clinical spectrum is modelled as small beamlet, 350 μm wide and 500 μm high, impinging perpendicularly on the MSC blade. The photon energy of the radiation transmitted by

the 8 mm thick blade was recorded over a virtual $20 \times 20\ mm^2$ region in air, 1.3 m after the MSC position where the target is typically placed on the motorized stage for irradiation. The LivermorePolarized physics list is used as it is the more suitable for photon energy in the range used in MRT and include as well photon polarization, typical characteristic of the synchrotron radiation. 2.0×10^8 have been simulated for each configuration used.

The first step is focused on the possible difference between transmitted radiation including all the possible type of scattering events against simulations where only photons transmitted without interacting with the MSC are considered. Practically, in the simulation, this different approach is obtained by setting a different energy cut for scattered photons and secondary particles generated. When scattering events are considered, the energy cut is set to 1 nm, while for simulations focused only on transmitted radiation, the energy cut is set to 1 m. The simulation for the clinical spectrum configuration impinging on the CF MSC shows that a negligible difference is present in the transmitted spectrum when including or not the contribution of the radiation scattering within the MSC. Figure 2.6 shows the spectrum profiles obtained from this simulation.

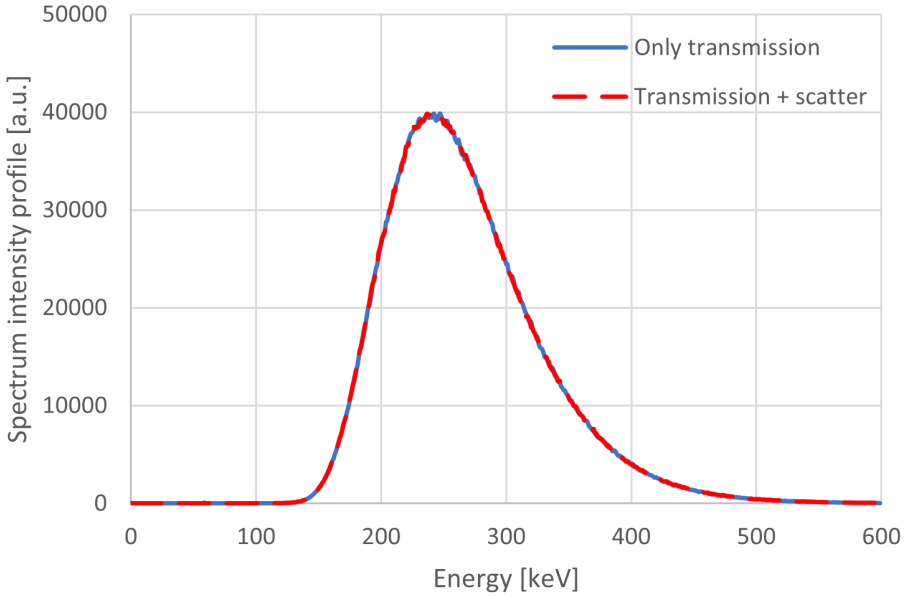

Figure 2.6: Spectrum intensity profiles of transmitted radiation by a single CF-H25S+ blade irradiated with the clinical spectrum showing the equivalence between the MC simulation model including only the transmission contribution in blue colour, and the spectrum profile considering the scatter contribution as well. The difference between the two configuration is negligible.

In order to reduce the calculation time that is significantly larger when all scattering contributions are included in the simulation, four simulations are prepared to model the

radiation transmitted by the two spectra used when irradiating both MSCs.

2.4. Dosimetry validation

In the following sections the methods and the detectors used for dosimetry measurement are presented. A PTW microDiamond detector is used to measure the dose transmitted by a small beamlet impinging on a single blade of the MSCs. Radiochromic film dosimetry for arrays of microbeams with different field sizes is after performed in air and inside a water-equivalent phantom. Monte Carlo simulations for dose calculation is performed for comparison with film dosimetry inside the phantom.

2.4.1. PTW microdiamond detector measurements

The microDiamond detector by PTW (PTW, Freiburg, Germany) is a solid state detector that runs in passive mode (zero applied bias) and is one of the most prolific diamond-based detector used in radiotherapy for dosimetry measurements. Developed by the University of Rome Tor Vergata and commercialized by PTW, it utilizes a synthetic single crystal diamond with a cylindrical shape of 2 mm diameter and 1 μm thickness as active volume. It has a high spatial resolution, able to solve microbeam features when operating in edge-on orientation, rather than in face-on orientation [13]. Figure 2.7 shows a schematic view of the two different orientations of the detector with respect to the incoming beam.

In this study the edge-on orientation is chosen in order to be sensitive at the radiation transmitted by a single MSC blade, as shown in figure 2.7 b. The microDiamond detector is not a pixelated detector and provides only a point measurement of the average dose delivered to the entire active volume. Only by scanning the detector inside the beam it is possible to record a dose profile or a 2-dimensional dose map.

By means of the beamline primary slits and the slits installed in the experimental hutch a 200x200 μm^2 field is defined and aligned to the center of the central blade (350 µm wide) of the MSC. The detector active volume is aligned with the center of the beam, and therefore with the center of the blade of the MSC. Measurements of the transmitted radiation are done considering both the Densimet and the CF multislit collimator, the clinical and the conventional spectra. Six central blades of each MSC are considered and for statistical reasons, for each studied blade three dose rate measurements are taken.

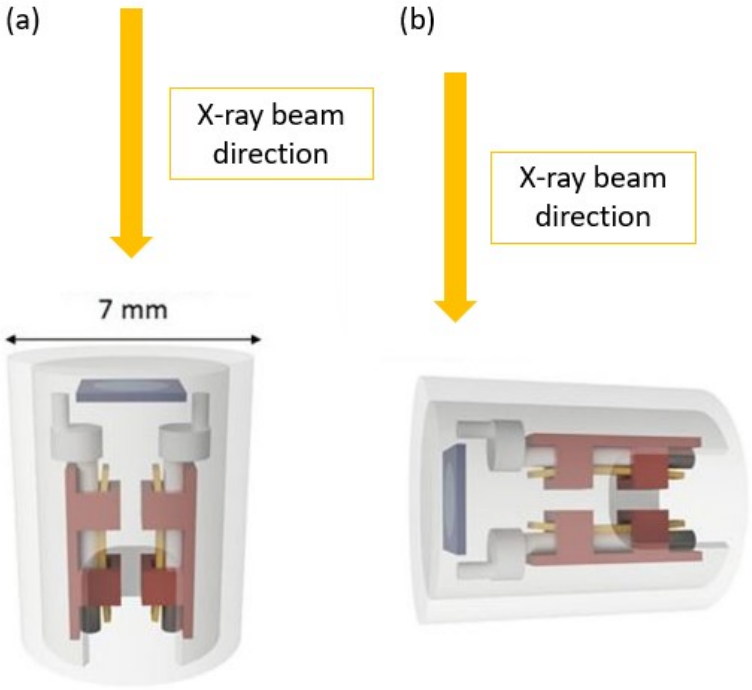

Figure 2.7: (a) Face-on orientation for a PTW microDiamond with a diameter of 7 mm, (b) edge-on orientation. The microDiamond has a centered rectangular representing the diamond size with central disc (blue) representing, to scale, the 1 μm thick sensitive volume [13].

2.4.2. Absolute dosimetry

Prior spatial fractionation of the irradiation field and film dosimetry, the measure of the beam dose rate is necessary. In general, absolute dosimetry is performed in radiotherapy using an homogeneous radiation field in order to ensure a correct dose delivery, following the instructions provided by the IAEA TRS 398 protocol. Ionization chambers (ICs) are the standard dosimeters in conventional radiation therapy. Figure 2.8 show a photo of the PinPoint chamber.

Cylindrical ICs are recommended for medium energy kilovoltage X-ray beam and therefore they are the dosimeters used in ID17 for reference dosimetry. Cylindrical ICs consist of an air cavity inside which the interaction of the incident radiation with air generates ions. At the center of the air cavity there is the collection electrode, while the inner conductive wall acts as external electrode. Applying a polarization voltage between the two electrodes, a motion of the charge created after ionization is induced. The IC measures the quantity of charge collected in Coulombs (C) which is directly proportional to the absorbed dose.

Figure 2.8: PTW PinPoint chamber 31014 [3].

At ID17 the IC used is the PTW PinPoint 31014 IC, because of its small sensitive volume (0.015 cm^2) that minimizes the saturation effect when performing measurements at very high dose rates.

The absorbed dose to water $D_{w,Q}$ is given by:

$$D_{w,Q} = M_Q \times N_{D,w,Q_0} \times k_{Q,Q_0} \tag{2.4}$$

N_{D,w,Q_0} is the IC calibration factor (Gy/nC) that is applied to the IC readings in order to convert the measured current into absorbed dose. It is a specific of the dosimeter and is provided by the metrology lab in terms of absorbed dose in water at reference beam quality Q_0.

If the beam quality Q is different from the reference Q_0, a beam quality correction k_{Q,Q_0} is needed, given by:

$$k_{Q,Q_0} = \frac{N_{D,w,Q}}{N_{D,w,Q_0}} \tag{2.5}$$

M_Q is the raw IC reading M_{raw} corrected for difference influence quantities k_i:

$$M_Q = M_{raw} \times k_i \tag{2.6}$$

Due to these influence quantities, several correction factors need to be applied to the IC reading:

- Temperature and pressure: the mass of air contained in the cavity and the ionization current measured depend on the atmospheric conditions at the time of the measurement. Thus, if the atmospheric conditions at the time of the measurements are different from those during the calibration, a correction factor $k_{T,P}$ must be applied:

$$k_{T,P} = \frac{P_0 T}{T_0 P} \tag{2.7}$$

  where T_0 and P_0 are the temperature and air pressure at the time of the calibration, while T and P are the temperature and air pressure at the time of the measurements.

- Polarity effect: some differences may occur if the in dosimeter reading depending if the polarization voltage is positive or negative. Polarity effect can caused by a parasitic radiation-induced current arising from secondary electrons produced by Compton effect in the wall and electrodes of the IC. Also the potential difference between the guard and the central electrode may have an influence on the polarity effect, causing polarity asymmetry. These effects are corrected by the k_pol factor.

- Ion recombination: if the applied voltage of the IC is not high enough the ions created inside the air cavity will recombine before reaching the electrode, resulting in an underestimation of the dose. The measured current depends on the applied voltage. Thus, the applied voltage must be increased until the recombination is reduced and the machine current is stabilized, in the so called saturation regime. However, ICs reading still need to be corrected for this effect by applying the ion recombination correction factor k_s.

- Electrometer calibration: k_elec is the correction factor for the electrometer calibration. It is determined by the metrology lab.

After considering the calibration and correction factors and global uncertainties, the treatment planning system is approved if the calculated dose and the measured dose match within a 3% of error.

Following the MRT reference dosimetry protocol, the IC is placed inside a LAP EASY

CUBE phantom. It is a water equivalent plastic phantom with a total dimension of 180 x 180 x 180 mm^3 with 10 mm thick removable slabs, as shown in figure 2.9. One of these slabs has a machined hole used for the insertion of the IC. This type of device is used instead of a water tank to simplify operational aspects of the measurement.

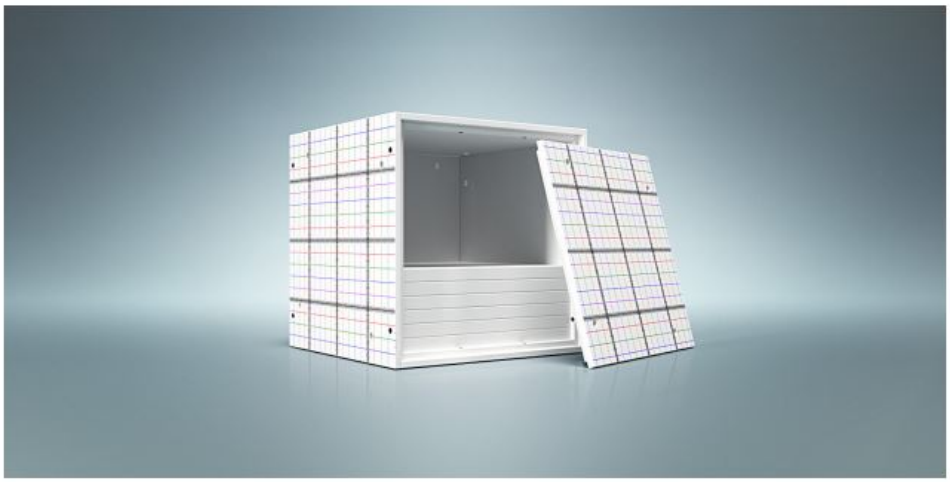

Figure 2.9: LAP EASY CUBE, water equivalent plastic phantom used for reference dosimetry.

The reference position of the IC is at 20 mm from the surface of the phantom. The IC is aligned with the active volume in the center of the 20 x 20 mm^2 field and scanned vertically in front of the broad beam, as shown in figure 2.10, with the multislit collimator moved out of the beam. Knowing the dose measured by the IC, the beam height, the synchrotron storage ring current and the vertical speed of the stage at the moment of the irradiation, the dose rate evaluation under reference condition is done. Indeed, the dose measured by the IC is [31]:

$$D = \frac{z_{beam} \cdot \dot{D}}{v_z} = \frac{z_{beam} \cdot \dot{D}_{scaled}}{I \cdot v_z} \tag{2.8}$$

where D is the measured absorbed dose (Gy), $\dot{D}$ the dose rate (Gy/s), z_{beam} the beam height (mm), v_z the scan speed (mm/s), I the current in the synchrotron storage ring and $\dot{D}_{scaled}$ the dose rate scale by the SR current (Gy/s/mA). $\dot{D}_{scaled}$ can be deduced from the measured dose, allowing the determination of the scan speed to be used in order to deliver the wanted dose during the irradiation. At ESRF, indeed, the Synchrotron Radiation current decays in time so the scan speed, depending on the desired dose, must be adapted to the machine current.

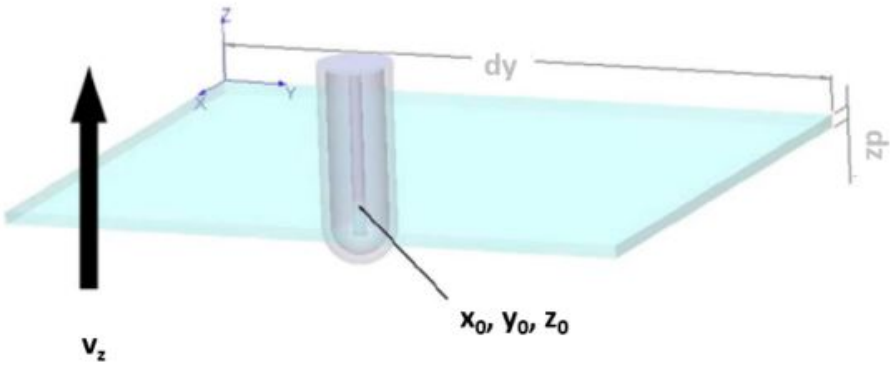

Figure 2.10: Drawing of the scanning technique of the PinPoint Ionization Chamber used to measure the odse rate in reference conditions [31].

2.4.3. Film dosimetry

Radiochromic films (RCF) are well established detectors in radiotherapy applications and are daily used in hospital to validate treatment plans before patient treatment. RCF are made as thin flexible sheets of clear polyester coated with an active material, typical emulsion, that chemically react when crossed by ionizing radiation. RCF provides a 2-dimensional dose distribution of the irradiation fields with a resolution of a few micrometers. For this reason, RCF are interesting detectors for measurements. The films used in this study are the GAFchromic films produced by Ashland company [34].

The active material of modern RCF is made of crystalline polyacetylee, usually diacetylenes such as the pentacosa-10,12-diyonic acid, the one chosen for recent Gafchromic films. This material has the characteristic of undergoing a polymerization process under exposure to heat or radiation, creating polymer chains that increase in length with the level of exposure. In figure 2.11 is shown an example of polymerization chemical reaction of a monomer of length 0.75 μm, on the left before the exposure and on the right the result of the polymerization after the exposure to radiation.

As a consequence of the polymerization process, the optical density (OD), i.e. the film absorbance changes after irradiation. This variation is the quantity to be measured to determine the delivered dose. It is defined as:

$$OD = log_{10}\frac{I_0}{I} \tag{2.9}$$

where I_0 is the initial transmitted intensity and I is the transmitted intensity after the film irradiation.

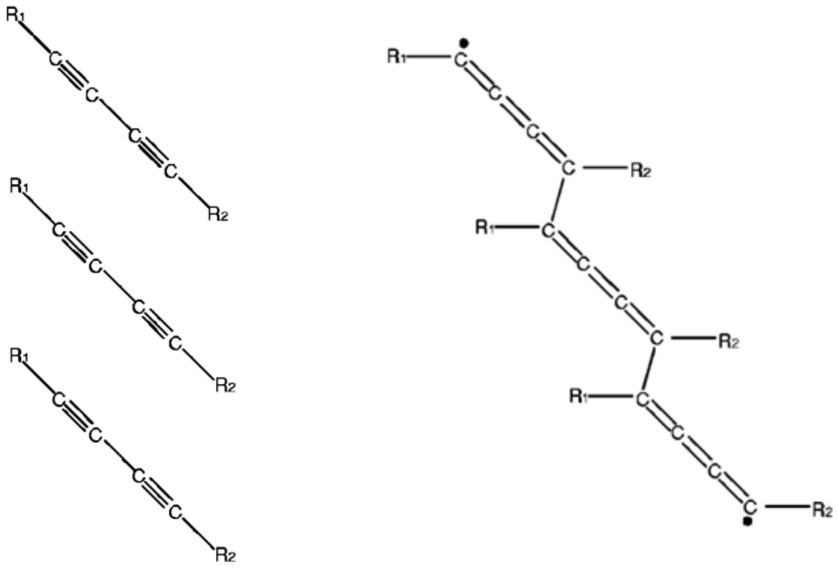

Figure 2.11: (a) Diacetylene monomers before the exposure to radiation and (b) the resulting polymer chain due to polymerization after the exposure to radiation [28].

The OD is measured as the transmitted light trough the film and it can be recorded by different densitometry techniques. In this work, the same inverted optical microscope described in section 2.2.1. is used for the digitalization of the films. Therefore, the OD is defined starting from the colour value of the acquired digital image.

For this study the third generation of Gafchromic films, EBT3, is used. Several publications can be found in literature describing the properties and characterizations of EBT3 films [17, 19]. The EBT3 film design is characterized by a symmetric structure: the active layer of 28 μm thick is sandwiched between two clear polyester layers of 125 μm thick. The structure of the film is reported in figure 2.12. This film is able to provide a 2-dimensional dose maps distribution with a nominal resolution of at least 25 μm.

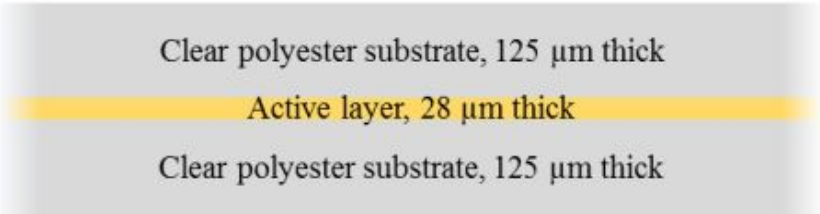

Figure 2.12: Structure of the EBT3 Gafchromic film. [28].

EBT3 film are sold in sheet with a dimension of 8 $\times$ 10 $inches^2$ (20.32 $\times$ 25.4 cm^2) and they can be cut in small pieces for irradiation. For this study, the film sheet was divided into 6 columns and 8 rows, obtaining 48 smaller tiles with an area of 30 $\times$ 30 mm^2. Each

small film is marked with a point in the upper-right angle, to assure that all films are irradiated with the same orientation, and with an alphanumeric code to easily identified each piece of film. Being light sensitive, RCF are put inside a protective aluminum foil in order to preserve the OD and they are exposed to external light just for irradiation and read-out. Part of the film pieces are used for the film calibration and part for microbeam irradiation. Due to their thin structure, radiochromic films can be used in several different experimental setup without perturbing the irradiation outcome. Typically, radiochromic films are placed between the plastic slabs of phantoms or also close to biological samples as monitoring devices of the irradiation field.

Calibration curve

To perform absolute dose measurements using RCF, the definition of a calibration curve under reference conditions is necessary. Prior irradiation of spatially fractionated fields, RCF are irradiated with an homogeneous field and a known dose well defined under reference conditions, as previously described in section 2.4.2. The OD of the calibration films measured after irradiation is matched with the delivered dose to create the calibration curve. The delivered dose and the number of films irradiated for the calibration must be chosen in order to cover all the dose region of interest. For this study, 9 films are irradiated with a 20x20 mm^2 homogeneous beam and placed in a water equivalent phantom at 20 mm depth from the phantom surface. The values of dose for calibration used are 1, 3, 5, 7, 10, 15 Gy. The irradiated films are digitalized and analyzed by means of a Matlab program in-house developed by P. Pellicioli et al. [29]. The final calibration curve is created fitting a rational function suggested by Lewis et al. [24]:

$$D(x) = a + \frac{b}{x - c} \tag{2.10}$$

where x is the gray value obtained from the image, $D(x)$ is the delivered dose, a, b, c are constants to be determined by fitting. This suggested function describes the OD change of the film with a coefficient of determination higher than 0.99.

Figure 2.13 shows the calibration curve obtained by the 6 films irradiated with a broad beam under reference conditions. After the creation of the calibration curve, the dose delivered to films not irradiated under reference conditions can be easily derived by comparing the grey value obtained by the film digitalization with the calibration curve.

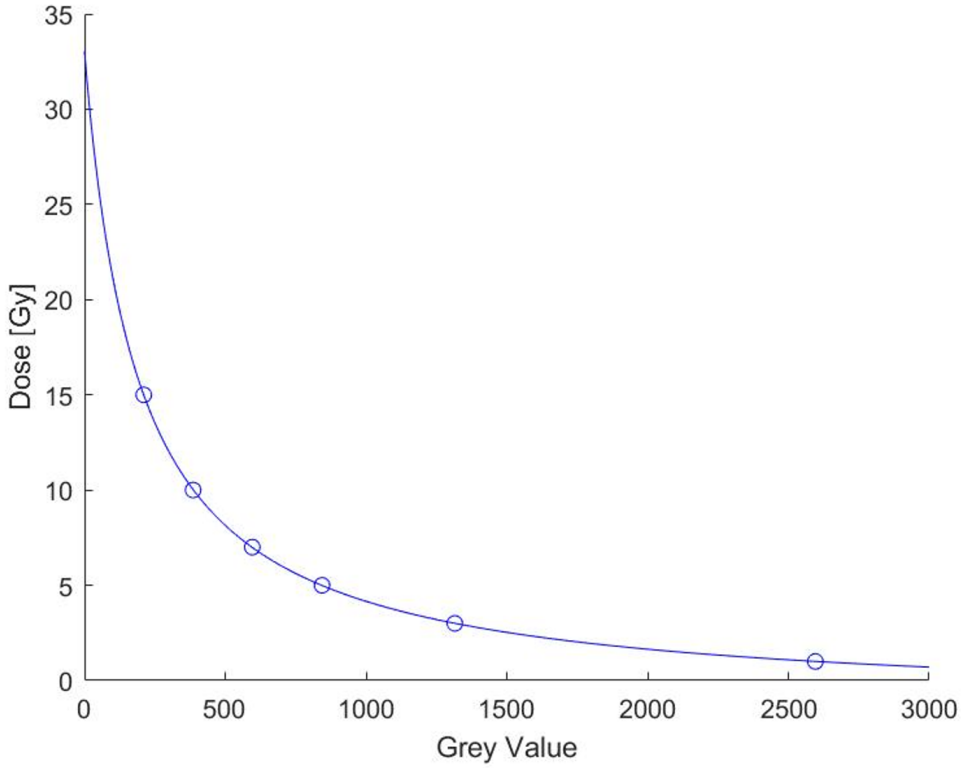

Figure 2.13: Calibration curve defined using 6 RCF irradiated with a broad beam under reference conditions.

Film irradiation in air

After the definition of the calibration curve, the films irradiation with microbeams arrays is performed by moving the MSC along the beam path. Two different exposure setups are used in this study: firstly, films are irradiated in air to be more sensitive only to the beam variation due to the interaction of the radiation with the blades of the two MSCs and secondly, films are irradiated at different depths inside the water-equivalent plastic phantom. In this second configuration, the scattering of the radiation inside the phantom volume is considered as well, recreating irradiation conditions that are more similar to clinical scenarios.

For film irradiation in air, the samples are aligned with the center of the beam with ± 1 mm precision by means of external lasers previously aligned to the beam position over the sample stage. Films are irradiated one at a time. To hold the film straight, vertically aligned and perpendicular to the beam, two metal frames with a square hole at the center are used. Figures 2.14 and 2.15 show the final setup used for film irradiation in air with the details of the entire sample holder.

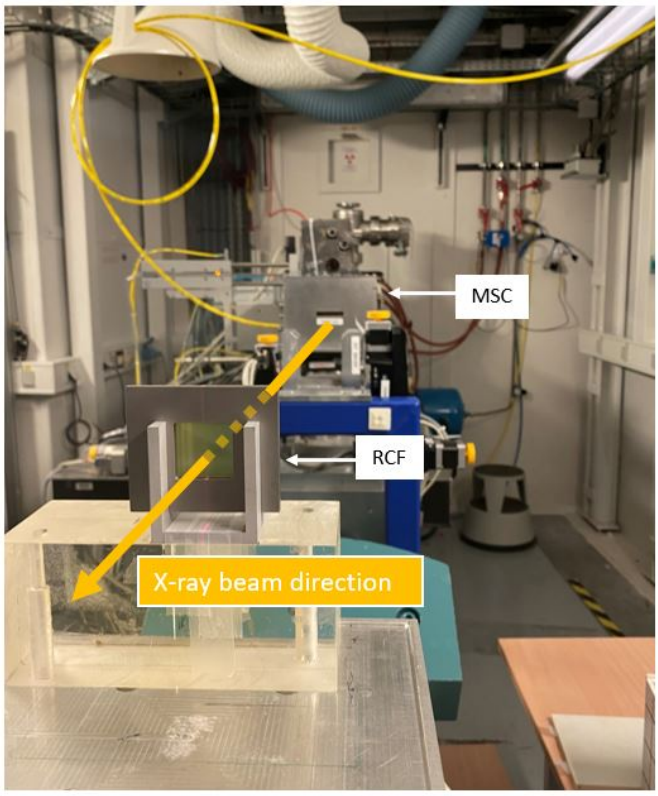

Figure 2.14: Photo of the setup used at ID17 for film irradiation in air.

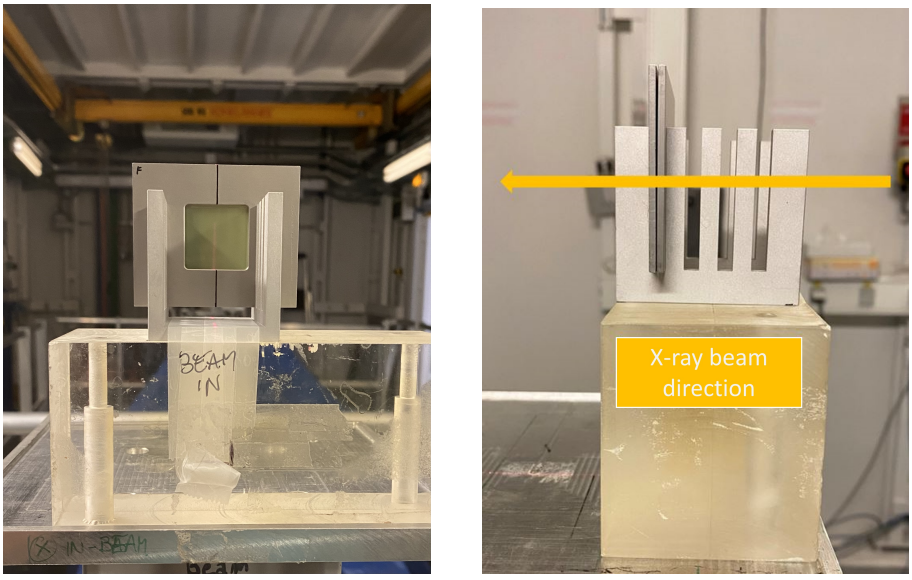

(a) Frontal view. (b) Lateral view.

Figure 2.15: Photo of the details of the film holder realized for the sample irradiation. The film is sandwiched between two metal frames and placed in an aluminum guide for irradiation.

For the study in air, the conventional and the clinical spectrum are used and three field size are considered: 20x20 mm^2, 10x10 mm^2, and 5x5 mm^2. For statistic reasons, three films are irradiated for each configuration of spectrum, MSC and field size used. For the dose evaluation of the valley doses, the four central valleys of each field are considered, obtaining a statistic over a total of twelve valley dose values for each field size. A total of 36 films are irradiated. The peak dose delivered is of 700 Gy. This dose is well out of the calibration curve range but its measurement is not the focus of this study. The peak dose for each irradiation is then adjusted in order to fit the valley dose inside the calibration curve range.

Film irradiation in a water-equivalent plastic phantom

To quantify the variation of the valley dose due to the use of the two different MSCs in a more realistic conditions of bigger targets, films are placed inside the water-equivalent phantom at the depth of 3 mm, 5 mm, 10 mm and 20 mm for irradiation. In this case the main valley dose contribution is connected to photons that undergo several scattering events when crossing the cube. This scattering contribution to valley dose is dependent to the energy of the spectrum and the field size for a given geometry of the microbeam pattern. The contribution of the transmitted radiation through the MSC blades is then added on top to the dose deposited in the valley region due to radiation scattering inside the target.

Films are placed between the slabs of the phantom for irradiation at the different defined depths. For time reason, only the clinical spectrum is used for this study, and three different field size: 20x20 mm^2, 10x10 mm^2, 5x5 mm^2. To improve statistic, two irradiations are performed for each depth and the dose values of four different valleys was measured for each irradiation, obtaining a total of eight valley dose values for each depth. Measurements are done for both the CF and the Densimet MSC, for a total of 48 films irradiated. The dose delivered to the films (as in reference condition) is 100 Gy when using a field size of 20x20 mm^2, 150 Gy when using a field size of 10x10 mm^2 and 200 Gy when using a field size of 5x5 mm^2. For small fields the radiation scatter contribution is smaller than bigger fields therefore, in order to bring the valley dose to a value well center in the calibration curve, the delivered peak dose is higher in small fields with the same experimental setup. The films are then digitized and analyzed and the gray value is compared with the calibration curve in order to derive the corresponding dose value.

Figure 2.16 shows a picture of the two plastic slabs of the phantom between which a film is sandwiched during the irradiation.

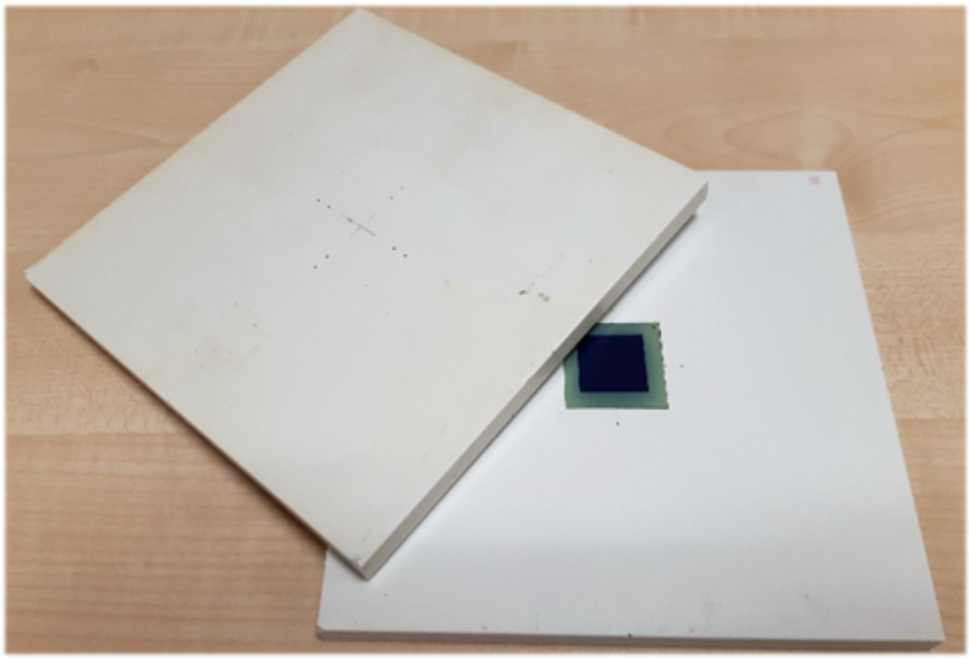

Figure 2.16: Picture of two plastic slabs from EASY CUBE phantom with a film irradiated in the center.

Film read-out

After the irradiation, the chemical reaction of the radiochrmic film active layer takes up to a few days for stabilizing to the final state. The OD, indeed, changes extremely rapid during irradiation (most of the variation develops within few milliseconds), but during hours and even days after some chemical reactions can continue. For this reason, the read-out of the films is done around one week after the irradiation to be sure that the OD stabilization can be considered concluded. The film digitalization is performed using the same Inverted Optical Microscope described in section 2.2.1, suitable for film analysis thanks to its micrometer resolution, small uncertainty, high precision and accuracy. Digital images are taken with a CCD camera. The output is a 2-dimensional array with integer gray values between 0 and 4095 and a resolution of 1.3 μm per pixel. Figure 2.17 shows as example two digital images of films irradiated by broad beam on the left and by microbeams on the right.

By means of Matlab program in-house developed at the beamline [29], the digital images are analyzed to convert the image color to the corresponding dose value for each irradiated area.

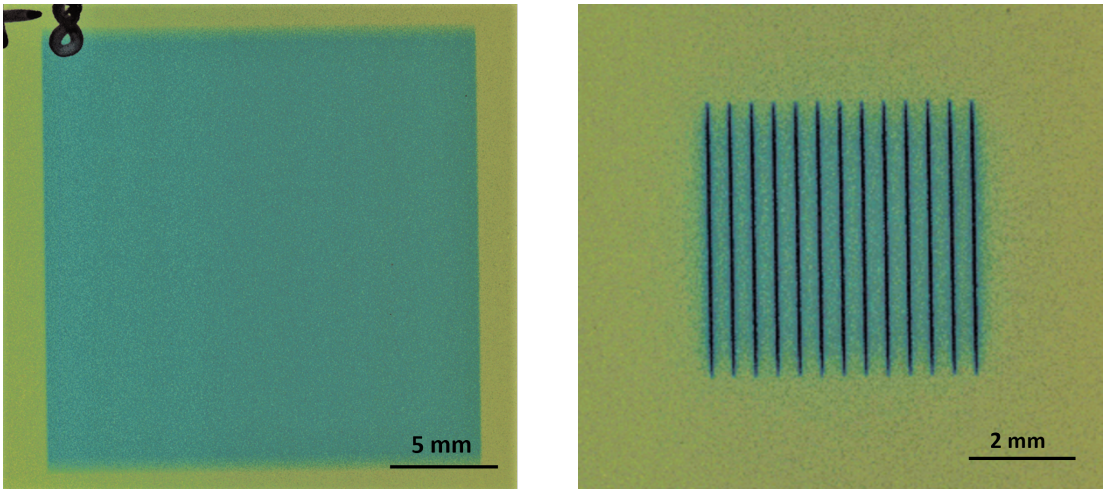

(a) (b)

Figure 2.17: EBT3 films irradiated with a broad beam (a) and with an array of microbeams of 50 μm wide spaced by 400 μm pitch (b). The irradiated field size is 20×20 mm^2 for the broad beam and 5×5 mm^2 for the microbeams.

2.4.4. Monte Carlo simulations of valley depth dose profile

Monte Carlo simulations is used to simulate the dose delivered by an array of microbeams to a water equivalent phantom using the clinical spectrum. The study focuses on the calculation of the valley dose when the two different collimators are used and different fields size of 5x5 mm^2, 10x10 mm^2 and 20x20 mm^2 are defined, as used for film dosimetry. The microbeams array has the typical geometry of 50 μm wide beams spaced by 400 μm pitch. The volume of the phantom interested by the irradiation field is discretized in voxel 10 μm wide in the horizontal direction (perpendicular to the vertical microbeams) to resolve the dose modulation. Vertically and along the beam propagation direction, a resolution of 1 mm is used to increase the statistic of particle interacting in each volume and reduce the calculation time. Along these directions, the dose variation study can be considered acceptable even if not considered at micrometric scale.

To efficiently model the radiation transmitted by the collimators in the simulation, the array of microbeams is not modeled as the homogeneous synchrotron beam hitting the MSC blades, because seven eighths of the photons would be mainly absorbed inside the MSC volumes, increasing the calculation time to obtain a good statistic for valley doses inside the target. By opposite, a "two-simulations" approach is used. Firstly, an ideal array of microbeam is simulated, with photons only starting from the peak region. Secondly, considering the results shown in section 3.2.1. on the spectra transmitted by the MSC

blades, a simulation considering the radiation transmitted only in correspondence of the valley region is done. The number of simulated photons for the second simulation is properly adjusted considering the microbeam array geometry and the MSC material used. For the simulation of the primary microbeam, 50×10^9 photons are simulated. The corresponding simulations for the transmitted radiation through the MSC blades is of 227.0×10^6 photons for the CF MSC and 67.7×10^6 photons for the Densimet MSC. The uncertainty on the simulated doses is only less than 0.5% with the number of photons used.

The analysis of the depth dose profile obtained is focused on the valley dose relative differences when the two MSC are used. For time reason, an entire characterization of peak and valley dose will be performed in future studies. Section 3.3.3. reports the results of the MC simulations.

3 | Results

3.1. Characterization of the multislit collimator geometry

3.1.1. Inner walls characterization

The results after cleaning of the apertures for both MSC can be easily verified by images acquired with the optical microscope. Figure 3.1 and 3.2 shows images for the comparison of the situation, on the left, before the cleaning and , on the right, after the cleaning of the apertures for both the CF and the Densimet MSC, respectively. From the following figures it is possible to recognize how the cleaning process greatly reduces debris between the apertures. In the case of the CF MSC, whose apertures are shown in figure 3.1, the improvement is more significant. The result of the cleaning shows an almost perfect definition of the apertures.

3.1.2. Apertures dimension and spacing periodicity of the MSCs

The results of the analysis of the collimators geometry obtained using a small synchrotron beamlet only 15-20 μm wide are reported in this section.

Figure 3.3 shows the measurement of the FWHM of each aperture of the CF MSC.

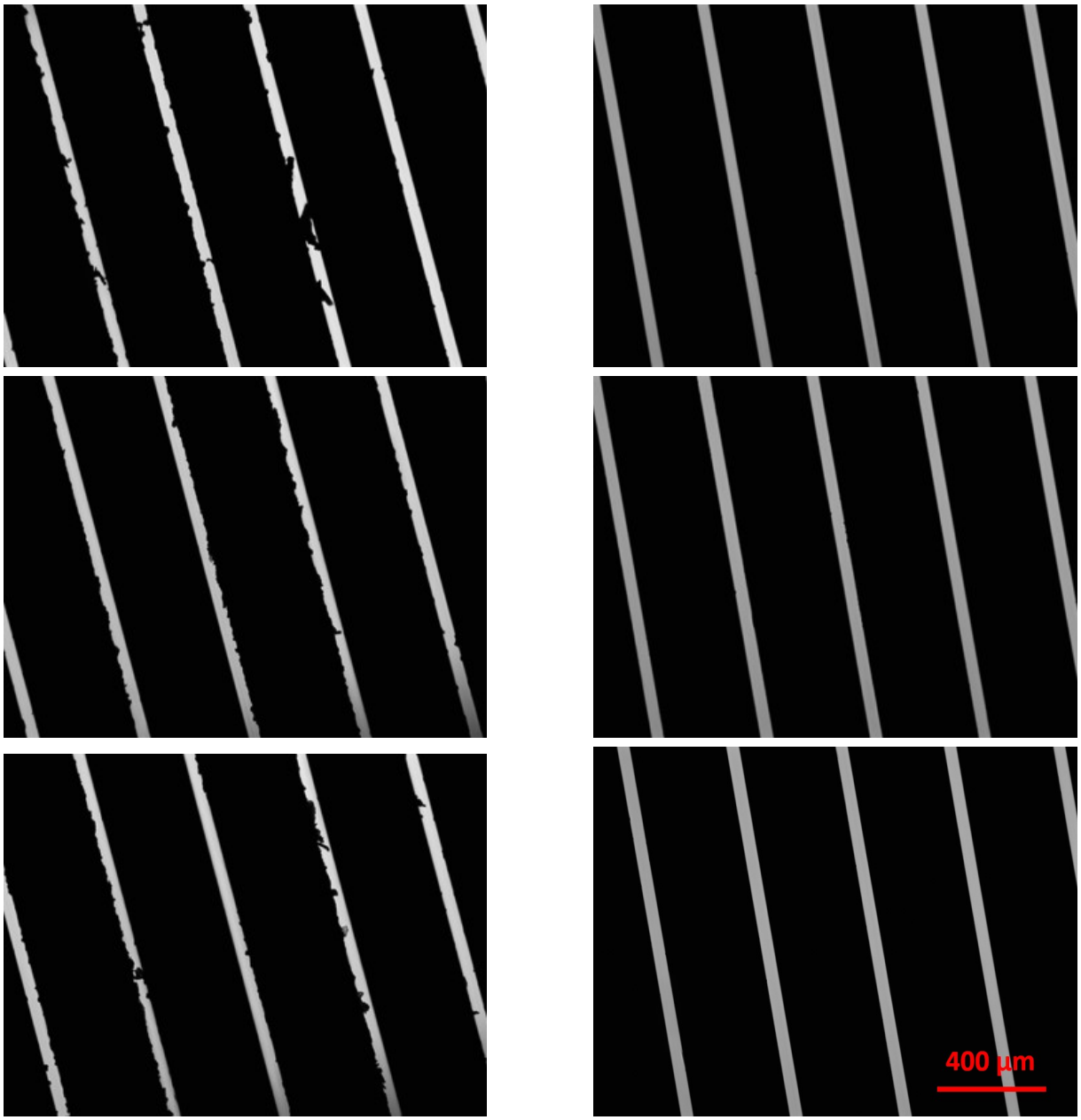

Figure 3.1: Images of the apertures of the CF MSC obtained using an inverted optical microscope: on the left images done before the cleaning process, on the right images done after the cleaning process.

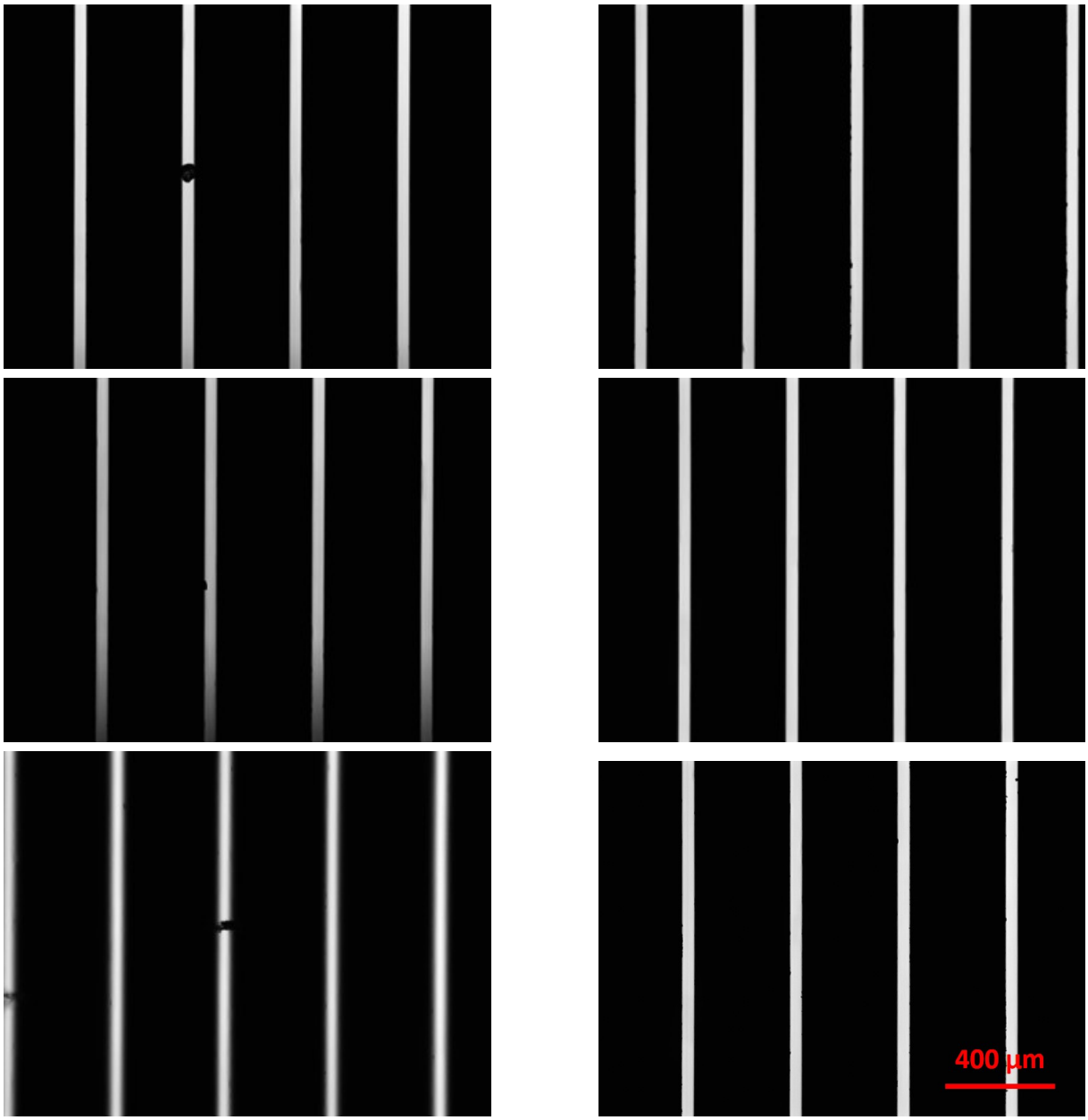

Figure 3.2: Images of the apertures of the Densimet MSC obtained using an inverted optical microscope: on the left images done before the cleaning process, on the right images done after the cleaning process.

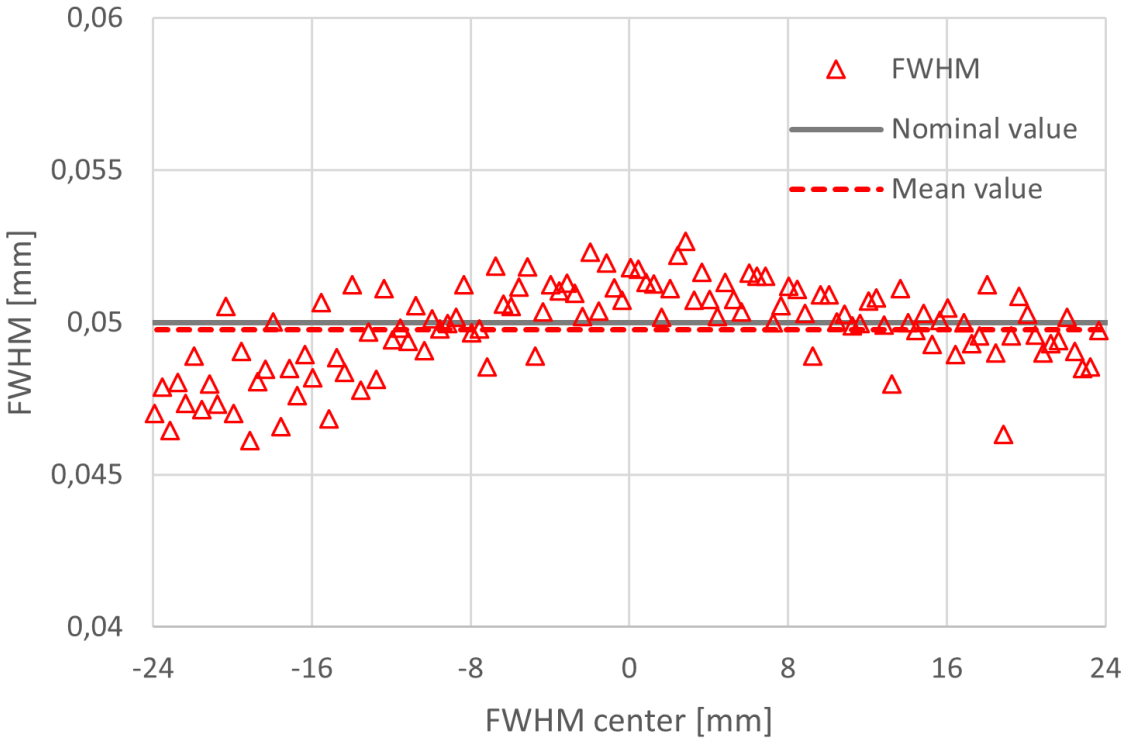

Figure 3.3: Plot of the FWHM measured for each aperture of the CF MSC.

The FWHM of the apertures of the CF MSC is around 52 μm in the central part while it drops down to around 47 μm at the edges. The average value of the FWHM is 49.78 μm, really close to the nominal value of 50 μm, with a standard deviation of $\pm$1.43 μm (2σ). These variations are probably due to limits in the fabrication process and cannot be easily corrected. Possible explanations are: a non-precise machining of the MSC blades or more probable, looking at the tendency of the FWHM values, a misalignment of the blades occurred during the assembling of the device. To be mention: this results in the FWHM value coincide with the ones obtained by E.Bräuer-Krisch et al.[15], demonstrating their validity and reproducibility of the procedure used.

Figure 3.4 shows the c-t-c distance obtained for each couple of consecutive apertures, together with the mean values.

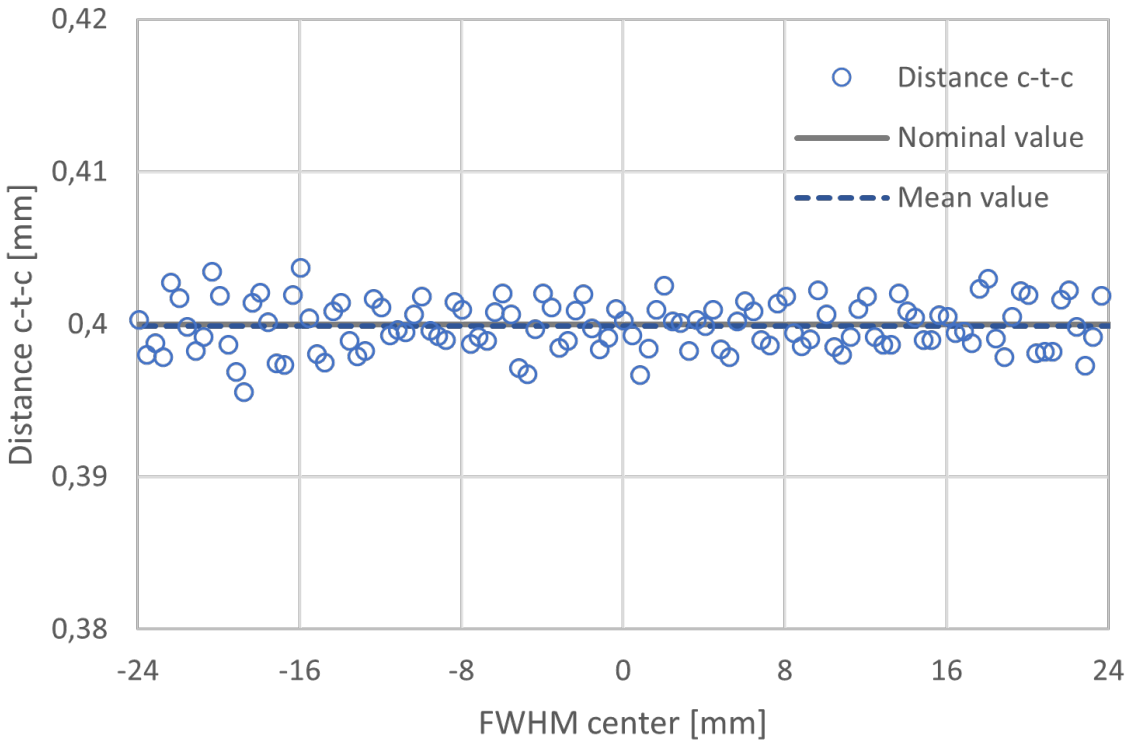

Figure 3.4: Center-to-center distance between consecutive apertures for the CF MSC.

The values measured for the center-to-center distance are randomly oscillating between a minimum of 397 μm to a maximum of about 403 μm. The average c-t-c distance is 399.87 μm with a variation of ± 1.66 μm (2σ), very close to the nominal value of 400 μm. From the obtained data, no specific trend is observed therefore the variations of this metric could be caused by possible uncertainties in the measurement procedure or as well due to mechanical imperfections.

Following the same approach, the analysis is now reported for the study of the Densimet MSC geometry. The FWHM distribution together with the nominal and mean values are shown in figure 3.5.

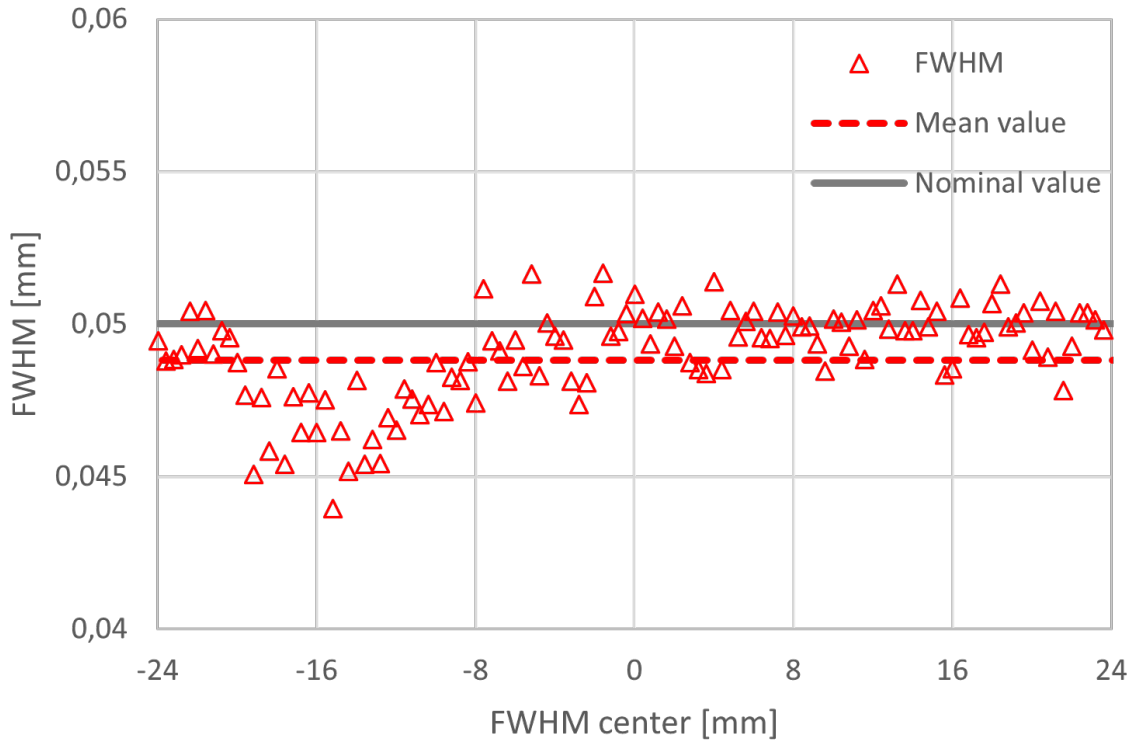

Figure 3.5: Plot of the FWHM measured for each aperture of the Densimet MSC with the beam aligned with the three central apertures.

The average value of the apertures FWHM is almost 50 μm $\pm$1.5 μm for motor positions between -8 and 24 mm, but around motor position -15 mm the apertures width is greatly reduced, down to around 45 μm $\pm$1.5 μm. This suggests the presence of a blade misalignment in a region of the Densimet MSC. To confirm this assumption and discard the possibility of a mechanical error in the definition of the aperture dimension, a new scans was taken after having redefined the aligned of three apertures located at position -15 mm. Figure 3.6 shows the FWHM distribution after the new alignment.

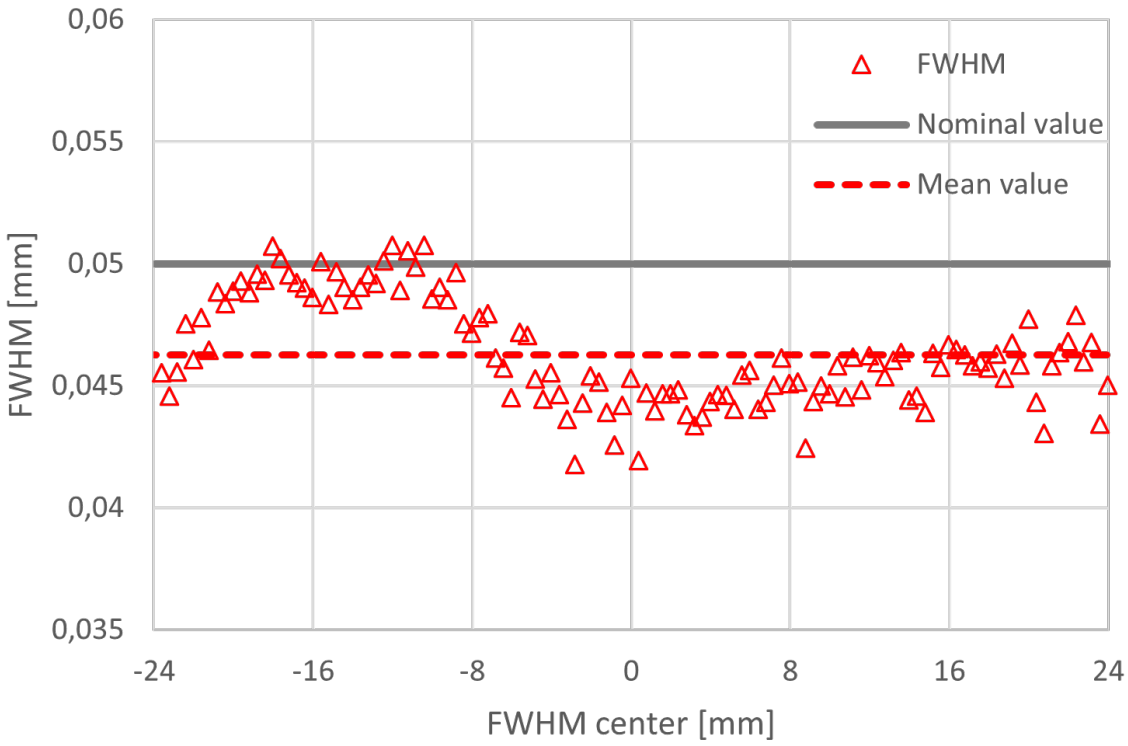

Figure 3.6: Plot of the FWHM measured for each aperture of the Densimet MSC with the beam aligned with the three apertures located at position -15 mm.

As it can be easily observed, the apertures FWHM around position -15 mm is restored to a value of 50 μm $\pm$1.5 μm confirming the misalignment of the blades, while on the other side, the aperture FWHM is reduced to a value of about 45 μm $\pm$1.5 μm. This confirms that the Densimet MSC is really characterized by an irregular pattern of apertures. Indeed, the misalignment of the blades could cause a reduction of the transmitted radiation and so of both the peak and valley dose.

By opposite, the c-t-c distance, as it can be observed in figure 3.7 and 3.8, remains constant for both alignment angles of the MSC. The average value is 399.85 μm $\pm$2.24 μm (2σ) in the first case, and 399.86 μm $\pm$1.95 μm in the second case, almost equivalent to the nominal value of 400 μm.

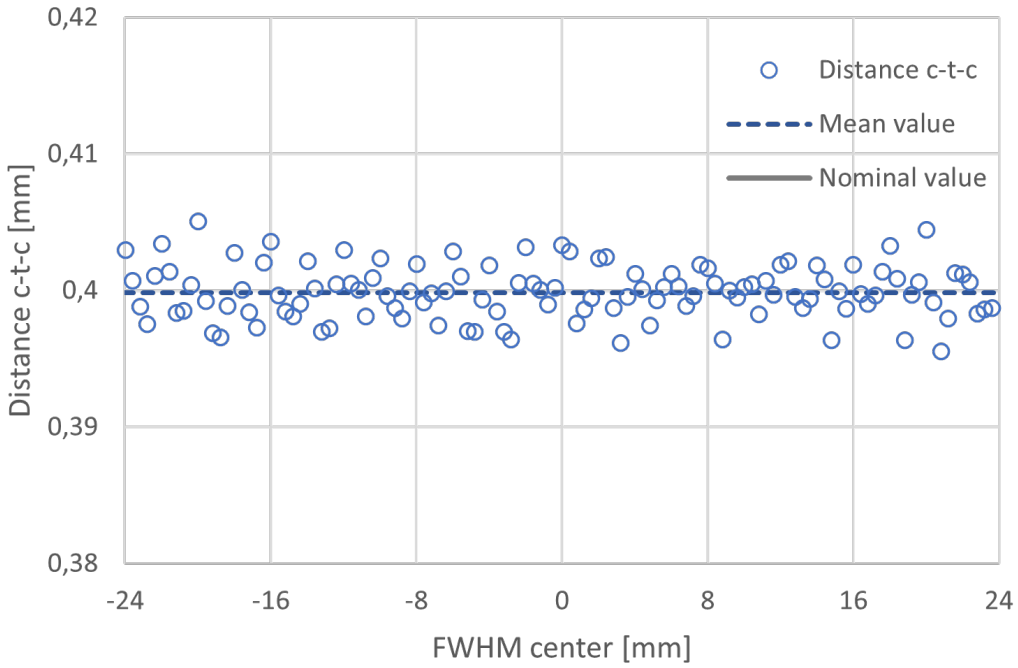

Figure 3.7: Center-to-center distance distribution between the apertures of the Densimet MSC and with the MSC aligned considering the three central apertures.

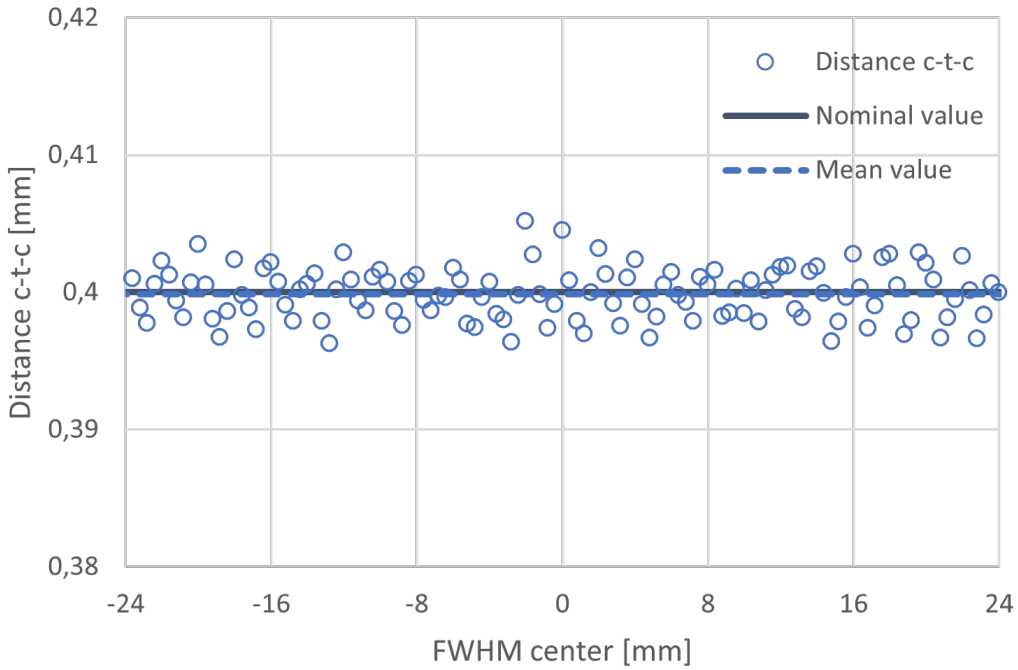

Figure 3.8: Center-to-center distance distribution between the apertures of the Densimet MSC and with the MSC aligned considering the apertures located at motor position -15 mm.

Table 3.1 summarize the average values of the FWHM and of the distance c-t-c for the CF MSC and the Densimet MSC in the case of the beam aligned with the central aperture and with the aperture at -15 mm. The last case is referred to as Densimet *rotated*.

MSC	Average FWHM [μm]	% Std dev (2σ)	Average distance c-t-c [μm]	% Std dev (2σ)
CF	49.78±1.43	2.88	399.87±1.66	0.42
Densimet	48.66±1.78	3.66	399.85±2.24	0.56
Densimet rotated	46.26±2.18	4.72	399.86±1.95	0.49

Table 3.1: Average FWHM and c-t-c distance between the apertures of the CF MSC, the Densimet MSC in the case of the beam aligned with the central aperture and with the aperture at -15 mm (*Densimet rotated*).

3.2. Radiation transmission through the multislit collimator blades

The results of the theoretical and experimental analysis of the transmitted spectra through the blades of the MSCs are described in the following sections.

3.2.1. Theoretical calculation of transmitted radiation

Figure 3.9 shows the transmittance as a function of the photon energy for the CF and the Densimet MSC, compared to the case of an ideal MSC made of pure tungsten. The transmittance in all cases is almost equal to zero at low energy and it starts to increase from 200 keV for the CF MSC. At 300 keV the transmittance is really low, less then 5% in both cases, and then become more and more important until reaching almost 30% and 20% respectively for the CF and the Densimet MSC at an energy of 600 keV.

The transmittance of the Densimet MSC is lower and much closer to that of a MSC made of pure tungsten with respect to the transmittance of the CF MSC.

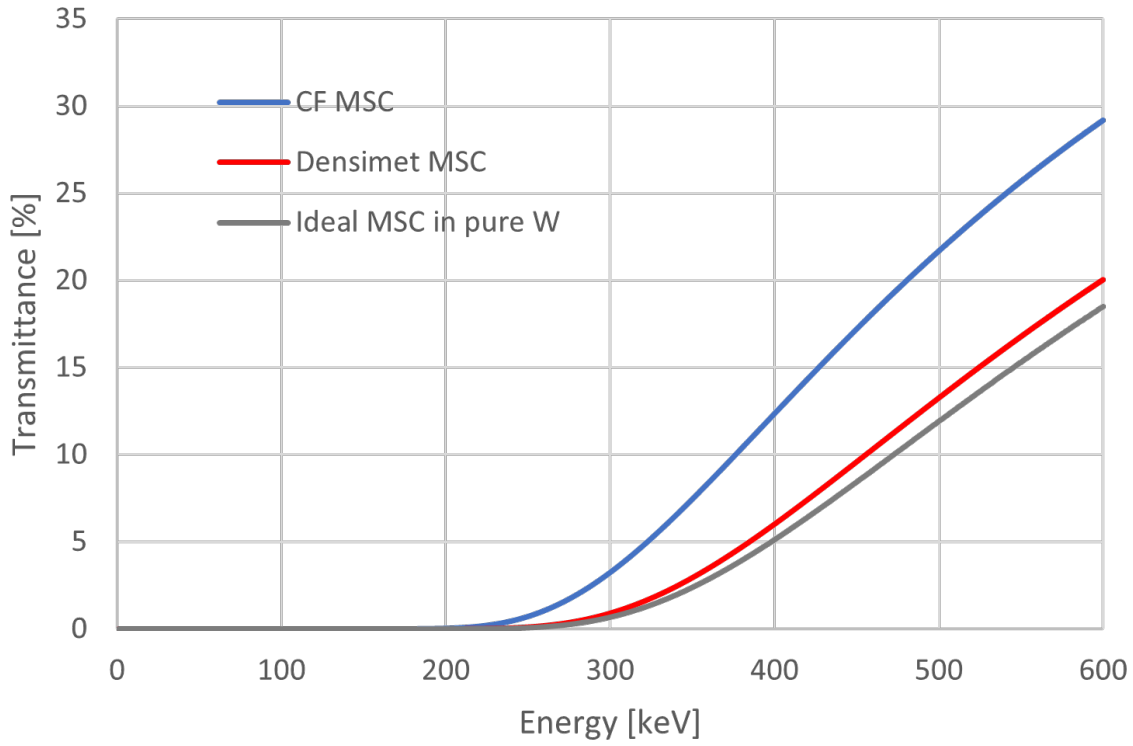

Figure 3.9: Theoretical X-ray transmittance distribution as a function of the photon energy for the CF and the Densimet MSC compared with an ideal MSC made of pure tungsten. Calculation done on the base of the NIST database.

Figure 3.10 shows the expected X-ray transmitted spectra by the CF and the Densimet MSC, obtained by multiplying each normalized spectrum profile, reported in figure 2.4, by the transmittance of the CF and the Densimet MSC, just shown in figure 3.9, in the conventional (on top) and in the clinical (at the bottom) configuration.

As expected, in both configurations, using the Densimet MSC the transmitted radiation decreases with respect to the spectrum transmitted by the CF MSC. The spectrum power reduction is of 70% in both cases.

In both cases the peak of intensity is around 300 keV, shifted towards higher energy with respect to the primary photon beam.

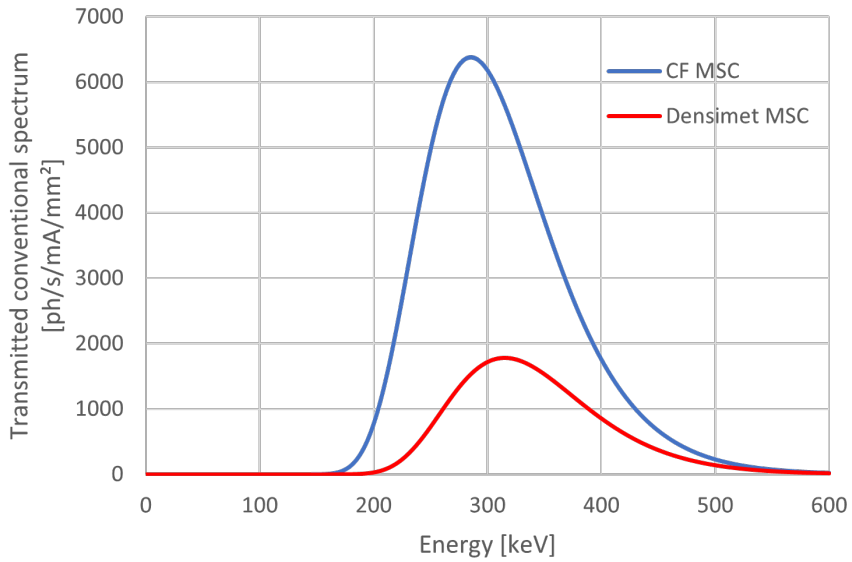

(a)

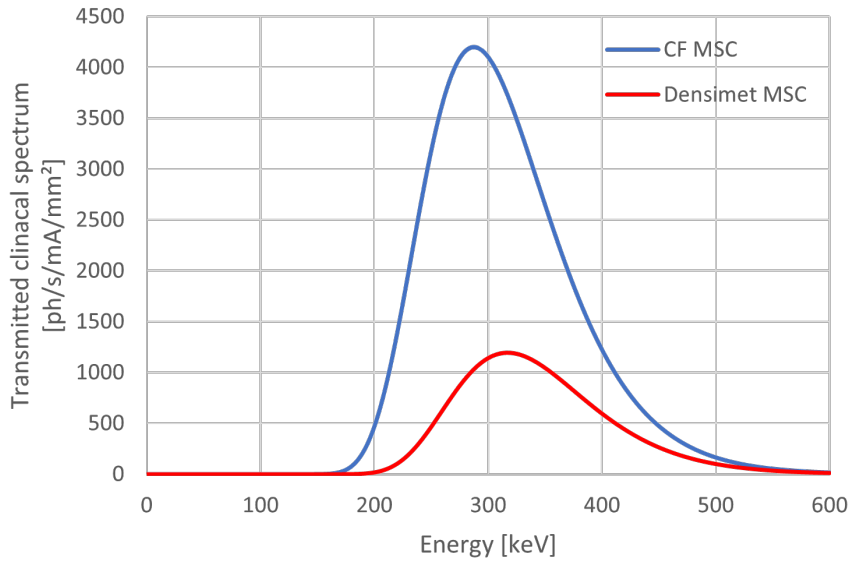

(b)

Figure 3.10: Theoretical X-ray transmitted spectra by the CF MSC (blue curves) and the Densimet MSC (red curves) considering (a) the conventional spectrum and (b) the clinical spectrum.

3.2.2. Monte Carlo simulations of transmitted radiation

After the theoretical calculation of the transmitted spectra by the CF and the Densimet MSC for both clinical and conventional configuration, the Monte Carlo simulations are

performed to confirm the possible agreement between the NIST database and the MC model. A perfect agreement between the calculated and the simulated results can be observed for the spectrum transmitted by either the CF and the Densimet MSC. Figure 3.11 and 3.12 show respectively the transmitted spectra considering the clinical and the conventional configuration.

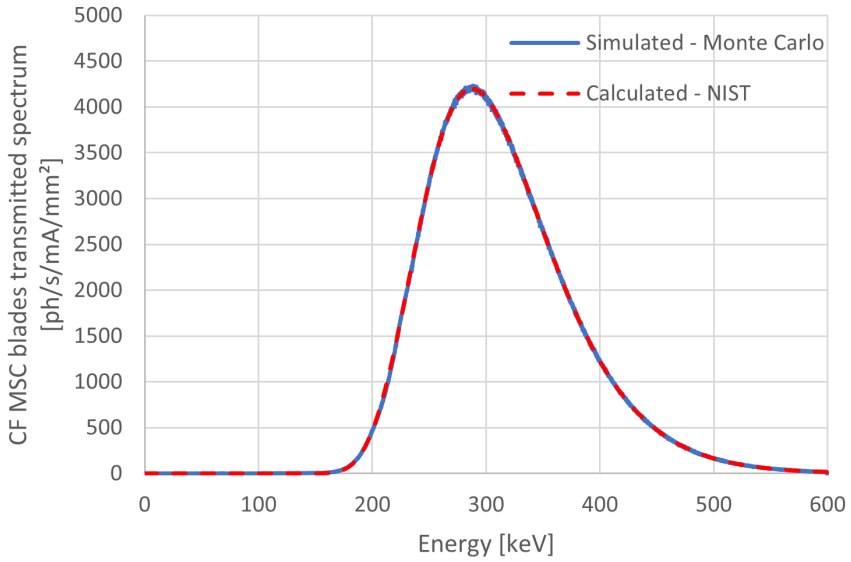

(a)

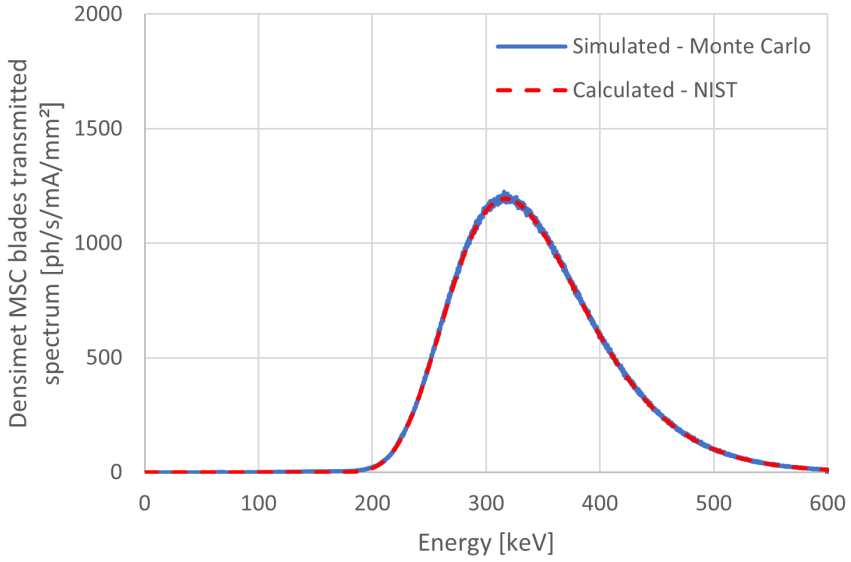

(b)

Figure 3.11: Transmitted clinical spectrum calculated vs simulated, using CF MSC (a) and Densimet MSC (b).

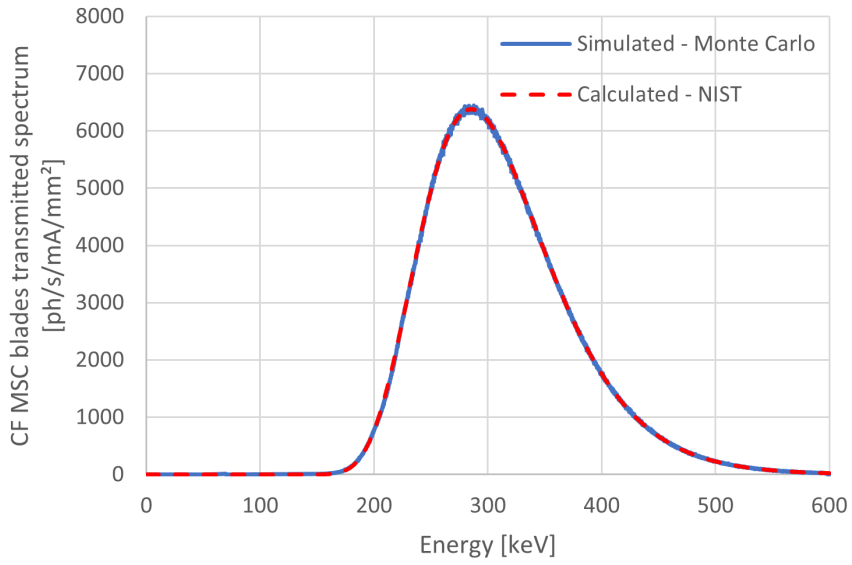

(a)

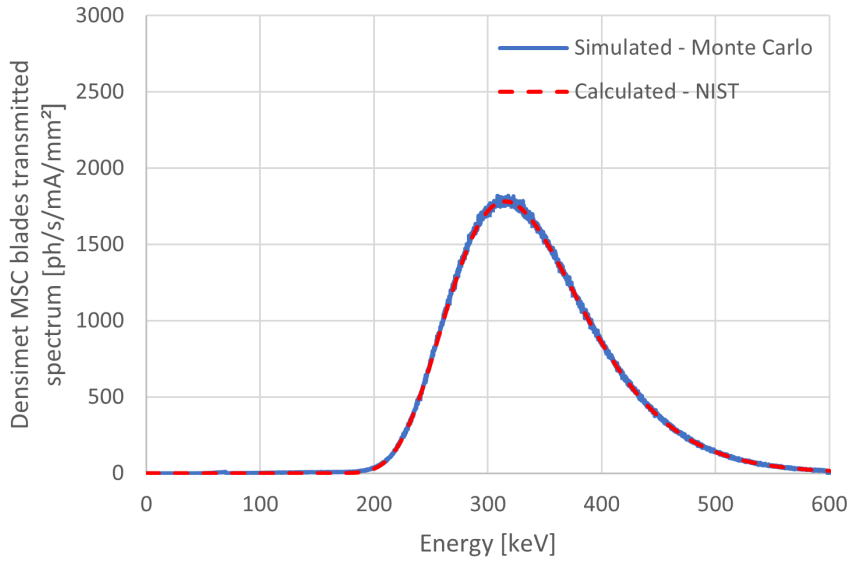

(b)

Figure 3.12: Transmitted conventional spectrum calculated vs simulated, using CF MSC (a) and Densimet MSC (b).

For each of the figures, on top, it is represented the spectrum transmitted by the CF MSC and, at the bottom, the spectrum transmitted by the Densimet MSC.

The plots show perfect agreement between the calculated and the simulated transmitted spectra by either the CF and the Densimet MSC. The simulated spectra have a slightly noisy profile that can be easily improved by simulating more photons and increasing

statistic.

3.3. Dosimetry validation

3.3.1. PTW microdiamond detector measurements

The results of the measurements of the transmitted radiation through the blades considering the CF and the Densimet MSC and using the microDiamond detector, are shown hereafter.

Six different blades from the center of each MSC are considered and three measurements of transmitted dose rate are taken from each blade.

Figure 3.13 shows the valley dose rate normalized with respect to the machine current measured with the CF and the Densimet MSC considering the clinical spectrum.

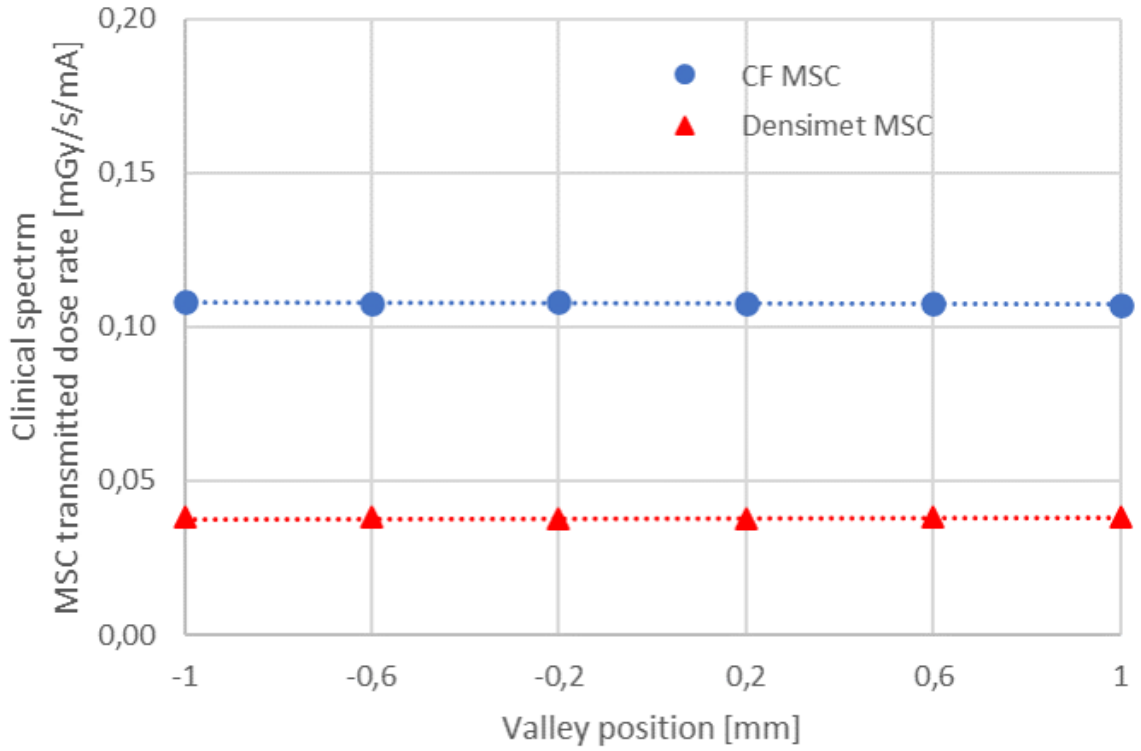

Figure 3.13: Transmitted dose rate normalized by the machine current considering the clinical spectrum and the CF and the Densimet MSC. For each MSC, the six central blades are considered.

For both MSCs it is possible to notice that there is a minimal difference between the dose rate transmitted by different blades. The measured transmitted radiation is around

0.11 mGy/s/mA for the CF MSC and 0.04 mGy/s/mA for the Densimet MSC. In table 3.2, indeed, is reported for each MSC the standard deviation and % standard deviation between the dose rates measured in correspondence of different blades: for both the CF MSC and the Densimet MSC the differences can be considered negligible. This confirm that overall the blades of the two MSC have the same capability in absorbing radiation. Some small variations could be linked to a non-perfect alignment of the blades or some imperfections of the material the two MSCs are made of.

The same trend is found for the conventional spectrum. Figure 3.14 shows the normalized valley dose rate for the CF and the Densimet MSC together with the mean values. Also for the conventional configuration the transmitted dose rate by different blades is almost constant: as shown in table 3.2, it is around 0.17 mGy/s/mA for the CF MSC and 0.06 mGy/s/mA for the Densimet MSC with an error around zero for either CF and Densimet MSC.

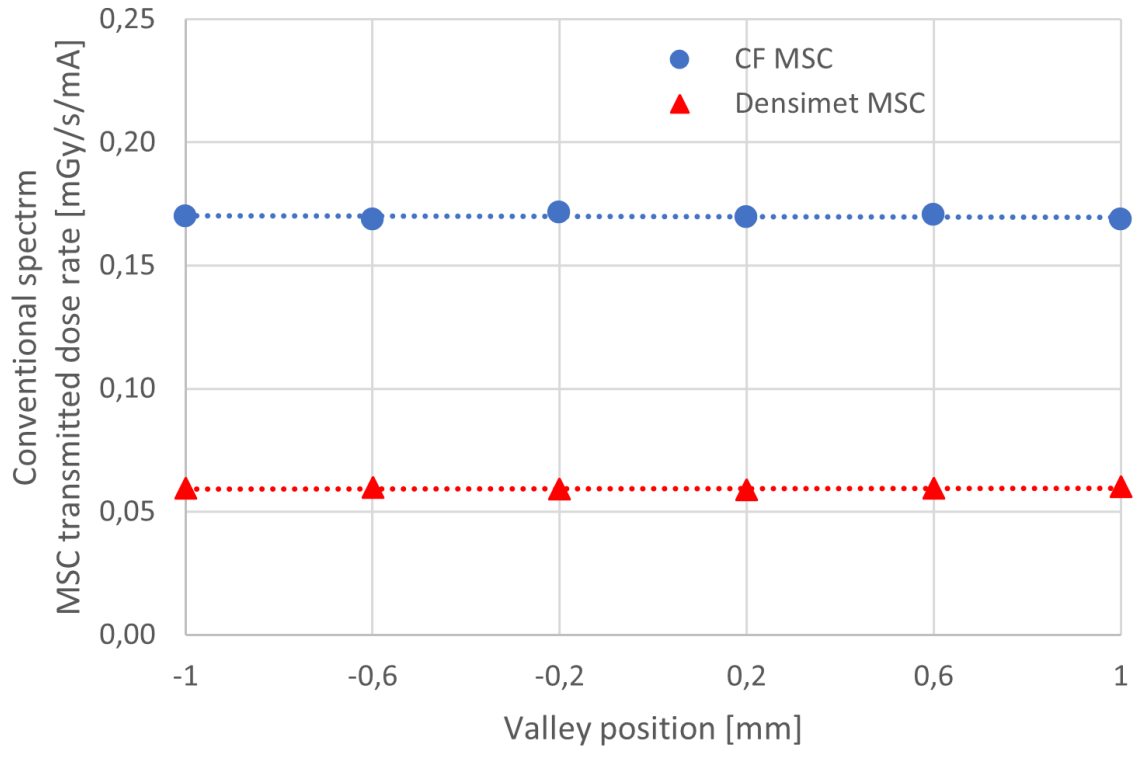

Figure 3.14: Transmitted dose rate normalized by the machine current considering the conventional spectrum and the CF and the Densimet MSC. For each MSC, the six central blades are considered.

	Average transmitted dose rate [mGy/s/mA]			
MSC	**Clinical spectrum**	**% Std dev (2σ)**	**Conv spectrum**	**% Std dev (2σ)**
CF	0.11±0.00	0.32	0.17±0.00	0.59
Densimet	0.04±0.00	0.66	0.06±0.00	0.75

Table 3.2: Average transmitted dose rate measured with the CF and the Densimet MSC for the clinical and the conventional configuration.

The most important result is the % difference of the transmitted dose measured between the two collimators that is 65% less when using the Densimet MSC with respect to the CF MSC. This value is slightly smaller but overall in good agreement with the theoretical value calculated in section 3.2.1.

Following this measurement, the model of the transmitted radiation through the blades of the MSCs can be considered valid for the MC simulations done.

3.3.2. Film measurements in air

The results of the film dosimetry performed in air for both CF and Densimet MSC are reported hereafter. With respect to the microdiamond detector measurements where only one blade per time is irradiated using a small field size, here films are irradiated with an entire microbeam array defined by the collimators. The result is not just the transmitted radiation measured in correspondence of the particular blade considered, but the 2-dimensional map of the delivered dose considering as well the scattered radiation due to the presence of the microbeams. In addition, being the blades irradiated entirely, some possible imperfections of the MSC may bring non-expected variation of the dose delivered to the films due to the radiation interaction with the inner walls of the collimators

Figure 3.15 shows the valley dose profile measured on the radiochromic film using the clinical spectrum and both MSCs. It can be easily observed an overall higher valley dose delivered when using the CF MSC and, in addition, the irregularity of the valley dose profiles.

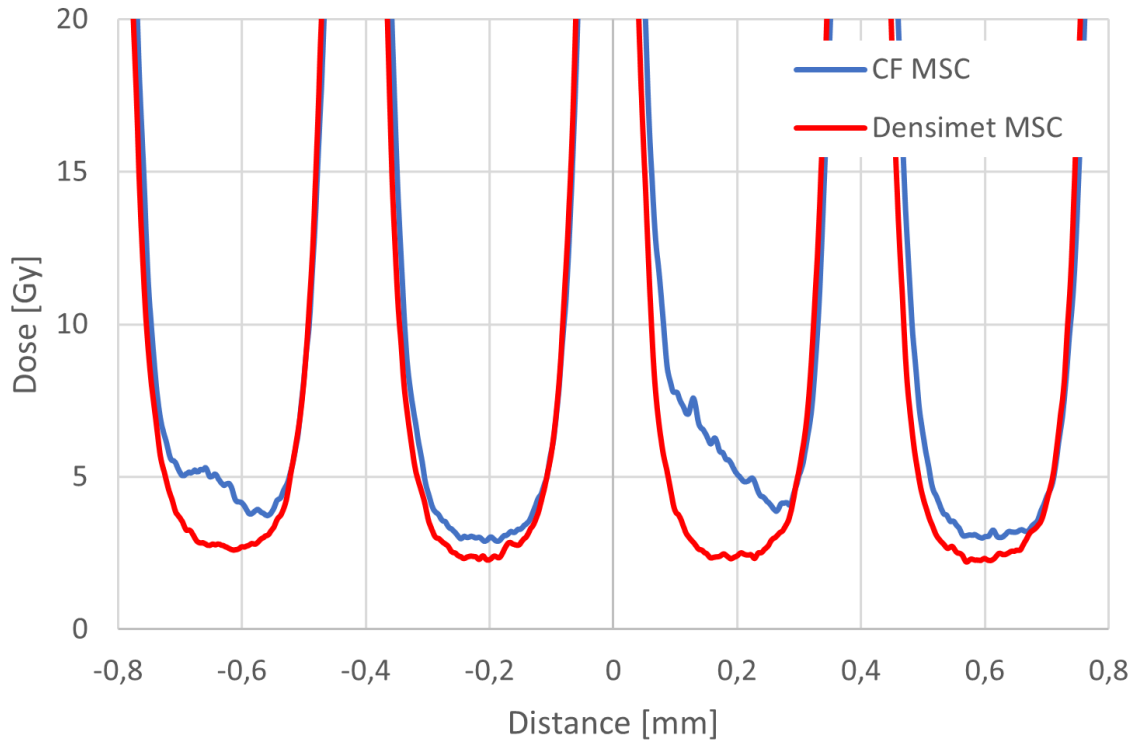

Figure 3.15: Detail of valley dose profile measured with radiochromic films using the CF MSC (blue line) and Densimet MSC (black line).

For the data analysis, a visual classification of the *good* valley profile, with a well-defined rounded shape, and *bad* valley profile, with a somehow distorted dose distribution, is done. For each field size, a separate statistic is done for *good* and *bad* valley in addition to an overall average dose. The total average valley dose is the average among all the twelve valley dose. Table 3.3 and 3.4 reports the results of the valley dose analysis for the clinical spectrum in combination with the use of the CF MSC and Densimet MSC, respectively. The standard deviation and % standard deviation of all the twelve valley dose is reported for each field size.

Comparing the results between different field size for both CF and Densimet MSC, the average valley dose slightly decreases with the decrease of the field dimension. For larger field the contribution related to the scattered radiation inside the target (the RCF in this case) increases, causing the increase of also the valley dose itself. Counting the distorted valleys, they are more numerous when using the CF MSC (up to one third) while they are rarely observed when the Densimet MSC is used. This is reflected in the higher standard deviation calculated between the valley doses produced by the CF MSC.

Analysis done with clinical spectrum and CF MSC

Field size [mm^2]	Good average valley dose [Gy]	Bad average valley dose [Gy]	Total average valley dose [Gy]	% Std dev (2σ)
20x20	3.30±0.04	5.06±0.36	4.18±0.92	21.94
10x10	3.04±0.03	3.05±0.30	2.99±0.89	29.79
5x5	2.98±0.08	2.95±0.32	3.00±0.94	31.39

Table 3.3: Average values of the good, the bad and the total valley dose the four central valleys for each field size, using the clinical spectrum in combination with the CF MSC.

Analysis done with clinical spectrum and Densimet MSC

Field size [mm^2]	Good average valley dose [Gy]	Bad average valley dose [Gy]	Total average valley dose [Gy]	% Std dev (2σ)
20x20	2.68±0.07	3.01±0.02	2.77±0.15	5.55
10x10	2.50±0.06	2.87±0.04	2.59±0.17	6.51
5x5	2.41±0.04	2.72±0.04	2.49±0.14	5.70

Table 3.4: Average values of the good, the bad and the total valley dose the four central valleys for each field size, using the clinical spectrum in combination with the Densimet MSC.

Also, the variation of dose between good and bad valley profile is different between the two collimators. Bad valleys have around 10% more dose for the Densimet MSC, while 35% more for the CF MSC. The distortion of valleys is clearly visible for the CF MSC, while for the Densimet MSC they have a regular rounded profile but higher dose. Moreover, using the CF MSC the variation of dose among different valleys is more relevant with respect to the case in which the Densimet MSC is used.

The comparison between the CF and the Densimet MSC could be done calculating the % difference of the valley dose of the Densimet MSC with respect to that of the CF MSC. Table 3.5 shows the improvements obtained using the Densimet MSC and the clinical spectrum for each field size.

Percentage difference of the Densimet MSC with respect to the CF MSC using the clinical spectrum

Field size $[mm^2]$	Good valley dose [%]	Bad valley dose [%]	Total valley dose [%]
20x20	-18.65	-40.53	-33.84
10x10	-17.96	-40.02	-33.78
5x5	-18.99	-43.27	-35.99

Table 3.5: Percentage difference of the average valley dose obtained with the Densimet MSC with respect to the average valley dose obtained using the CF MSC for the three field dimensions and considering the clinical spectrum.

It is possible to notice that the improvements using the Densimet MSC is much more relevant for the *bad* valleys, rather than for the *good* valleys: in the first case a reduction that goes from the 40% with the $20 \times 20mm^2$ field size to the 43% with a $5 \times 5mm^2$ field size is achieved. When considering only the *good* valleys, instead, the average valley dose is reduced by 18/19% using the Densimet MSC. Nevertheless, a significant reduction occurs. Considering the average valley dose over all valley regions, the reduction using the Densimet MSC is of the 33/35%. This difference is much smaller with respect to what has been calculated theoretically in section 3.2.1. and to what has been measured with the microdiamond detector in section 3.3.1. As already explained, due to the fact that an entire array of microbeam is used, a further contribution to the valley dose is related to the scattered photons inside the film, on top of potential imperfections of the blades MSC alignment. However, a clear difference between the dose delivered by the two different collimators is observed, with the Densimet MSC more capable in defining more reliable microbeam arrays.

The study is repeated as well using the conventional spectrum and the results follow the same trend.

The consideration done for the clinical spectrum are similar for the conventional one. Comparing the variation among different valley doses, from table 3.6 and table 3.7 it is evident that the Densimet MSC gives pretty stable results: the % standard deviation is 6/7% compared with the 26/27% obtained using the CF MSC. Moreover, table 3.8 shows the improvements obtained using the Densimet MSC considering the three field dimensions: even if, as before, the % difference is higher for bad rather than for good valleys, the overall result is a reduction of around the 29% of the valley doses if the

Densimet MSC is used instead of the CF MSC.

Analysis done with conventional spectrum and CF MSC

Field size [mm^2]	Good average valley dose [Gy]	Bad average valley dose [Gy]	Total average valley dose [Gy]	% Std dev (2σ)
20x20	2.76±0.03	4.67±0.35	3.71±0.99	26.56
10x10	2.54±0.05	4.30±0.29	3.42±0.91	26.46
5x5	2.46±0.09	4.25±0.33	3.35±0.93	27.70

Table 3.6: Average values of the good, the bad and the total valley dose the four central valleys for each field size, using the conventional spectrum in combination with the CF MSC.

Analysis done with conventional spectrum and Densimet MSC

Field size [mm^2]	Good average valley dose [Gy]	Bad average valley dose [Gy]	Total average valley dose [Gy]	% Std dev (2σ)
20x20	2.56±0.10	2.87±0.06	2.64±0.16	6.23
10x10	2.45±0.20	2.37±0.03	2.43±0.17	7.11
5x5	2.31±0.08	2.64±0.10	2.39±0.17	7.04

Table 3.7: Average values of the good, the bad and the total valley dose the four central valleys for each field size, using the conventional spectrum in combination with the Densimet MSC.

Percentage difference of the Densimet MSC with respect to the CF MSC using the conventional spectrum

Field size [mm^2]	Good valley dose [%]	Bad valley dose [%]	Total valley dose [%]
20x20	-7.25	-38.54	-29.00
10x10	-3.56	-44.89	-28.97
5x5	-5.98	-37.82	-28.63

Table 3.8: Percentage difference of the average valley dose obtained with the Densimet MSC with respect to the average valley dose obtained using the CF MSC for the three field dimensions and considering the conventional spectrum.

Overall the Densimet MSC is actually improving the reliability of the radiation delivered to the target surface and it should be preferred to the CF MSC for future MRT experiments.

3.3.3. Dosimetry validation in phantom

Film dosimetry is performed inside a water-equivalent plastic phantom to measure the difference in dose delivery by an array of microbeams defined by the two different MSCs. In this case, for time reason, only the most interesting configuration of the clinical spectrum is considered. The field sizes used are 20×20 mm^2, 10×10 mm^2 and 5×5 mm^2 and the depth considered for the film are 3 mm, 5 mm, 10 mm and 20 mm from the surface of the water cube.

The results report the average valley dose, calculated as the average among the eight valley dose measured for each depth in the center of the field, together with the standard deviation and percentage standard deviation between the measured valley doses.

Table 3.9 shows the case of 20×20 mm^2 field using the CF and the Densimet MSC. In both cases the average valley dose increases with increase of the depth, in the first 20-25 mm of the phantom, due to the scattered radiation contribution inside the material of the cube. The dose difference between bad and good valleys is decreased with respect to the case observed of films irradiated in air. The difference between good and distorted valley doses is mitigated by the more dominant contribution of the scattered radiation inside the target. It must be also considered that films in air and films inside the phantom were irradiated in different experimental session, and a slightly different alignment of the MSC may have changed the result of the radiation interaction with the inner walls of the MSC.

Analysis of the valley dose done using the CF MSC and the Densimet MSC with a 20×20 mm^2 field size

Depth	Average valley dose [Gy]			
[mm]	CF MSC		Densimet MSC	
		% std dev (2 σ)		% std dev (2 σ)
3	2.15±0.07	3.25	1.87±0.05	2.66
5	2.39±0.04	1.49	2.16±0.06	2.57
10	2.63±0.05	1.74	2.39±0.03	1.43
20	2.76±0.05	1.78	2.51±0.08	3.31

Table 3.9: Average values of the valley dose at different depth from the water equivalent phantom surface, together with the standard deviation and % standard deviation between the eight valley dose measured for each depth, considering a 20×20 mm^2 field using the CF MSC and the Densimet MSC.

Extending the same approach to the 10×10 mm^2 and to the 5×5 mm^2 field cases, results are presented respectively in table 3.10 and 3.11. The same consideration made for the 20×20 mm^2 field size can be repeated here in both cases.

Analysis of the valley dose done using the CF MSC and the Densimet MSC with a 10×10 mm^2 field size

Depth	Average valley dose [Gy]			
[mm]	CF MSC		Densimet MSC	
		% std dev (2 σ)		% std dev (2 σ)
3	2.21±0.04	1.77	1.94±0.03	1.75
5	2.48±0.06	2.35	2.11±0.04	2.03
10	2.59±0.09	3.45	2.29±0.07	3.02
20	2.52±0.03	1.08	2.17±0.08	3.77

Table 3.10: Average values of the valley dose at different depth from the water equivalent phantom surface, together with the standard deviation and % standard deviation between the eight valley dose measured for each depth, considering a 10×10 mm^2 field using the CF MSC and the Densimet MSC.

Analysis of the valley dose done using the CF MSC and the Densimet MSC with a 5×5 mm^2 field size

Depth	Average valley dose [Gy]			
[mm]	CF MSC		Densimet MSC	
		% std dev (2 σ)		% std dev (2 σ)
3	2.11±0.04	1.84	1.79±0.06	3.20
5	2.23±0.07	2.92	1.90±0.07	3.73
10	2.32±0.06	2.47	1.93±0.07	3.61
20	2.05±0.04	1.93	1.80±0.06	3.23

Table 3.11: Average values of the valley dose at different depth from the water equivalent phantom surface, together with the standard deviation and % standard deviation between the eight valley dose measured for each depth, considering a 5×5 mm^2 field using the CF MSC and the Densimet MSC.

The MC simulations results confirm the difference in the valley dose delivered with one and the other MSC. Figure 3.16 shows the depth dose profile of the valley dose for a 20×20 mm^2 array of microbeams simulated using the clinical spectrum and both CF and Densimet collimators. In the first 20 mm form the phantom surface the valley dose increases due to the increased radiation scattering contribution inside the valley regions, while going deeper inside the phantom, the absorption of the primary photons becomes more relevant, causing the overall decrease of the valley dose. The % difference between the two profiles reported at the bottom of figures 3.16 shows a high difference at the entrance of the phantom where the radiation scattering contribution is minimum and the contribution of the different transmitted radiation between the two collimators is dominant. The percentage difference stays between -4% and -6% inside the phantom.

Similar trends are obtained with the 10×10 mm^2 field size and the 5×5 mm^2 field size but for these smaller fields there is an increased percentage difference in the valley dose deposition between the two collimators. For the 10×10 mm^2 field size, the differences are up to -12% at the phantom surface and between -8% and -10% inside the cubic phantom. For the 5×5 mm^2 field size, the differences are up to -18% at the phantom surface and between -13% and -16% inside the cubic phantom. Figures 3.17 and 3.18 show the depth dose profiles of the valley dose for the 10×10 mm^2 and the 5×5 mm^2 field size, respectively, when the two MSCs are used.

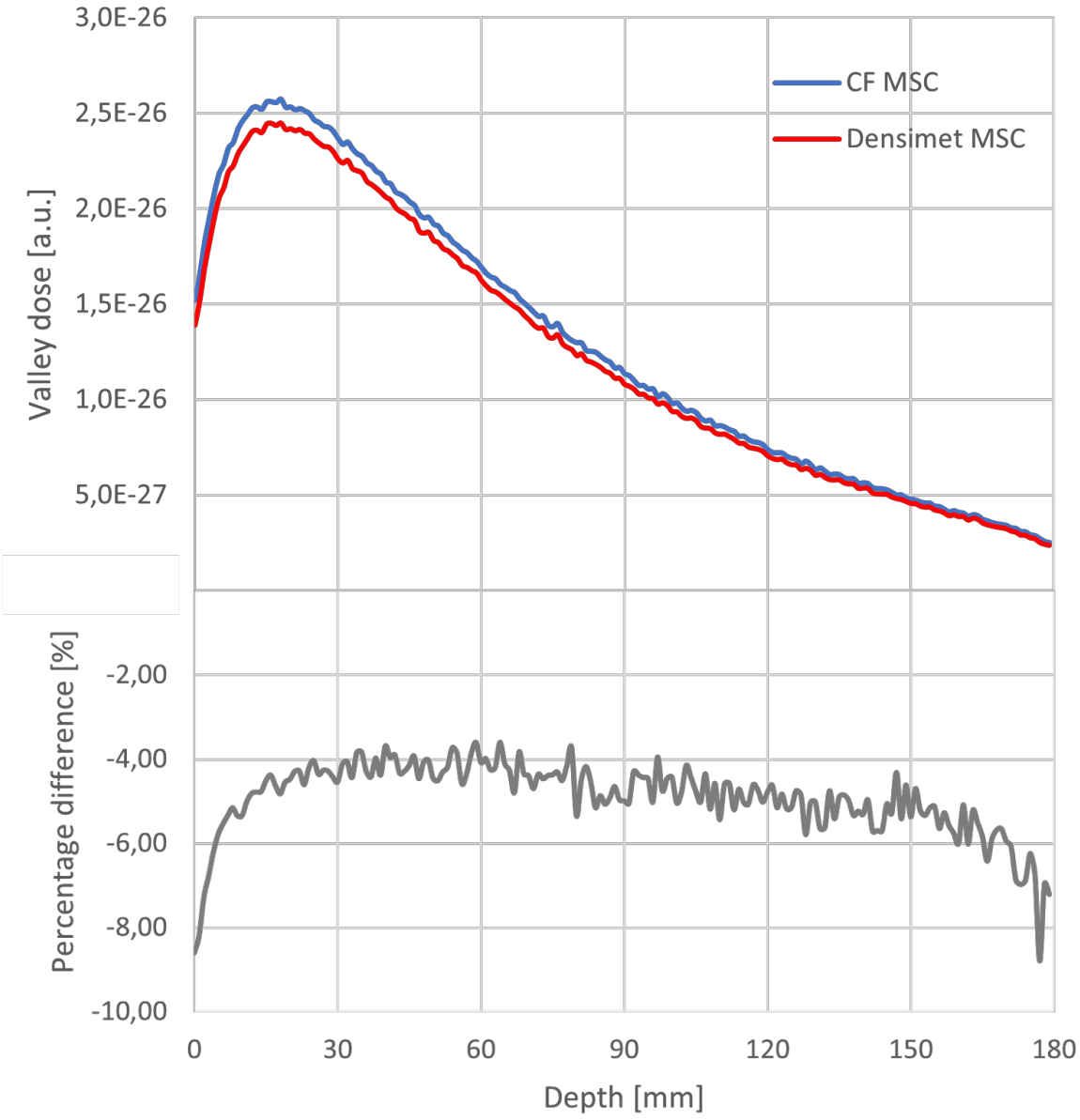

Figure 3.16: On top valley depth dose profile obtained with CF MSC and Densimet MSC and with a 20×20 mm^2 field size. At the bottom percentage difference of the valley dose obtained with the Densimet MSC with respect to that obtained with the CF MSC at different depth inside the phantom.

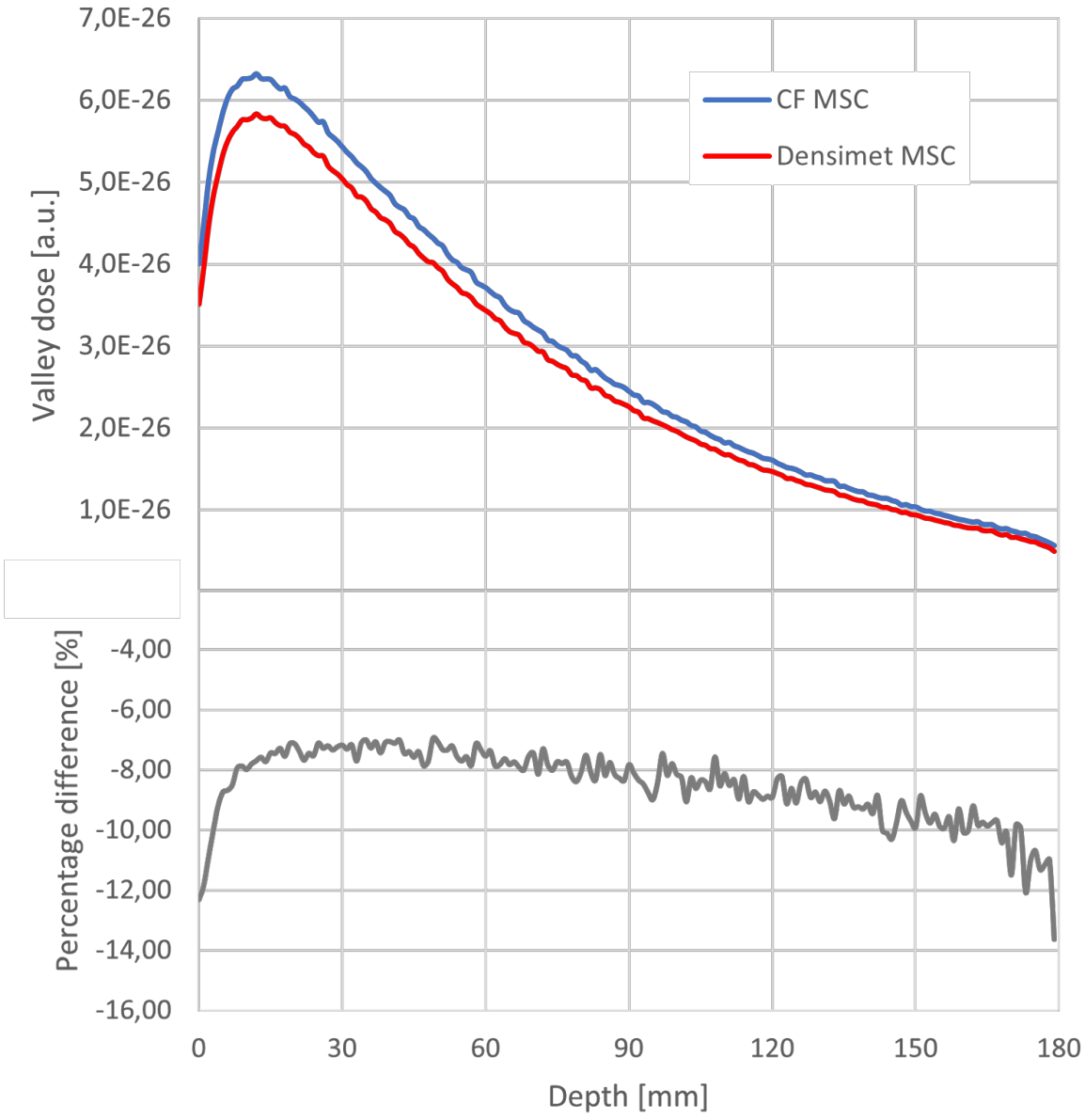

Figure 3.17: On top valley depth dose profile obtained with CF MSC and Densimet MSC and with a 10×10 mm^2 field size. At the bottom percentage difference of the valley dose obtained with the Densimet MSC with respect to that obtained with the CF MSC at different depth inside the phantom.

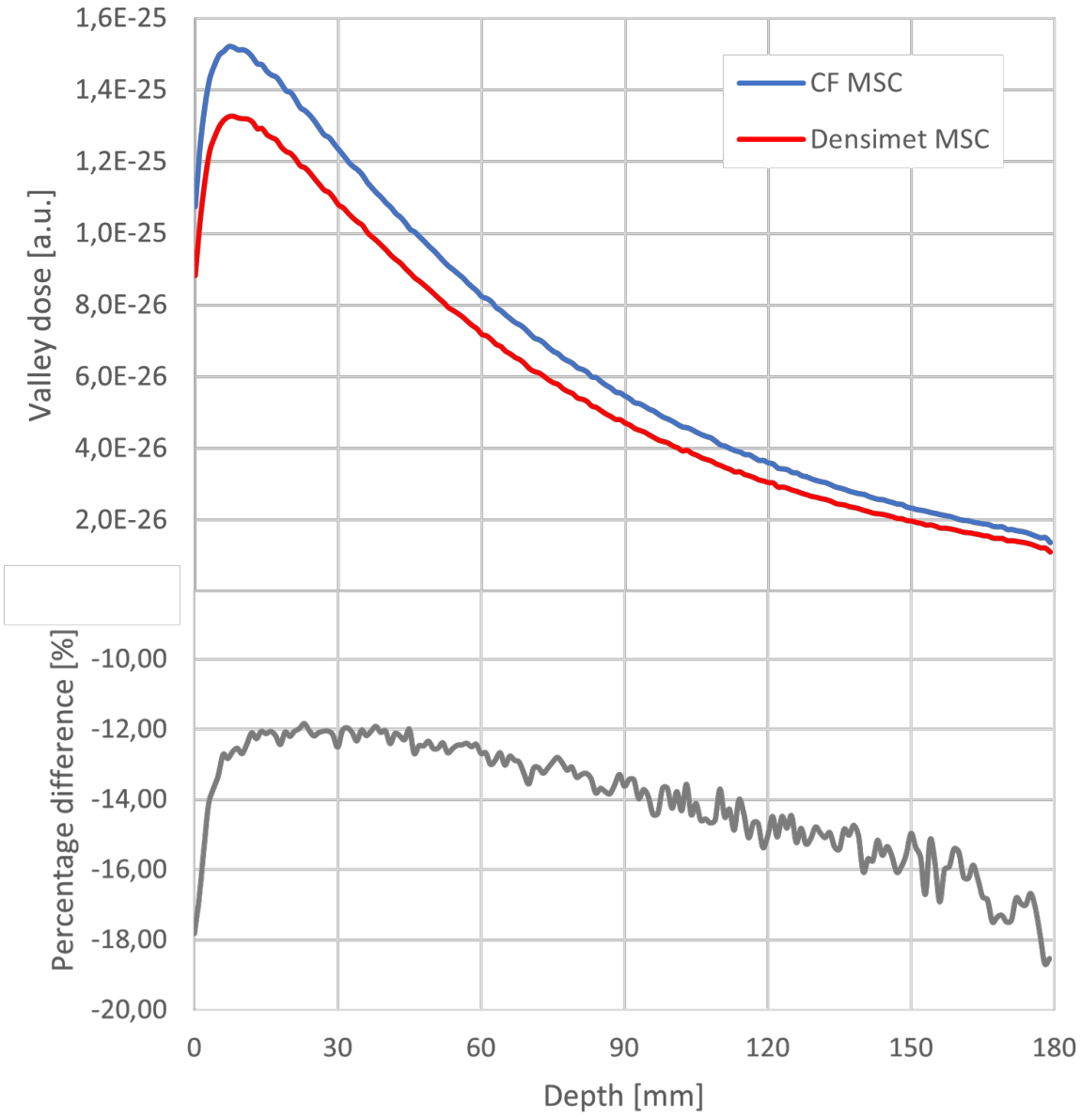

Figure 3.18: On top valley depth dose profile obtained with CF MSC and Densimet MSC and with a 5×5 mm^2 field size. At the bottom percentage difference of the valley dose obtained with the Densimet MSC with respect to that obtained with the CF MSC at different depth inside the phantom.

Interesting is the comparison of the valley dose data obtained from film dosimetry and MC simulation when the two collimators are used. The results are shown in table 3.12 where the percentage difference is reported for each depth and each field size, compared with MC simulations.

Percentage difference of the Densimet MSC with respect to the CF MSC.

Depth [mm]	20×20 mm^2 **field [%]**		10×10 mm^2 **field [%]**		5×5 mm^2 **field [%]**	
	Film	**MC**	**Film**	**MC**	**Film**	**MC**
3	-12.83	-6.78	-11.97	-10.03	-15.27	-14.12
5	-9.49	-5.79	-14.86	-8.74	-14.77	-13.32
10	-9.25	-5.34	-11.43	-7.98	-16.58	-12.70
20	-9.21	-4.48	-13.73	-7.12	-12.26	-12.20
Average % diff	-10.20	-5.60	-12.99	-8.47	-14.72	-13.09

Table 3.12: Percentage difference of the valley dose obtained with the Densimet MSC with respect to the CF MSC for the three field dimensions using the clinical spectrum. Four depths were considered from the surface of the water cube. Data compare film dosimetry with MC simulations.

The overall reduction of valley dose using the Densimet MSC is clearly visible.

For both film dosimetry and MC simulation differences between the valley dose for the depth inside the phantom considered is small and therefore at 3 mm depth we can consider the radiation scattering contribution relevant. Comparing dose differences between different field size, the average % difference of the Densimet MSC with respect to the CF MSC increases for small field size: it goes from around -10% with a 20×20 mm^2 field to around -15% with a 5×5 mm^2 field. Same trend is obtained with MC simulations: the % difference goes from -5% with a 20×20 mm^2 field to around -13% with a 5×5 mm^2 field. Bigger it is the field, stronger is the contribution of the scattering events happening inside the target making overall less important the contribution of the transmitted radiation interacting with the MSCs and reaching the sample, due to radiation transmission or interaction with the MSC inner walls.

To conclude, a difference between the two MSCs is present, thus it is possible to definitely confirm that the Densimet MSC is able of absorbing more radiation through the blades, decreasing the resulting valley dose seen on the irradiated films, with respect to the CF MSC.

4 | Discussion

The aim of this work is to better understand and characterize the radiation-matter interaction that occur in microbeam radiation therapy when the homogeneous X-ray beam interact with the multislit collimator and improve the reliability in the definition of an array of microbeams. Previous studies showed that a non-negligible transmitted radiation through the blades of the MSC, available at the ID17 biomedical beamline of the ESRF and made of CF-H25S+ material, influences the dose delivered in the valley region of a microbeam array. From this the need of realizing a new MSC, made of Densimet 185 material, capable of better absorbing the radiation transmitted through its blades, reducing the scattering of the radiation on the collimator inner walls and therefore decreasing the valley dose, arises. After the characterization of the two MSCs geometry, the comparison between measured and simulated transmitted spectra are performed, followed by a dosimetry study in three different ways: a PTW microdiamond detector is used for the measurement of the transmitted radiation through the collimators blades, radiochromic film dosimetry in air is used to measure the radiation delivered by an array of microbeams at the surface of the target and film dosimetry is as well performed in an water equivalent phantom to quantify the valley dose variation in a more realistic irradiation scenario.

The first part focuses on the characterization of the MSCs geometry, aperture width and center-to-center spacing, and it is realized by scanning the MSCs in front of a narrow synchrotron beam. For both MSCs the overall results about the apertures geometry are in good agreement with nominal values, with small errors that could be caused by measurements limits such as the minimum motor step of 5 μm. This limit on the motor displacement requires an interpolation of the value acquired on the aperture edges that can cause an error on the FWHM measured of around 1/2 μm.

Despite the measurement limits, the misalignment of the blades orientation is clearly observed for both the CF and the Densimet MSC and a different amount of radiation can pass through each single apertures depending on its alignment with respect to the beam. In MC simulations, the MSC is built with an ideal structure: the 125 blades are considered perfectly aligned inside a no divergent beam, thus creating exactly an array

of 50 μm wide microbeams and 400 μm pitch. It would be useful to simulate arrays of microbeams with a slightly different beam width, with respect to the nominal one, in order to estimate the difference in the delivered dose for microbeams which are slightly larger or narrower.

It is possible to distinguish two cases of scattering events: scattering events that can happen during the MSC-radiation interaction and the scattering events that occurs in the target.

When the X-ray beam interacts with the MSC, several scattering events can happen. Considering the photons impinging on the central part of the MSC blades, MC simulations suggest that photons have just two main possibilities: they will pass undisturbed through the entire blade being transmitted or they will be completely absorbed inside the blade. The contribution of photons that undergo a scattering event in the bulk of a MSC blade and escape the blade is negligible. The agreement between theoretical calculation using NIST's data and simulated transmitted spectra is indeed excellent.

The theoretical percentage difference between the radiation transmitted by the CF MSC and the Densimet MSC, calculated using NIST's database and confirmed by MC simulations, is 70%. Measuring only the transmitted radiation through the blade of the MSCs by means of a PTW microdiamond detector, as shown in section 3.3.1., the percentage difference between the results obtained with the CF MSC and the Densimet MSC is 65%, in agreement with the theoretical value.

The second radiation-MSC interaction that requires particular attention is related to photons hitting the inner walls of the collimator. The synchrotron beam has anyway a natural divergence, despite it is really small, and moreover the blades of both MSCs are not perfectly aligned. From film dosimetry in air, the presence of distorted valleys suggests that radiation reflection on the MSC walls may occur. This phenomenon cannot be simulated with MC approach that consider photons as particles and a software able to considered the wave nature of the photons should be used. The use of the Densimet MSC clearly improves the delivery of valley doses with a more regular rounded shape. The fact that the Densimet 185 material is more rich in Tungsten may have improved the results reducing the probability of photon reflection. Film irradiated in air shows that the percentage difference between the valley dose measured when the Densimet MSC is used with respect to that measured with the CF MSC is of 30%. With respect to the measurement of only the transmitted radiation through the MSC blades, here the entire array of microbeam is irradiated. In addition, slightly divergent photons may encounter along their path not the entire 8 mm thick blade, but just a portion of material close to

the blade corner, also favored by the not perfect blades alignment. All this radiation could scatter and be deviated into the valley region increasing the delivered dose, in addition to the transmitted radiation contribution. In future, to possibly quantify this contribution, MC simulations including the MSC blades misalignment are planned.

Entering the target, photons undergo different scattering events that brings dose delivery into the valley regions, between microbeams. The intensity of the valley dose due to scattering events inside the target varies depending on the field size, the target material and the target dimensions. Smaller field will result in a reduced scattering contribution into the valley, while bigger target volume will increase the probability of having a scattering event and therefore an increased valley dose. In our case, with the use of a 180x180x180 mm^3 water-equivalent phantom, the scattering contribution of the radiation inside the target is the most dominant in the valley dose.

Indeed, films dosimetry inside the phantom at different depth and with different field size shows a smaller difference with respect to film dosimetry in air when the two MSC are used. The valley dose % difference when using the Densimet MSC is on average -10% for a 20×20 field, -13% for a 10×10 mm^2 field and -15% for a 5×5 field. In addition, the % difference of the simulated valley dose is smaller than the % difference of the measured valley dose. This difference between measured and simulated can be explained by the fact that the MC model of the MSC is too approximate and do not consider all non-idealities of the MSC inner walls and their interaction with radiation.

Overall, the results can be considered very satisfactory because the use of the Densimet MSC improves the reliability of the microbeams delivery in MRT. The MSC remains a very critical component for this radiotherapy technique and still the limits in the realization of this components leave the room for further improvements and developments.

5 | Conclusion

The development of MRT opens new prospective in the research for cancer defeating with the spatial fractionation of the irradiation field at micrometric scale. When X-ray radiation sources are used for spatial fractionated radiotherapy approaches, the use of a MSC is necessary and a full understanding and characterization of the interaction of the radiation with this component is essential to control in a reliable way the irradiation process. The aim of this study is to characterized the performance of a new MSC recently purchased at the ESRF - ID17 biomedical beamline, and to compare it with the MSC already used. After the verification of the geometry of the new MSC, made of Densimet 185 material, to understand if the MSC is more effective in absorbing the radiation of the incoming synchrotron beam, the transmitted radiation trough the blades of the MSC is measured. Experimental dosimetry study is realized for measuring the dose delivered at the target by different arrays of microbeams, with focus on the valley dose delivered between microbeams. Experimental data are compared to MC simulations.

The experimental measurements are successful in confirming the improvement for the realization of microbeams using the Densimet MSC with respect to the CF MSC. The radiation transmitted through the MSC blades measured with the PTW microdiamond detector is reduced by -65% when using the Densimet MSC, in close agreement with the theoretical value of -70% calculated using NIST's data or MC simulations. The delivered valley dose to the target surface is measured by radiochromic films irradiated in air and a reduction of -30% valley dose is observed when using the new MSC. When valley doses are measured inside a water-equivalent phantom, -10% valley dose for a $20 \times 20\ mm^2$ field and -15% for a $5 \times 5\ mm^2$ is observed when using the new MSC. Comparing the depth dose profiles calculated with MC simulations, the % difference between doses delivered by the two MSCs is slightly smaller than the measured one. This is probably due to the MSC model used for simulation that is too approximate and ideal, and does not consider scattering events that could happen to photons when interacting with the non-ideal inner walls of the MSC.

The introduction of the new Densimet MSC can be considered a significant improvement

for MRT experiments at the ID17 beamline as it is able to better absorb the radiation impinging on the MSC blades and to overall deliver more clean microbeams. This results in a reduction of the valley dose and therefore in a better preservation of healthy tissues for irradiation of biological tissues. Nevertheless, some differences between measured and calculated dose values are observed and are still under investigation. As an example, MC simulations should include the non-idealities found in the geometry of the MSC with all the possible scattering events photons can undergo due to these imperfections.

Overall, this work presents a solid approach for the characterization of MSCs used for spatially fractionated radiotherapy techniques and the realization of a new MSC based on Densimet 185 material improved the reliability in MRT irradiation. This is a step forward in the process of making MRT a well-established and controlled technique for possible future clinical trials.

Bibliography

[1] International agency for research on cancer, . URL https://www.iarc.who.int.

[2] Radiation therapy, . URL https://en.wikipedia.org/wiki/Radiation_therapy.

[3] Pinpoint 3d ion chamber, . URL https://www.ptwdosimetry.com/en/products/pinpoint-3d-ion-chamber/.

[4] National cancer institute, . URL https://www.cancer.gov/about-cancer/treatment/types/radiation-therapy.

[5] How does the esrf work?, . URL https://www.esrf.fr/home/education/what-is-the-esrf/how-does-the-esrf-work.html.

[6] Lightsources.org, . URL https://lightsources.org/.

[7] History of radiography, . URL https://www.nde-ed.org.

[8] A.L.Brambilla. Lecture notes of physics of low-dimensional systems ii – experimental methods. 2021.

[9] S. Bartzsch, S. Corde, J. C. Crosbie, L. Day, M. Donzelli, M. Krisch, M. Lerch, P. Pellicioli, L. M. Smyth, and M. Tehei. Technical advances in x-ray microbeam radiation therapy. *Physics in Medicine and Biology*, 65, 2020.

[10] Blattmann, H., and et al. Applications of synchrotron x-rays to radiotherapy. *Nuclear Instruments and Methods in Physics Research A*, 548, 2005.

[11] BouchetA and al. Permeability of brain tumor vessels induced by uniform or spatially microfractionated synchrotron radiation therapies. *Int. J. Radiat. Oncol. Biol. Phys.*, 98, 2017.

[12] BouchetA, E. Bräuer-Krisch, PrezadoY, M. E. Atifi, L.Rogalev, L. Clec'hC, J. Laissue, L. Pelletier, and G. L. Duc. Better efficacy of synchrotron spatially microfractionated radiation therapy than uniform radiation therapy on glioma. *Int. J. Radiat. Oncol. Biol. Phys*, 95, 2016.

[13] O. J. Brace1, S. F. Alhujaili, J. R. Paino, D. J. Butler, D. Wilkinson, B. M. Oborn, A. B. Rosenfeld, M. L. F. Lerch, M. Petasecca, and J. A. Davis. Evaluation of the ptw microdiamond in edge-on orientation for dosimetry in small fields. *Radiation measurements*, 2019.

[14] M. Donzelli. *Improving dose calculation and treatment planning techniques for microbeam radiation therapy with computational methods*. PhD thesis, Institute of Cancer Research, Sutton, UK, 2018.

[15] E.Bräuer-Krisch, H. Requardt, T. Brochard, G. Berruyer, M. Renier, J. A. Laissue, and A. Bravin. New technology enable high precision multislit collimators for microbeam radiation therapy. *Review of scientific instruments*, 80, 2009.

[16] E. Fardone, B. Pouyatos, E. Bräuer-Krisch, S. Bartzsch, H. Mathieu, H. Requardt, D. Bucci, G. Barbone, P. Coan, G. Battaglia, G. L. Duc, A. Bravin, and P. Romanelli. Synchrotron-generated microbeams induce hippocampal transections in rats. *Scientific reports*, 2018.

[17] C. Fiandra, U. Ricardi, R. Ragona, S. Anglesio, F. R. Giglioli, E. Calamia, and F. Lucio. Clinical use of ebt model gafchromic film in radiotherapy. *The International Journal of Medical Physics Research and Practice*, 2006.

[18] P. Fournier. *Dosimetry in synchrotron microbeam radiation therapy*. PhD thesis, Univeristy of Wollongong, 2016.

[19] C. Huet, C. Moignier, J. Fontaine, and I. Clairand. Characterization of the gafchromic ebt3 films for dose distribution measurements in stereotactic radiotherapy. *Radiant measurements*, 2014.

[20] K.Wille. Introduction to insertion devices. *University of Dortmund, Germany*.

[21] A. Köhler, J. A. Laissue, H. Blattmann, and D. N. Slatkin. Inventor of grid therapy. *Med. Phys.*, 22, 1874-1947.

[22] J. Laissue, G. Geiser, P. Spanne, F. Dilmanian, J. Gebbers, M. Geiser, and et al. Neuropathology of ablation of rat gliosarcomas and contiguous brain tissues using a microplanar beam of synchrotron-wiggler-generated x rays. *Int J Cancer*, 78, 1998.

[23] J. Laissue, H. Blattmann, M. D. Michiel, D. Slatkin, N. Lyubimova, and R. G. et al. The weanling piglet cerebellum: a surrogate for tolerance to mrt (microbeam radiation therapy) in pediatric neuro-oncology. *Penetrating Radiation Systems and Applications III*, 4508, 2001.

[24] D. Lewis, A. Micke, X. Yu, and M. F. Chan. An efficient protocol for radiochromic film dosimetry combining calibration and measurement in a single scan. *The International Journal of Medical Physics Research and Practice*, 2012.

[25] I. D. Manici. Synchrotron x-ray spectra characterization for radiation therapy applications at the esrf - id17 biomedical beamline. Master's thesis, Politecnico di Milano, 2021.

[26] G. Margaritondo. A primer in synchrotron radiation: Everything you wanted to know about sex (synchrotron emission of x-rays) but were afraid to ask. *J. Synchrotron Rad.*, 2, 1995.

[27] M. Morri. Experimental dosimetry of high dose rate x-ray microbeams fields for the mrt program. Master's thesis, Università degli studi di Trieste, 2010.

[28] P. Pellicioli. *Development of radiochromic film dosimetry at micrometric scale for microbeam radiation therapy.* PhD thesis, Communauté Université Grenoble Alpes and Swansea University, 2019.

[29] P. Pellicioli, S. Bartzsch, M. Donzelli, M. Krisch, and E. Bräuer-Krisch. High resolution radiochromic film dosimetry: Comparison of a microdensitometer and an optical microscope. *European Jurnal of Medical Physics*, 2019.

[30] P. Pellicioli, M. Donzelli, J. A. Davis, F. Esteve, R. Hugtenburg, S. Guatelli, M. Petasecca, M. L. F. Lerch, E. Brauer-Krisch, and M. Krisch. Study of the x-ray radiation interaction with a multislit collimator for the creation of microbeams in radiation therapy. *Jurnal of Synchrotron Radiation*, 2020.

[31] Y. Prezado, I. Martínez-Rovira, S. Thengumpallil, and P. Deman. Dosimetry protocol for the preclinical trials in white-beam minibeam radiation therapy. *The International Journal of Medical Physics Research and Practice*, 2019.

[32] D. Slatkin, P. Spanne, F. Dilmanian, and Sandbora. Microbeam radiation therapy. *Med. Phys.*, 19, 1992.

[33] D. N. Slatkin, F. A. Dilmanian, M. M. Nawrocky, and P. Spanne. Design of a multislit, variable width collimator for microplanar beam radiotherapy. *Review of Scientific Instruments*, 1995.

[34] M. Williams, P. Metcalfe, A. Rosenfeld, T. Kron, F. d'Errico, and M. Moscovitch. Radiochromic film dosimetry and its applications in radiotherapy. *AIP Conference Proceedings*, 2011.

[35] W. Zeman, H. J. Curtis, , and C. P. Baker. Histopathologic effect of high-energy-particle microbeams on the visual cortex of the mouse brain. *Radiation Research*, 14, 1961.

List of Figures

List of Tables

List of Abbreviations

Acronym	Complete name
RT	Radiation Therapy
MRT	Microbeam Radiation Therapy
ESRF	European Synchrotron Radiation Facility
MSC	Multislit Collimator
CF	Corrosion Free
TCP	Tumor Control Probability
NTCP	Normal Tissue Complications Probability
PVDR	Peak to Valley Dose Ratio
MSC	Multislit Collimator
CF	Corrosion-Free
BM	Bending Magnet
ID	Insertion Device
UHV	Ultra High Vacuum
RF	Radiation Frequency
SR	Synchrotron Radiation
IC	Ionization Chamber
FReLoN	Fast-Readout Low-Noise
IAEA	International Atomic Energy Agency
MC	Monte Carlo
FWHM	Full Width at Half Maximum
NIST	National Institute of Standards and Technology
Geant4	Geometry and Tracking
OASYS	OrAnge SYnchrotron Suite
OD	Optical Density
RCF	Radiochromic Film

Acknowledgements

I would like to express all my gratitude to my supervisor Dr. Paolo Pellicioli for the precious help during my internship at the ESRF in developing the project and for sharing with me all his knowledge, passion and experience in the field of MRT. I would like to thank all the team of the ID17 beamline of the ESRF for making me feel welcomed and involved in such an important and fascinating research project since the first day. A special thanks goes to Dr. Liam Day for the help with Monte Carlo simulations. I would like to thank the ESRF, as a whole, that together with the Politecnico di Milano gave me the opportunity to work in the field for which I have studied and with people whose career is an example, as well as a stimulus, for me.

My sincere gratitude goes to the Politecnico di Milano, a university that, even if often challenging me, taught me the art of sacrifice and of dedication and the ethical and moral values typical of all sciences.

My deepest gratitude goes to my parents, who have made all this possible and who have helped and supported me in every decision of my life.